STUDY OF CIRCULATION, HYDROGRAPHY AND DISSOLVED OXYGEN CONCENTRATION OVER COASTAL WATERS OF THE SCOTIAN SHELF

by

Qiantong Pei

Submitted in partial fulfilment of the requirements
for the degree of Master

at

Dalhousie University
Halifax, Nova Scotia
May 2022

TABLE OF CONTENTS

LIST OF TABLES

LIST OF FIGURES

ABSTRACT

The main objective of this thesis is to examine the temporal and spatial variability of circulation, hydrography, and dissolved oxygen concentration (DO) over coastal waters of the Scotian Shelf. A simple oxygen model is coupled to level 3 sub-model of a nested-grid circulation-ice modelling system for the southeastern Canadian shelf (seCS). Performances of both the nested-grid modelling system and oxygen model are assessed by comparing model results with available observations and reanalysis data. Model results produced by the nested-grid modelling system during the summer in 2018 are used to examine the effects of atmospheric and tidal forcing on general circulation, temperature, and salinity over the seCS. A process study is conducted using the coupled circulation-oxygen model for investigating main physical processes affecting the temporal and spatial variability of DO over coastal waters off southwest Nova Scotia during the summer in 2018. Analysis of model results demonstrates that both winds and tides affect coastal circulation and enhance the vertical mixing over the coastal waters. Winds significantly affect the hydrography and DO in the upper water column through wind effects on the air-sea fluxes and vertical mixing. Tides affect the local DO maxima at the subsurface of about 20 m through mainly tide-induced mixing. A sensitivity study is conducted using the coupled model to examine the effects of the net water respiration (NWR) and sediment oxygen consumption (SOC) on the DO produced by the oxygen model over the coastal waters. The NWR consumes a relatively large amount of dissolved oxygen (up to 8 mmol m^{-3} in August 2018) in the subsurface water in summertime, due to the distributions of chlorophyll and biomass. The SOC has relatively large effects (up to 15 mmol m^{-3} in August 2018) on the DO near the sea bottom.

LIST OF ABBREVIATIONS AND SYMBOLS USED

Abbreviations:

3D: Three dimensional

BoF: Bay of Fundy

CCI: Climate Change Initiative

CICE: Los Alamos Sea Ice Model

CMC: Canadian Meteorological Center

CR: Control run, numerical experiments with all external forcing inputs and parameterized net water respiration and sediment oxygen consumption

DO: Dissolved oxygen concentration

ECS: eastern Canadian shelf

ECV: Essential Climate Variable

ESA: European Space Agency

GB: Grand Banks

GDS: GHRSST Data Processing Specification

GeB: Georges Bank

GEBCO: The General Bathymetric Chart of the Oceans

GHRSST: Group for High Resolution Sea Surface Temperature

GLORYS: Global Ocean Physics Reanalysis

GoM: Gulf of Maine

GRB29: GLOBAL_REANALYSIS_BIO_001_029

GSL: Gulf of St. Lawrence

ICOADS: International Comprehensive Ocean-Atmosphere Data Set

L1: Level one

L2: Level three

L3: Level three

L3COM: L3 coupled circulation-oxygen model

LIM: Louvain-la-Neuve sea ice model

LS: Labrador Shelf

NARR: North American Regional Reanalysis

NEMO: Nucleus for European Modelling of the Ocean

NFS: Newfoundland Shelf

NGMS-seCS: Nested-grid modelling system for the southeastern Canadian Shelf

NoL3Wind: Numerical experiment same as control run, except for turning off wind forcing in submodel L3 and L3COM

NoNWR: Numerical experiment same as control run, except for turning off the parameterized NWR in L3COM

NoSOC: Numerical experiment same as control run, except for turning off the parameterized SOC in L3COM

NT: NoTide, Numerical experiment same as control run, except for turning off tidal forcing

NW: NoWind, Numerical experiment same as control run, except for turning off wind forcing in submodels L2 and L3 (and L3COM)

NWR: Net water respiration

OTIS: Oregon State University Tidal Inversion System

PEI: Prince Edward Island

PODAAC: Physical Oceanography Distributed Active Archive Center

ROMS: Regional Ocean Modelling System

ScS: Scotian Shelf

seCS: Southeastern Canadian Shelf

SLE: St. Lawrence Estuary

SLGO: St. Lawrence Global Observatory

SLR: St. Lawrence River

SOC: Sediment oxygen consumption

swScS: Southwestern ScS

SSDO: Sea surface dissolved oxygen concentration

SSS: Sea surface salinity

SST: Sea surface temperature

Symbols

$\Delta\bar{T}_Y^{C1-C2}$: Monthly-mean temperature difference between cases C1 and C2 at the depths of Y meters (0 represents the sea surface)

$\Delta\bar{S}_Y^{C1-C2}$: Monthly-mean salinity difference between cases C1 and C2 at the depths of Y meters (0 represents the sea surface)

$\Delta\bar{O}_Y^{C1-C2}$: Monthly-mean dissolved oxygen concentration difference between cases C1 and C2 at the depths of Y meters (0 represents the sea surface)

$\Delta\vec{\bar{U}}_Y^{C1-C2}$: Monthly-mean circulation difference (two-dimensional vector field) between cases C1 and C2 at the depths of Y meters (0 represents the sea surface)

$\Delta\bar{U}_{PP'}^{CR-NT}$ & $\Delta\bar{V}_{PP'}^{CR-NT}$: Monthly-mean alongshore (northeastward) and onshore circulation differences between cases Control Run and NoTide along transect PP' (shown in Figure 3.1b)

$\Delta\bar{O}_{PP'}^{C1-C2}$: Monthly-mean dissolved oxygen concentration difference between cases C1 and C2 on transect PP'

O_{2sat}: Solubility of dissolved oxygen

β: Coefficient for semi-prognostic method

Chl: Chlorophyll concentration

η: Sea surface elevation

γ^2: Values to assess the model performance

H: Local water depths

K_h and K_v: Horizontal eddy diffusivity and vertical eddy viscosity coefficients

R: Respiration rate

PP: Primary production rate

σ: Vertical coordinates in sigma level

θ: Coefficient for sponge layer nudging

Var( ): Variance

X_A: The adjusted temperature and salinity within the thin sponge layer

X_{GLO}: The reanalysis temperature and salinity from daily GLROYS 12V1 dataset

X_U: The unadjusted temperature and salinity

X_S & X_O: The simulated and observed value of variable X at the same observation time

z: Vertical coordinate in the Cartesian coordinate

z_0: Thickness of bottom boundary layer in the parameterization of bottom friction

ACKNOWLEDGEMENTS

Foremost, I would like to sincerely thank my supervisor, Prof. Jinyu Sheng, for providing me a unique opportunity to work on my master's thesis research, which is challenging but scientifically very interesting. I would like to thank him for many constructive academic advice and suggestions. My master's thesis research could hardly be completed without his supports, encouragements, and instructions. It is my honour to be supervised by Prof. Jinyu Sheng. I would also like to thank my other committee members, Drs. Eric Oliver, Jonathan Grant, and Li Zhai for their important instructions, advice, and comments on my thesis research.

I am particularly grateful to Dr. Kyoko Ohashi and Yi Sui for sharing the numerical models and MatLab codes used in this research work. I am also thankful to the other members of Jinyu Sheng's regional ocean modelling group. I benefited a lot from their advice and suggestions during the weekly group meetings. I would also like to thank my external examiner Dr. Dave Greenberg for taking the time to read my thesis and providing very constructive comments and suggestions

Finally, I would like to thank my family members and friends for their loves and supports.

This master's thesis research was supported in part by Prof. Sheng's Natural Sciences and Engineering Research Council of Canada (NSERC) grant, the Ocean Frontier Institute (OFI), and Marine Environmental Observation Prediction and Response Network (MEOPAR).

CHAPTER 1

INTRODUCTION

1.1 Background

The coastal and shelf waters of the Scotian Shelf (ScS) are influenced by tides, winds, buoyancy forcing including freshwater runoff and indirectly by large-scale ocean circulation such as the Labrador Current and Gulf Stream over the northwestern Atlantic Ocean. Because of the great dynamic and geographic complexity, the hydrography and circulation over the ScS have large temporal and spatial variability. Reliable knowledge and reasonable prediction on temporal and spatial variability of hydrography and circulation over the ScS are of great importance to many social and economic activities including fisheries, aquaculture, oil and gas industry, and marine tourism. This places an emphasis on the development of numerical modelling systems to accurately simulate and predict the hydrodynamics over the ScS.

The ScS is a rugged open shelf off Nova Scotia, Canada, bounded by the Northeast Channel, Laurentian Channel, and deep waters of the Northwestern Atlantic Ocean (Figure 1.1). The ScS is about 700 km long and has a width varying from 160 to 240 km, with an average depth of about 90 m (*Smith et al.*, 1978; *Han et al.*, 1997). The shelf break of the ScS, where the bottom slope connecting the coastal and shelf waters to the deep ocean suddenly increases, lies at water depths of about 200 m. The ScS has an irregular bathymetry characterized by shallow offshore banks, deep basins, and deep channels. The waters over

the ScS are originated from three main sources: runoff from the Gulf of St. Lawrence (GSL), the Labrador Current, and North Atlantic water (*Smith et al.*, 1978).

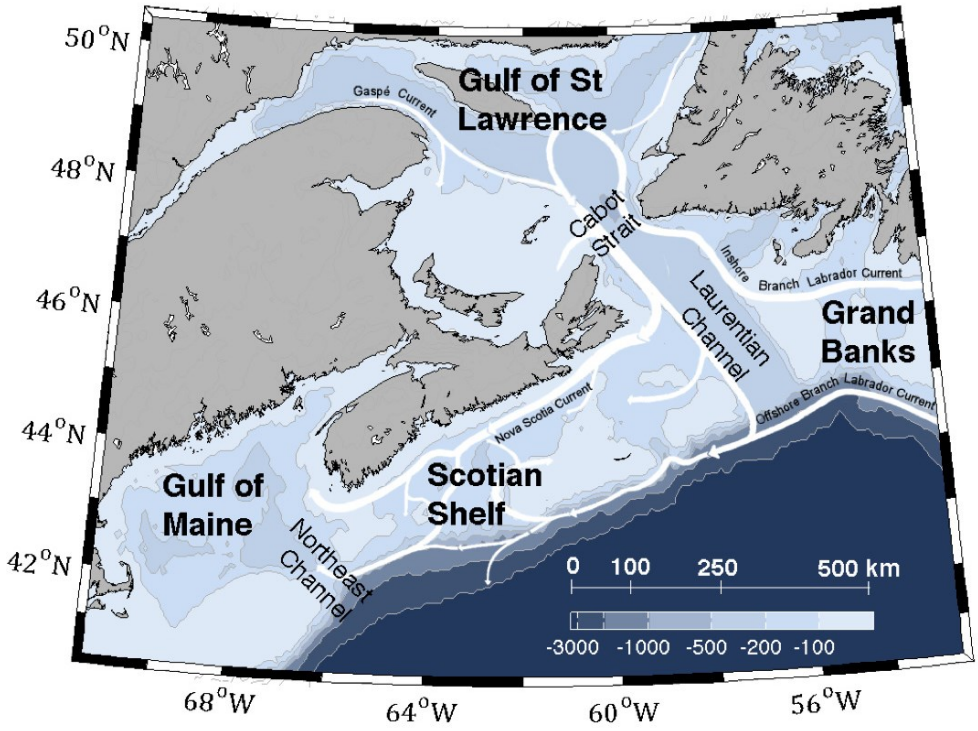

Figure 1.1: Major topographic features and mean circulation over the Scotian Shelf, Nova Scotia, Canada (taken from *Dever*, 2017). The color image indicates the water depth and the white arrows indicate the major circulation patterns.

The general circulation over the ScS is significantly affected by the equatorward flow of relatively cold and fresh shelf water from the GSL, Grand Banks (GB), and Newfoundland Shelf (NFS) (*Loder et al.*, 1997). Major ocean currents over the ScS include the southeastward outflow from the GSL known as the Nova Scotia Current and the offshore branch of the equatorward Labrador Current known as the shelf break jet (Figure 1.1) (*Smith*

and Schwing, 1991; *Dever,* 2017). The Nova Scotia Current carries one branch of the southeastward outflow from the GSL to the ScS and continues flowing southwestward. The southwestward jet at the shelf break of the ScS is a combination of the offshore branch of the Labrador Current and another branch of outflow from the GSL (*Dever*, 2017; *Han et al.*, 1997). These currents interact with the irregular bathymetry, resulting in complicated ocean circulation features over the coastal and shelf waters of the ScS. The bottom topography of submarine banks, basins, and cross-shelf channels is of great importance to the topographic-scale features of hydrography and circulation over the ScS (*Loder et al.*, 1997; *Han et al.*, 1997; *Hannah et al.*, 2001). In particular, the slope water flows and recirculation over the ScS have anticyclonic (cyclonic) circulation tendencies over banks (basins) due mainly to the effect of topographic steering (*Loder et al.*, 1997; *Hannah et al.*, 2001).

1.2 Review of Hydrography and Circulation Variability over the Scotian Shelf, Dissolved Oxygen Concentration, and Parameterizations of Biological Processes in the Ocean

1.2.1 Effects of Winds over the Scotian Shelf

Wind forcing plays a very important role in the ocean circulation and hydrography over the ScS in terms of wind-driven currents and wind-induced mixing. Through wind-induced modifications in hydrography, wind forcing also affects the baroclinic hydrodynamics and density-driven currents. Over some local areas of the ScS, wind forcing interacts with the complicated bottom topography and generates important local hydrodynamical phenomena. Several studies were made in the past to investigate the wind-induced phenomena over coastal waters of the ScS and some local areas. *Smith et al.* (1978) demonstrated that wind stress plays different roles in the alongshore dynamic balance over the inshore and offshore regions of the ScS. *Schwing* (1989, 1992) examined the subtidal

response of the ScS to the time-varying local wind stress. The numerical study by *Greenberg et al.* (1997) indicated that the barotropic response is an important part of the oceanic response to wind stress over the ScS and Gulf of Maine (GoM). Furthermore, the alongshore wind stress was found to be more effective in forcing barotropic response over the ScS and GoM than the cross-shore wind stress (*Greenberg et al.*, 1997). *Yang and Sheng* (2008) showed that local winds strongly affect the three-dimensional (3D) circulation, upwelling and downwelling inside Lunenburg Bay. *Zhai et al.* (2008) suggested that the upwelling and downwelling induced by local wind stress play dominant roles in the spatial and temporal variability of temperature and salinity in Lunenburg Bay. *Shan* (2010) revealed that local winds strongly affect the vertical structure of the low salinity front in Bedford Basin and significantly modulate the tidal circulation in the Narrows of Halifax Harbour. *Zhai et al*. (2008) found a strong baroclinic throughflow with day-to-day variation associated with wind stress. The wind forcing also has significant seasonal variability. One of the important scientific questions to be addressed in this thesis is how the seasonal variability of local wind stress could affect the hydrography and ocean currents over shallow waters of the ScS.

Coastal and shelf waters of the ScS are occasionally affected by tropical cyclones (including hurricanes) and winter storms. During tropical cyclones and winter storms, strong winds can generate intensive ocean currents and large variations in sea surface elevations and hydrography. Strong currents and large variations in hydrography and sea surface elevations (i.e., storm surge) caused by tropical cyclones and winter storms have the potential to incur significant economic damage. *Smith et al.* (1978) investigated the oceanic response of the ScS to strong winter storms based on in-situ observations and found that the transient winds of winter storms generate two types of hydrodynamic variability: strong inertial currents and forced oscillations at atmospheric time scales. Several previous studies demonstrated that tropical cyclones generate sea surface cooling and strong near-inertial currents over areas

along the storm tracks (*Price*, 1981, 1983; *Black,* 1983; *Gill*, 1984; *Chang*, 1985; *Bender et al*., 1993; *Sheng et al*., 2006; *Wang and Sheng*, 2016). One of the main physical mechanisms responsible for the upper-layer seawater cooling during a hurricane is the storm-induced intensive vertical eddy mixing. *Fisher* (1958) suggested that the SST cooling caused by tropical cyclones could reach several Celsius degrees, and the maximum SST cooling generally occurred in the back right quadrant of the storm. Several numerical studies were conducted on ocean responses during specific extreme weather events over the ScS. *Sheng et al.* (2006) investigated the upper ocean responses to Hurricane Juan in September 2003 over the ScS and the adjacent slope waters, and they found that during Hurricane Juan the SST cooling was biased to the right of the storm track and the vertical mixing played a dominant role in cooling the SST. *Wang and Sheng* (2016) studied the ocean responses to three extreme weather events, including two fast-moving hurricanes (Hurricane Juan in September 2003 and Hurricane Bill in August 2009) and a slow-moving winter storm (White Juan in February 2004). For both above-mentioned fast-moving hurricanes, the SST cooling biased to the right of the storm track. White Juan, which is one of the most severe winter storms affecting Nova Scotia and Prince Edward Island, by comparison, generated the SST warming over the central ScS to the left of the storm track (*Wang and Sheng*, 2016). Previous numerical studies provided valuable information about hydrodynamic responses during tropical cyclones and winter storms over the ScS. One of the important scientific questions remained to be addressed is how winter storms and tropical cyclones could affect 3D circulation, hydrography, and vertical seawater transport over specific coastal waters on the ScS such as coastal waters off Liverpool of Nova Scotia.

1.2.2 Effects of Tides over the Scotian Shelf

Tides in the ocean are caused by variations in gravitational force resulting from the relative motions of the Sun and the Moon with respect to the Earth. Tidal elevations and tidal

currents are typically large over coastal and shelf waters (such as the Bay of Fundy) and relatively weak in the deep ocean. In general, tidal currents and tidal mixing alter the circulation and hydrography distributions over coastal and shelf waters, consequently resulting in modulations of density-driven currents and baroclinic hydrodynamics. *Smith et al.* (1978) found that the semidiurnal M_2 constituent is the dominant tidal component on the ScS. The generation of M_2 baroclinic tides leads to the internal Reynolds stress divergences that are capable of producing significant mean circulation and tidal harmonics near the edge of the ScS (*Smith et al.*, 1978). Tidal rectification, on the other hand, supports the anticyclonic gyre around Browns Bank and induces the westward and offshore near-bottom currents off Cape Sable (*Smith*, 1983). *Wang et al.* (2020) recently examined the tidal impacts over the southeastern Canadian Shelf (seCS), and they found large tidal impacts over the central eastern GoM, upper Bay of Fundy, and northern flank of the Georges Bank (GeB). In comparison, relatively small tidal impacts occur over the Labrador Shelf (LS) and NFS (*Wang et al.*, 2020).

Several previous studies also showed that tidal forcing is of great importance to the near-bottom currents over some shallow areas in the ScS (*Smith*, 1983; *Yang and Sheng*, 2008; *Ohashi et al*., 2009a; *Chegini et al*., 2018). For example, the shoreward near-bottom currents off southwest Nova Scotia and the associated upwelling were induced by tides (*Chegini et al.,* 2018).

Tidal forcing also plays an important role in hydrodynamics over several coastal areas of the ScS, due mainly to the baroclinic dynamics and the interaction between tides and bottom topography. *Shan* (2010) showed that tidal forcing significantly influences the 3D circulation over the Narrows of Halifax Harbour and Bedford Basin. Furthermore, tidal forcing was also found to play an important role in affecting the distribution of hydrography over coastal waters of the ScS and some embedded local areas, through its influences on

seawater transport. For example, *Shan* (2010) demonstrated that tidal currents and tidal mixing are important influencing factors of the distributions of water temperature and salinity over the Narrows of Halifax Harbour and Bedford Basin.

Many practical applications, such as offshore oil and gas exploration and operation and nearshore aquaculture industry, require good knowledge on tidal currents and tidal elevations. Hence one of the significant scientific questions to be addressed is how tidal forcing could affect the hydrography and currents over the ScS.

1.2.3 Effects of Buoyancy Forcing over the Scotian Shelf

Buoyancy forcing is the upward forcing exerted on the water parcel associated with the density gradients (or perturbations) in the ocean. As a result, the ocean current driven by density gradients of seawater is known as the buoyancy-driven current. *Smith* (1983) found some strong seasonal cycles of salinity and density fields at Cape Sable which appear to be controlled partially by buoyancy input from coastal currents. In addition, the longshore mean density and stratification gradients are of great importance to the primary dynamical balance for circulation over the ScS (*Smith*, 1983). *Smith and Schwing* (1991) demonstrated that the ocean currents at the Halifax Line can be approximated by the geostrophic currents derived from the density gradients. *Ohashi et al*. (2009b) and *Katavouta et al.* (2016) demonstrated that the seasonal vertical stratification of seawater affects the tidal currents over the ScS through different physical mechanisms. Over the shelf break of the ScS and adjacent deep ocean waters, the seasonal vertical stratification significantly affects the M_2 tidal currents by impacting the baroclinic pressure gradients (*Ohashi et al*., 2009b). Over the Northumberland Strait, by comparison, the seasonal stratification in the vertical affects the M_2 tidal currents by modifying the vertical mixing and bottom stress (*Ohashi et al.*, 2009b). *Katavouta et al.*

(2016) found that the seasonal stratification of seawater in the vertical has relatively stronger impacts on tidal currents over the GoM and deep ocean waters adjacent to the Northeast Channel than other areas of the ScS. Over these two regions, the maximum M_2 tidal currents were found to be stronger in summer than in winter by over 0.1 m/s (*Katavouta et al*., 2016). There are also considerable freshwater discharges entering the eastern Canadian shelf (ECS) through estuaries. The investigation on how river runoffs could influence the hydrography and ocean currents over coastal waters of the ScS is of great importance.

1.2.4 Interaction between Circulation and Sea Ice

Sea ice plays an important role in affecting hydrography and circulation in the polar and high-latitude oceans. The formation and melting of sea ice modify the surface freshwater flux through brine rejection and freshwater release (*Komuro and Hasumi*, 2003). The horizontal movement of sea ice affects the local sea ice formation and melting and thus modifies the spatial variability of surface heat and freshwater fluxes (*Hasumi and Suginohara*, 1995). The spatial inhomogeneity of the surface heat and freshwater fluxes, in return, modifies the density-driven currents and baroclinic hydrodynamics. The transportation of sea ice is also an important part of the global hydrological cycle, which impacts the global thermohaline circulation and salt transportation (*Komuro and Hasumi*, 2003). As a result, the reliable simulation of sea ice is a very important topic for improving our knowledge on physical environmental conditions over the seCS, particularly over the Labrador and Newfoundland Shelves, the Gulf of St. Lawrence and the eastern ScS.

1.2.5 Dissolved Oxygen Concentration and Biological Processes in the Ocean

Oxygen is required for the respiration of marine plants, algae, phytoplankton (the primary producers) and animals in the ocean. Primary producers, including phytoplankton, kelp, and algal plankton, also consume the aqueous carbon dioxide and produce dissolved

oxygen in the ocean through primary production. Observational estimates indicated that the marine oxygen inventory decreased by about 2% over the past 50 years（*Schmidtko et al*., 2019）. The area of low oxygen water in the open ocean has increased by 4.5×10^6 km^2 since the 1960s, and over 500 low oxygen sites have been identified in estuaries and other coastal waters (*Breitburg et al*., 2018). Both physical (e.g., winds, tides and mixing) and biological (e.g., primary production and respiration) processes affect the DO in the ocean. In general, physical processes, including air-sea oxygen flux, turbulent mixing, and horizontal advection, significantly affect the distribution of dissolved oxygen in the ocean. Biological processes, especially in the case of eutrophication, are of great importance to the DO over coastal waters. Eutrophication is characterized by the excessive growth of marine plants and algae caused by the increased availability of limited growth factors (e.g., sunlight, carbon dioxide, and nutrients) required for photosynthesis (*Schindler*, 2006; *Chislock et al.,* 2013). These excessive marine plants and algae will eventually die and cause massive microbial decomposition, leading to significant dissolved oxygen consumption and hypoxic zones over coastal waters, particularly over coastal environments surrounding large and nutrient-rich rivers (*Chislock et al.,* 2013; *Diaz and Rosenberg*, 2008). Reliable modelling and prediction of DO over coastal and shelf waters are of great importance in many practical applications including aquaculture and fisheries.

There are two general types of numerical models in simulating DO over coastal waters. The first type is the coupled physical-biogeochemical models for simulating major physical and biogeochemical variables, including the DO. The coupled physical-biogeochemical models simulate many major physical and biogeochemical processes in the ocean, including advection, mixing, diffusion, nutrient regeneration dynamics, complex interdependencies of multiple trophic levels, and some complicated interactions among different physical and biogeochemical processes (*Hood et al.*, 2006; *Rose et al.*, 2010; *Ganju*

et al., 2016). By considering multiple physical and biogeochemical processes, the coupled physical-biogeochemical models have very sophisticated model setups and require very detailed data inputs. The current trend of biogeochemical model development is towards increasing complexity through including more state variables and processes (*Rose et al.*, 2010*; Low-Décarie et al*., 2014; *Ganju et al*., 2016). However, there are significant gaps in the current understanding of many biogeochemical variables and processes. Some parameterizations in these coupled physical-biological models require further improvements and optimizations. It should be noted that in-situ oceanographic observations to be used for validating intricate biogeochemical models are also very limited (*Ganju et al*., 2016; *Steiner et al.*, 2016).

The second type of numerical DO models is the simple oxygen model in which the biogeochemical processes are parameterized in terms of the net water respiration (NWR) and sediment oxygen consumption (SOC). In comparison with the above-mentioned coupled physical-biogeochemical models, the simple oxygen model is computationally more efficient and easier to setup with certain skills in simulating temporal and spatial variability of DO over coastal waters. The simple oxygen model is also useful in process-oriented studies. The main drawback of the simple oxygen model is large uncertainties for parameterizing the biogeochemical processes affecting the DO in the simple oxygen model, due mainly to the lack of good understanding of functional dependencies of different biogeochemical variables in the ecosystem. For example, the aquatic respiration rate is regulated by many biogeochemical variables and processes, including the variability of carbohydrate concentration, distribution of biomass, and biological activities in the coupled physical-biogeochemical models.

Several studies were made on the parameterizations of physical and biological processes affecting the DO in the ocean. *Wanninkhof* (1992) demonstrated a parabolic

relationship between the gas transfer velocity and surface wind speed. *Hetland and DiMarco* (2008) proposed a temperature and oxygen-dependent parameterization for the sediment oxygen consumption (SOC) rate. The SOC is a biological sink of dissolved oxygen occurring at the sea bottom. *Packard and Christensen* (2004) showed a strong linear relationship (with r^2 values about 0.9) between the respiration rates and chlorophyll concentration over the ScS, based on in-situ observations. *Del Giorgio et al*. (2005) suggested a linear relationship between the total respiration rate and chlorophyll concentration over the North Atlantic Ocean, based on the statistical analysis of observations (p. 159). *Fennel et al*. (2013) simulated the DO and hypoxia in the northern Gulf of Mexico by parameterizing the net air-sea oxygen exchange flux at the sea surface, based on the Schmidt number and gas transfer velocity suggested by *Wanninkhof* (1992).

Previous observational and numerical studies demonstrated that local winds significantly affect air-sea oxygen fluxes and the vertical mixing in the upper water column of seawater. Tidal forcing significantly enhances the surface and subsurface vertical mixing over some coastal waters. One of the important scientific questions to be addressed in this thesis is how tides and local wind stress affect the DO and associated temporal and spatial variability over coastal waters off southwest Nova Scotia based on model results produced by the simple oxygen model coupled to a 3D circulation model for the southwestern ScS.

1.3 Objectives

Previous studies improve our knowledge on the variability of ocean currents and hydrography over some coastal waters of the ECS and parameterizations of physical and biological processes affecting DO in the ocean. Many important scientific questions, however, remain to be addressed. It is important to understand how the tidal forcing, atmospheric forcing and large-scale ocean circulation affect the 3D hydrography, ocean currents, and DO

over coastal waters of the ScS. It is also important to understand how winter storms and tropical cyclones affect the 3D circulation, hydrography, and vertical seawater transport over coastal waters of the ScS. These scientific questions motivate me to conduct numerical studies on the variability of hydrography and ocean circulation over coastal waters of the ScS by using a coupled circulation-ice modelling system.

The overall objective of my master's thesis research is to examine the temporal and spatial variability of circulation, hydrography, and DO over coastal waters of the ScS. The specific research areas of my thesis research include:

1. Validate a coupled circulation-ice modelling system for simulating the water temperature, salinity, and ocean currents over coastal waters of the ScS.
2. Conduct a process study to examine the influences of tides and winds on water temperature, salinity, and ocean currents over coastal waters of the ScS, with a special focus on coastal waters off Liverpool, NS.
3. Validate a numerical oxygen model for simulating the dissolved oxygen concentration and examine the effects of local winds, tides, net water respirations, and sediment oxygen consumptions on the concentration of dissolved oxygen over coastal waters off southwest Nova Scotia.

In this study, model results of 3D hydrography and circulation in 2018 produced by the numerical modelling system are used to examine the variability of hydrography and circulation over the ScS. Model results of DO during the summer of 2018 are used to examine the variability of DO over coastal waters off southwest Nova Scotia.

1.4 Outline of the Thesis

The structure of this MSc thesis is as follows. Chapter 2 provides a description of the nested-grid coupled circulation-ice modelling system, model external forcing, and performance assessment of the coupled modelling system. The coupled modelling system uses the three-level nesting setup, with the outermost submodel (L1, refer to Level 1) for the southeastern Canadian shelf (seCS) and the innermost submodel (L3) for the coastal waters off southwest Nova Scotia. Chapter 3 presents a numerical study of hydrodynamic responses of the seCS to an extreme wind event, with a special emphasis on 3D circulation and hydrography over coastal waters off southwest Nova Scotia. Chapter 4 presents a simple oxygen model coupled to submodel L3 of the coupled circulation-ice modelling system and validations of the simulated DO. A sensitivity study and a process study are also presented in Chapter 4 using the coupled circulation-oxygen model to examine the effects of net water respirations and sediment oxygen consumptions and the effects of local winds and tides on DO over coastal waters of the ScS. The final chapter provides summaries and conclusions of this thesis research.

CHAPTER 2

PHYSICAL MODEL SETUP AND VALIDATION

One of important research tools used in my thesis is a coupled circulation-ice modelling system developed recently by the Regional Ocean Modelling Group of Dalhousie University led by Professor Jinyu Sheng. The coupled modelling system uses the 3-level nesting setup with the one-way nesting technique. Model performance is assessed using various types of observations, including the remote sensing data, in-situ observations, and reanalysis data.

2.1 Physical Model Setup

The coupled circulation-ice modelling system (hereinafter NGMS-seCS) used in my thesis research is based on the Regional Ocean Modelling System (ROMS) and the Los Alamos Sea Ice Model (CICE, https://zenodo.org/record/1205674; *Hunke et al*., 2017) for the southeastern Canadian shelf (seCS). The external coupler developed by *Hedström* (2009) (github.com/kshedstrom/roms) is used for two-way coupling between the ROMS and CICE. The model bathymetry of the coupled system is based on the GEBCO_2014 dataset (available on https://www.gebco.net/data_and_products/gebco_web_services/).

ROMS is a free-surface and terrain-following numerical ocean model. It numerically solves the Reynolds-averaged Navier-Stroke equations with hydrostatic and Boussinesq assumptions (www.myroms.org). The model has been developed and supported by researchers at the Rutgers University, University of California Los Angeles and contributors worldwide (www.myroms.org). ROMS has been widely used in simulating 3D currents and

hydrography over many different coastal and shelf waters of the world's oceans (*Hetland and DiMarco*, 2008; *Zhang et al.*, 2010; *Fennel et al.*, 2013; *Lin et al.*, 2021).

CICE is a numerical model for simulating the growth, melt and movement of sea ice. It solves numerically two main physics equations for the sea ice: (a) Newton's second law for sea ice and the (b) evolution of the sea ice thickness distribution for different thicknesses spread of the area (*Hunke et al*., 2010). The first version of CICE was developed by Elizabeth Hunke at Los Alamos National Laboratory. Since its initial release in 1998, the CICE has been substantially developed by an international community of model users and developers.

The NGMS-seCS has three submodels, with nested domains of successively smaller areas and higher horizontal resolutions. The domain of submodel L1 covers the southeastern Canadian shelf (seCS) and adjacent deep ocean waters between 80° W and 40° W, and between 34° N and 55° N (Figure 2.1a), with a horizontal resolution of 1/12°. The domain of submodel L2 covers the Gulf of St. Lawrence-Scotian Shelf-Gulf of Maine (GSL-ScS-GoM) and adjacent deep ocean waters between 71.5° W and 56° W, and between 38.5° N and 52° N (Figure 2.1b), with a horizontal resolution of 1/36°. The domain of submodel L3 covers the coastal waters of the southwestern ScS between 66° W and 63° W, and between 43° N and 44.75° N (Figure 2.1c), with a horizontal resolution of 1/108°. The main advantage of the nested-grid modelling system is that the lower-level (child) submodel can resolve relatively fine-scale hydrodynamical features by using the dynamically consistent open boundary conditions provided by the upper-level (parent) submodel.

A one-way nesting technique is used in the coupled modelling system, in which information from the upper-level submodel is transferred to the lower-level submodel. Specifically, results of sea surface elevations, currents, temperature, salinity and sea ice

conditions produced by submodel L1 are used to specify open boundary conditions for submodel L2. Similarly, results of submodel L2 are used to specify open boundary conditions for submodel L3. In each submodel, the Smagorinsky scheme (*Smagorinsky,* 1963) and the level 2.5 Mellor-Yamada turbulence closure (*Mellor and Yamada*, 1982) are used respectively for the horizontal and vertical eddy mixing coefficients.

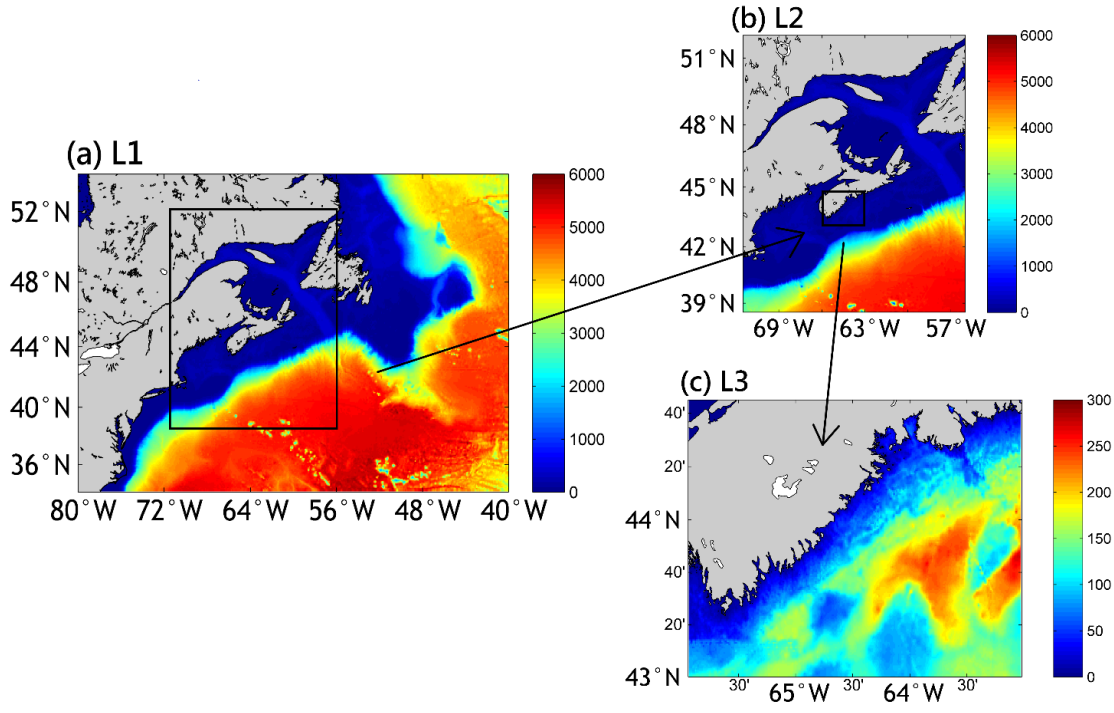

Figure 2.1. Major topographic features and domains of three submodels for a nested-grid coupled circulation-ice modelling system (NGMS-seCS) for the southeastern Canadian shelf and adjacent deep ocean waters of the northwestern Atlantic Ocean. The horizontal resolutions of submodels (a) L1, (b) L2, and (c) L3 are respectively 1/12°, 1/36° and 1/108°. The color image in each subplot represents water depths.

Each submodel of the NGMS-seCS has 40 σ-levels in the vertical with various σ intervals. The σ vertical coordinate used in the model is defined as

$$\sigma = \frac{z-\eta}{H+\eta} \tag{2.1}$$

where z is the Cartesian vertical coordinate, with $z = 0$ for the equilibrium position of the sea surface. Here $\eta(x, y, t)$ is the displacement of the sea surface from its equilibrium position ($z = 0$), and $H(x, y)$ is the local water depth.

2.2 Initial Conditions and External Forcing

The model initial conditions of water temperature, salinity, sea surface elevations, and 3D currents are specified based on the daily Global Ocean Physics Reanalysis dataset (https://resources.marine.copernicus.eu) with a horizontal resolution of 1/12º (GLORYS 12V1 dataset). The GLORYS 12V1 dataset was constructed by the Copernicus - Marine Environment Monitoring Service (CMEMS).

The NGMS-seCS is driven by tides, atmospheric forcing, and freshwater discharge. The tidal forcing is specified at the open boundaries of the outer-most submodel (L1) in terms of tidal elevations and depth-mean currents of 11 major tidal constituents (M_2, S_2, N_2, K_2, K_1, O_1, P_1, Q_1, M_4, MS_4, and MN_4). The harmonic constants of these 11 major tidal constituents were extracted from the results produced by the Oregon State University Tidal Inversion System (OTIS, *Egbert and Erofeeva*, 2002), with a horizontal resolution of 1/6º.

The atmospheric forcing used to drive the coupled modelling system includes the three-hourly fields of air pressure, specific humidity, and air temperature at the sea surface, and wind velocity at 10 m above the mean sea level. These fields were extracted from the three-hourly North American Regional Reanalysis (*Mesinger et al*., 2006) with a horizontal

resolution of 32 km. The bulk formula from *Large and Pond* (1981) is used to calculate the wind stress from the wind velocity at 10 m about the mean sea level. The atmospheric forcing also includes three-hourly shortwave and longwave radiation fluxes, cloud fraction, and precipitation. In each submodel, linear interpolation is used to interpolate the three-hourly atmospheric forcing into the model time steps, and Barnes' method is used to map the atmospheric forcing into the model grid.

The freshwater discharges from 49 major rivers over the seCS are specified in the NGMS-seCS using the monthly-mean climatological data (*Lin*, 2021; *Lin et al.*, 2021), except for the St. Lawrence River (SLR), for which the freshwater discharge is specified in the model based on the monthly-mean values published by the St. Lawrence Global Observatory (SLGO). These monthly-mean values were estimated by applying a regression model (*Bourgault and Koutitonsky*, 1999) on observed sea surface elevations. These freshwater inputs are implemented in the modelling system using idealized channels cut into the coastline (*Lin et al.*, 2021).

In submodel L1, the lateral open boundary conditions of water temperature, salinity, ocean current, sea ice concentration, sea ice thickness, and sea ice momentum are specified based on the daily GLORYS 12V1 dataset. The adaptive open boundary condition (*Marchesiello et al.,* 2001) is used in submodel L1, with the time scales of 1.0 day for the inward flux condition and 360 days for the outward flux condition. In addition, a thin sponge layer (with the thickness of 20 grid points in the normal direction of the boundary) is used at the open boundaries of submodel L1 by restoring the model temperature and salinity to the GLORYS 12V1 dataset based on

$$X_A = X_U + \theta \cdot (X_{GLO} - X_U) \tag{2.2}$$

where X_A represents the adjusted temperature and salinity within the thin sponge layer, X_U represents the unadjusted temperature and salinity, and X_{GLO} represents the reanalysis temperature and salinity from daily GLROYS 12V1 dataset. In this study, θ is set to 0.5 for the first 15 grid points and decrease from 0.5 to 0 for the remaining 5 grid points.

In submodels L1 and L2, the semi-prognostic method developed by *Sheng et al.* (2001) and the spectral nudging method developed by *Thompson et al.* (2007) are used to reduce the model systematic seasonal drift. The basic idea of the semi-prognostic method is to introduce a correction term (i.e., an interactive forcing) to the horizontal momentum equations based on differences between the model density and climatological density through the model hydrostatic equation (*Sheng et al*., 2001). The correction term affects directly the model-computed circulation and hence affects indirectly the simulated hydrographic features. In this study, the value of β (coefficient for semi-prognostic method) is set to 0.15, and the semi-prognostic method is applied from the sea surface to sea bottom. More details of the semi-prognostic method are available in Appendix B.

Different from the semi-prognostic method, the spectral nudging method nudges the model-computed temperature and salinity toward the climatological values in the prescribed frequency-wavenumber bands (*Thompson et al*., 2007). It should be noted that the spectral nudging method is only applied at the subsurface below 30 m (controlled by the nudging coefficients), since the hydrography in the top 30 m is dominantly influenced by the atmospheric forcing and freshwater discharges from rivers. The spectral nudging coefficients increase from 0 to 0.0011 linearly with depths from 30 to 40 m and equal to 0.0011 at depths greater than 40 m. More details of the spectral nudging method are available in Appendix C.

2.3 Model Results and Validation

The NGMS-seCS is integrated for one year from the beginning of January 2018 to the end of December 2018. The performance of submodel L1 in simulating the sea surface elevations, sea surface temperature (SST), sea surface salinity (SSS), and sea ice concentration is assessed by comparing model results with in-situ oceanographic observations provided by the Marine Environmental Data Service of Fisheries and Oceans Canada (MEDS-DFO) and satellite remote sensing data extracted from the GHRSST Level 4 CMC0.1deg Global Foundation Sea Surface Temperature Analysis and Sea Surface Salinity Essential Climate Variable datasets.

2.3.1 Sea Surface Elevation

The tide gauge data at Halifax and Yarmouth are used to assess the model performance in simulating sea surface elevations. The in-situ observations of sea surface elevations were obtained from the MEDS-DFO.

For quantitative assessments of the model performance, the γ^2 value is calculated based on the definition given by *Thompson and Sheng* (1997):

$$\gamma^2 = \frac{Var(X_o - X_s)}{Var(X_o)} \tag{2.3}$$

where X_S and X_O represent respectively the simulated and observed value of variable X at the same observation time. The γ^2 values are in the range of 0 and infinity. Smaller values of γ^2 imply better performances of the numerical model in simulating variable X. The critical value of γ^2 is set to 1 in this study.

Figure 2.2a presents time series of observed and simulated total sea surface elevations at the Halifax tidal gauge station for the period from February 5 to March 27, 2018. The simulated surface elevations (blue) shown in the figure are produced by submodel L1. The value of γ^2 is about 0.09 for this period and similar values are found for other periods in 2018, indicating the satisfactory performance of submodel L1 in simulating the total sea surface elevations at Halifax.

The total sea surface elevations are affected by tidal and non-tidal forcing. To examine the model performance in simulating tidal and non-tidal components of sea surface elevations, the observed and simulated total sea surface elevations are decomposed into tidal and non-tidal components using t_tide Matlab program (*Pawlowicz et al*., 2002). It should be noted that the non-tidal surface elevations obtained by using t_tide still contain some tidal components. As a result, any remaining high-frequency variability with periods of less than 3 hours in the non-tidal surface elevations is eliminated using a low-passed filter.

The maximum observed tidal and non-tidal sea surface elevations at Halifax are about 1.0 m and 0.5 m respectively during the period from 5 February to 27 March 2018 (Figures 2.2b and 2.2c). As shown in Figure 2.2b, submodel L1 performs very well in simulating tidal sea surface elevations in Halifax, with the γ^2 value of about 0.04 during this period. During other periods in 2018, Submodel L1 performs also very well in simulating the tidal elevations at Halifax, with the small values of γ^2 in the same order of magnitude as in Figure 2.2b.

Figure 2.2c shows the simulated and observed non-tidal sea surface elevations at Halifax during the period from 5 February to 27 March 2018. The γ^2 value is about 0.304 for submodel L1 in simulating the non-tidal surface elevations at Halifax during this period, which is small but larger than the γ^2 value for the tidal elevations. One plausible reason is that the actual atmospheric conditions (i.e., winds and atmospheric pressures) over coastal

waters near Halifax, particularly during storm events, are not well represented by the North American Regional Reanalysis products. Another plausible reason is that the horizontal resolution of submodel L1 is not fine enough to resolve fine-scale topographic and circulation features over the inner shelf waters of the ScS. These fine-scale features of local circulation and topography play roles in affecting the sub-tidal wind-driven sea level variations over coastal shallow waters. In addition, the parameterizations of sub-grid mixing, i.e., the Smagorinsky scheme and level 2.5 Mellor-Yamada turbulence closure, and bottom friction, i.e., the logarithmic parameterization from *Warner et al*. (2008), with z_0 = 0.02 m, in the model also play some roles in affecting the accuracy of simulated sub-tidal sea surface elevations over the ScS.

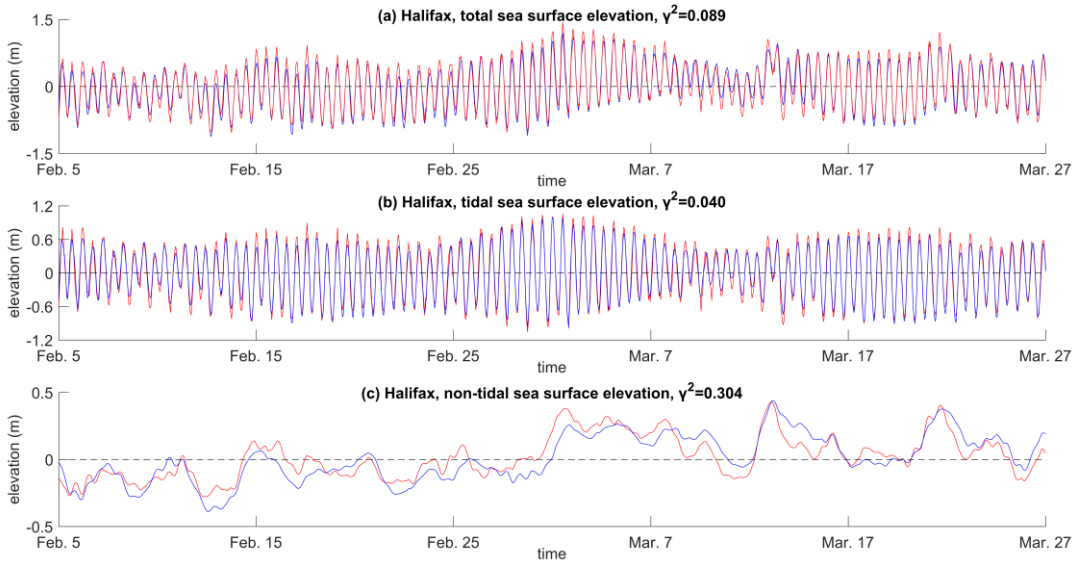

Figure 2.2. Time series of observed (red) and simulated (blue) (a) total, (b) tidal and (c) non-tidal sea surface elevations at the Halifax tidal gauge station for the period from 5 February to 27 March 2018. The simulated results are produced by submodel L1.

Figure 2.3 presents the observed (red) and simulated (blue) total, tidal and non-tidal sea surface elevations at the Yarmouth tidal gauge station from 5 February to 27 March 2018.

The maximum observed tidal and non-tidal surface elevations are about 2.2 m and 0.4 m respectively at Yarmouth during this period. The γ^2 values for simulating the total, tidal, and non-tidal sea surface elevations at Yarmouth during this period are about 0.02, 0.01 and 0.32 respectively. Similar γ^2 values were found for the satisfactory model performance during other periods of 2018 at Yarmouth.

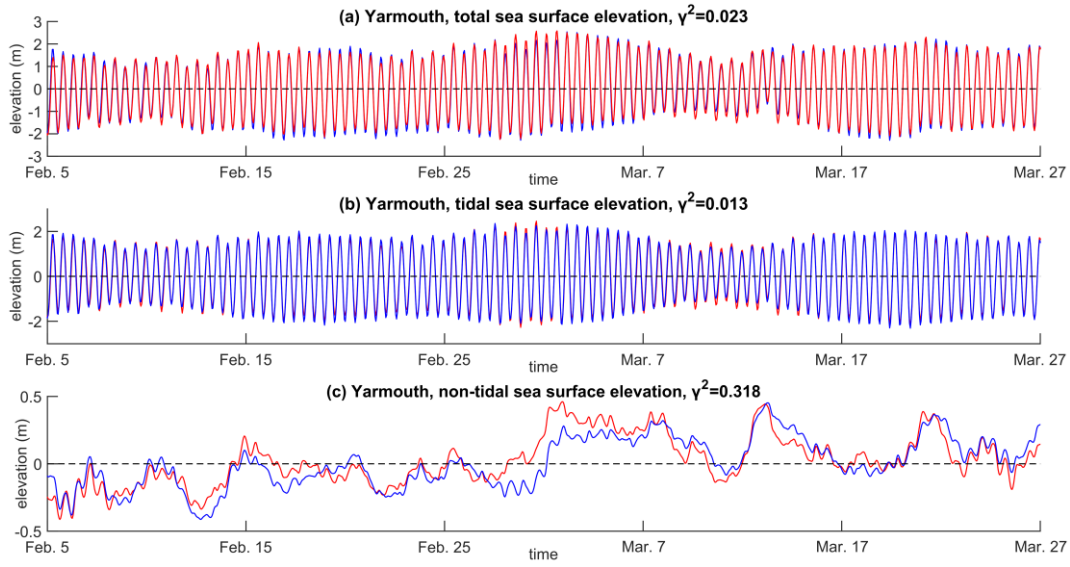

Figure 2.3. Time series of observed (red) and simulated (blue) (a) total, (b) tidal and (c) non-tidal surface elevations at Yarmouth tidal gauge station from 5 February to 27 March 2018. The simulated results are produced by submodel L1.

As discussed above and also shown in Figures 2.2 and 2.3, submodel L1 performs reasonably well in simulating tidal elevations at Halifax and Yarmouth, with small γ^2 values of about 0.04 and 0.01 respectively. These very small γ^2 values for simulated tidal elevations indicate that submodel L1 has satisfactory skills in reproducing tidal elevations over coastal waters of the ScS. Submodel L1 also performs reasonably well in simulating non-tidal surface elevations at Halifax and Yarmouth, with γ^2 values of about 0.30 and 0.32 respectively.

Although larger than the values for tidal elevations, the γ^2 values for the non-tidal elevations are still small and comparable to the counterparts published in the literature (*Shan*, 2010; *Shan and Sheng*, 2012), indicating that submodel L1 has satisfactory skills in reproducing non-tidal elevations over coastal waters of the ScS.

To further assess the model performance in simulating tidal elevations over the seCS, tidal harmonic analyses using the t_tide Matlab program were conducted for the sea surface elevations produced by submodel L1 over the whole domain of submodel L1 during the period from 1 to 30 June 2018.

Figure 2.4a,c presents respectively the co-phases (black contour lines) and co-amplitudes (red contour lines) of the M_2 and K_1 tidal elevations computed from L1 model results. Figure 2.4b,d presents respectively the co-phases and co-amplitudes of the M_2 and K_1 tidal elevations based on the OTIS tidal model results (input tidal forcing for submodel L1). The OTIS provides one of the best products for the barotropic tides in the global oceans (https://www.tpxo.net), since OTIS is the data-assimilative tidal model results using various satellite altimetric data (including data collected by TOPEX Poseidon, TOPEX Tandem, European Remote Sensing, and Geosat Follow-On Satellites) and in-situ observations made by tide gauges and ship born acoustic Doppler current profilers (https://www.tpxo.net). An examination of Figure 2.4a,b demonstrates that submodel L1 reproduces reasonably well the distributions of co-amplitudes and co-phases of M_2 tidal elevations over the seCS and adjacent deep ocean waters. In particular, submodel L1 reproduces reasonably well positions of two M_2 amphidromic points over the domain of submodel L1. One M_2 amphidromic point is close to the eastern boundary of L1 domain, and another is over the central area of the GSL. Around both the M_2 amphidromic points, the M_2 tidal elevations rotate cyclonically. As shown in Figure 2.4a,b, the amplitudes of M_2 tidal elevations are large in the St. Lawrence Estuary (SLE), GoM, Bay of Fundy (BoF), ScS, and southern Newfoundland Shelf (NFS).

In the St. Lawrence Estuary, the maximum amplitudes of the M_2 tidal elevations are over 1.5 m. In the GoM, the amplitudes of the M_2 tidal elevations are generally over 0.7 m and decrease to less than 0.5 m over the Georges Bank and adjacent deep waters. In the BoF, the amplitudes of M_2 tidal elevations are generally over 4 m. Over the ScS and southern NFS, the amplitudes of the M_2 tidal elevations are generally between 0.4 and 0.6 m. Furthermore, the positions of M_2 amphidromic points, rotations of M_2 tidal elevations, and distribution of M_2 co-amplitudes produced by submodel L1 are consistent with previous model results made by *Han et al*. (2010) and *Wang et al.* (2020).

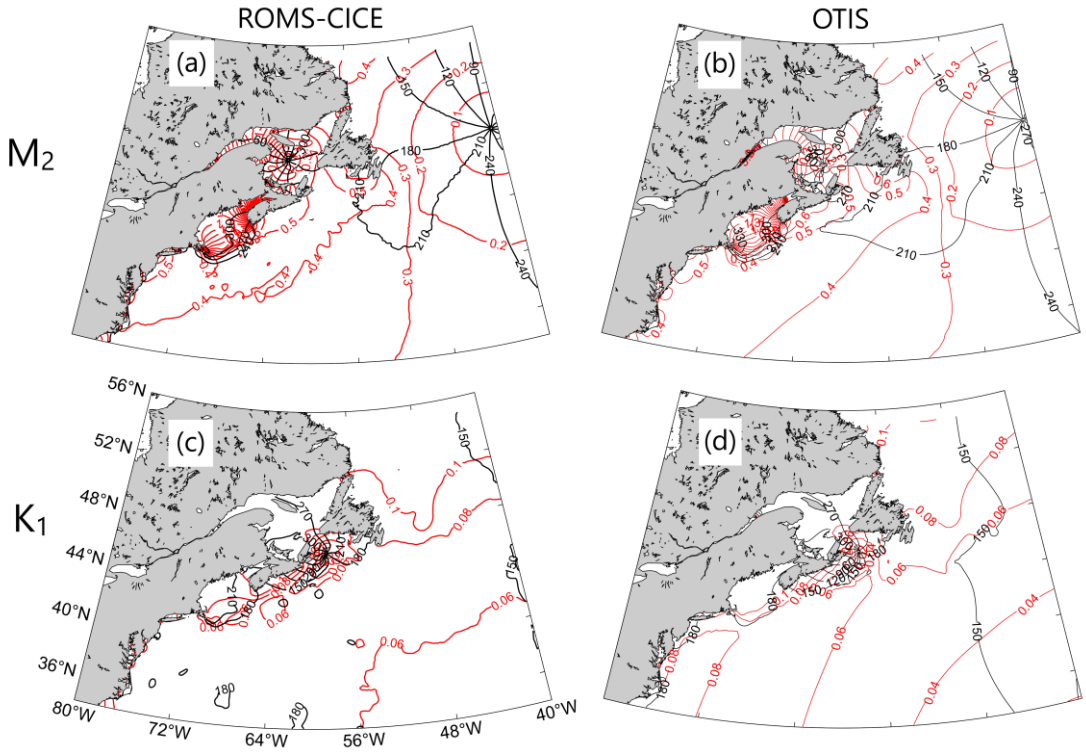

Figure 2.4. Co-phases (black contour lines) and co-amplitudes (red contour lines) of the M_2 (upper panels) and K_1 (lower panels) tidal elevations calculated from results produced by submodel L1 using t_tide (left panels) and taken from OTIS dataset (right panels). The ground truth data are from m_map Matlab program (*Pawlowicz*, 2020).

An examination of Figure 2.4c,d demonstrates that submodel L1 has reasonable skills in reproducing distributions of co-phases and co-amplitudes of K_1 tidal elevations over the GSL, ScS, and GoM. Submodel L1 reasonably reproduces the position of the K_1 amphidromic point over the southern Laurentian Channel. Around the K_1 amphidromic point, the K_1 tidal elevations rotate cyclonically in Figure 2.4c,d. The position of K_1 amphidromic point and cyclonic rotations of K_1 tidal elevations simulated by submodel K_1 are generally consistent with the OTIS model results and previous studies (e.g., *Han et al.*, 2010; *Wang et al*., 2020). Some differences occur in co-phases and co-amplitudes of the K1 tidal elevations shown in Figure 2.4c,d over the deep ocean in the domain of submodel L1. Over the deep ocean within the domain of submodel L1, large differences in amplitudes of K_1 tidal elevations between model results of submodel L1 and the OTIS are about 0.02 m. One possible explanation for these differences is the baroclinic hydrodynamics and other physical processes over the deep ocean. It should be noted that submodel L1 generates small-scale features in co-amplitudes and co-phases in the deep ocean waters to the south of the ScS and GoM, due mainly to baroclinic dynamics (*Wang et al*., 2020).

2.3.2 Sea Surface Temperature, Salinity, and Sea Ice

In this section, we assess the performance of submodel L1 of NGMS-seCS in simulating monthly mean SST, SSS, sea ice conditions and general circulation using satellite remote sensing data and global ocean reanalysis. The satellite remote sensing data of SST and sea ice concentration used here were extracted from the daily GHRSST Level 4 CMC0.1deg Global Foundation Sea Surface Temperature Analysis (GDS version 2) dataset, provided by the Physical Oceanography Distributed Active Archive Center (PODAAC). This dataset was constructed by merging the infrared satellite SST from the Advanced Very High Resolution Radiometers (from NOAA-18, NOAA-19, METOP-A and METOP-B) and microwave SST data from the Advanced Microwave Scanning Radiometer 2 onboard the

GCOM-W satellite in conjunction with in situ observations of SST from drifting buoys and ships from the International Comprehensive Ocean-Atmosphere Data Set (ICOADS) program (podaac.jpl.nasa.gov/dataset/). This dataset also includes the remote sensing sea ice concentration constructed in the same way as SST.

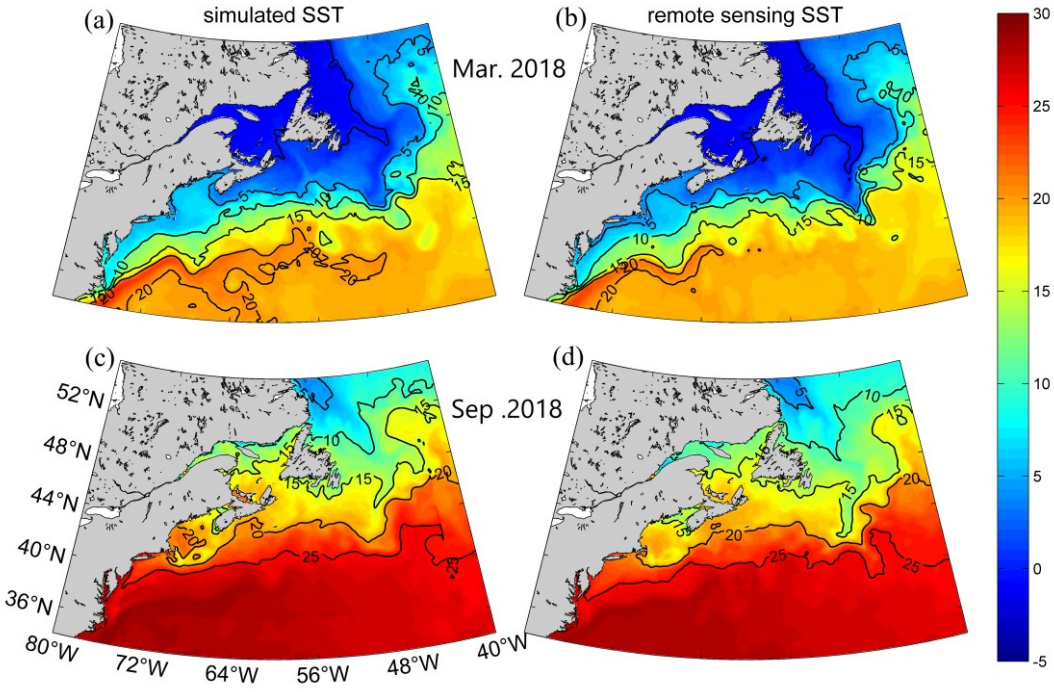

Figure 2.5. Monthly-mean SST over the domain of submodel L1 in (a,b) March and (c,d) September 2018 calculated respectively from (a,c) results produced by submodel L1 and (b,d) satellite remote sensing SST data.

Figure 2.5a shows the monthly-mean SST in March 2018 produced by submodel L1. The simulated March-mean SST is cold and ranges from -2 °C to 5 °C over the ScS, GSL, BoF, LS, NFS, and GB. In the GoM, slope water region of the seCS, and deep ocean waters off the LS, NF, and GB, the simulated March-mean SST ranges from 5 °C to 15 °C. Over the

deep ocean waters to the south of the seCS, by comparison, the simulated March-mean SST is relatively warm and ranges from 15 °C to 22 °C. Submodel L1 also generates small-scale SST features associated with eddies and meandering of the Gulf Stream in the deep waters to the south of the ScS and GOM. Previous studies demonstrated that, after separating from Cape Hatteras (35.5 °N, 75.5 °W), the Gulf Stream turns eastward and changes from fast straight flows to slow meandering currents (*Webb*, 2019, p. 201; *Zhang and McGillicuddy*, 2020). The meandering currents result in warm-core (cold-core) rings pinched off from the northern (southern) side of the Gulf Stream. These warm-core rings (anticyclonic with about 1 km deep and 100 km across) entrap warm (and salty) waters and transport them north to the seCS (*Webb*, 2019, p. 201; *Zhang and McGillicuddy*, 2020). These warm-core rings were formed associated with the Gulf Stream instability processes related to the conversion between the potential energy and eddy kinetic energy (*Gill et al.*, 1974; *Robinson et al.*, 1989; *Stammer and Wunsch*, 1999; Gangopadhyay et al., 2019). With the same physical mechanism, the baroclinic instability also results in some meso-scale and small-scale warm/cold-core eddies over coastal and slope waters of the ScS. The statistical studies of *Brown et al.* (1986) and *Auer* (1987) indicated that the production of the warm-core ring by the Gulf Stream system peaks in the summer months.

The simulated September-mean SST (Figure 2.5c) ranges from 5 °C to 10 °C over the LS and adjacent deep ocean waters, due mainly to the effect of the Labrador Current, which transports relatively cold and fresh waters from high latitudes equatorward. Over the northern GSL, inner shelf waters off southern Newfoundland, and coastal waters of the eastern NFS, the simulated September-mean SST is relatively warm and ranges between 10 °C and 15 °C. Over the southern GSL, ScS, and southwestern NFS, the simulated September-mean SST is generally between 15 °C and 21 °C. Over the deep ocean waters off the seCS, the simulated monthly-mean SST is warm and ranges between 25 °C and 28 °C. Submodel L1 also

simulates small-scale SST features associated with thermal fronts over the southern GSL, ScS, GoM, and GeB.

The performance of submodel L1 in simulating SST is assessed by comparing simulated SST fields (Figure 2.5a,c) with the SST inferred from the daily GHRSST Level 4 dataset (Figure 2.5b,d). An examination of Figure 2.5a,b demonstrates that submodel L1 reproduces reasonably well the general features of observed monthly-mean SST over the domain of submodel L1 in March 2018. Submodel L1 reasonably reproduces the observed cold SST over the GSL, GB, and coastal and shelf waters of the ScS, NFS and LS, and the observed warm SST in the deep ocean waters off the southern ECS in March 2018. Submodel L1 also has reasonable skills in reproducing the general features of the thermal fronts over the slope water regions of the seCS, NFS and LS. It should be noted that submodel L1 is not able to generate the observed small-scale features such as meso-scale eddies and meanders associated with the Gulf Stream and Labrador Current. Due to their nonlinear characteristics, accurate simulations of meso-scale eddies and meanders require the assimilation of various instantaneous in-situ observations and satellite remote sensing data into the model. Noticeable differences also occur between the simulated and observed March-mean SST over some local areas, including the GoM and southwestern ScS. Over these areas, the simulated SST is slightly warmer than the observation. One possible reason is that the wind-induced vertical mixing and upwelling/downwelling over these areas may not be well reproduced by submodel L1 due to the relatively coarse horizontal resolution of wind forcing. Another possible reason is that the freshwater discharges and the water temperature of freshwater runoffs over these areas are specified from the monthly mean climatology rather than the actual values in the model. It should be noted that some satellite remote sensing data of SST have relatively low spatial accuracy over coastal waters.

An examination of Figure 2.5c,d demonstrates that submodel L1 also has similar satisfactory skills to reproduce the main features of the observed September-mean SST in 2018 over the model domain. Submodel L1 reproduces the observed relatively cold SST over the LS and adjacent deep ocean waters, the observed relatively warm SST over coastal and shelf waters of the ScS and southern NFS, and the observed very warm SST over the deep ocean waters off the seCS. In addition, submodel L1 also reproduces the general distribution of the observed September-mean SST over the GSL, including the relatively low monthly-mean SST off the northwestern Anticosti Island. Submodel L1 also has sat skills in reproducing the September-mean observed SST features associated with thermal fronts and the meandering of the slope water jet over the slope water regions of the seCS and Newfoundland-Labrador Shelves. The length scales and general locations of the monthly-mean simulated and observed thermal fronts generally agree.

Noticeable differences occur, however, between the monthly-mean simulated and observed SST in September 2018 over several local areas. Submodel L1 does not simulate well the cold water tongue over the GB. The simulated Gulf Stream still slightly overshoots northward in this month. The overshot Gulf Stream in the model pushes back the cold water tongue over the GB. In addition, submodel L1 slightly overestimates the September-mean SST in 2018 over the western GoM and BoF. One possible explanation is that the overshot Gulf Stream in the model transports more warm surface waters to the GoM from the south. Another possible explanation is the model error in simulating wind-induced mixing due to the relatively coarse horizontal resolution of atmospheric forcing.

It should be noted that the use of the semi-prognostic and spectral nudging methods, with a thin sponge layer at the open boundary conditions reduces significantly the model systematic errors in simulating the large-scale circulation in the study region, including the Gulf Stream and Labrador Current. Discussions about the effect of the semi-prognostic

method and the spectral method in reducing the systematic model errors in seasonal cycles were given in *Sheng et al.* (2001) and *Thompson et al*. (2007).

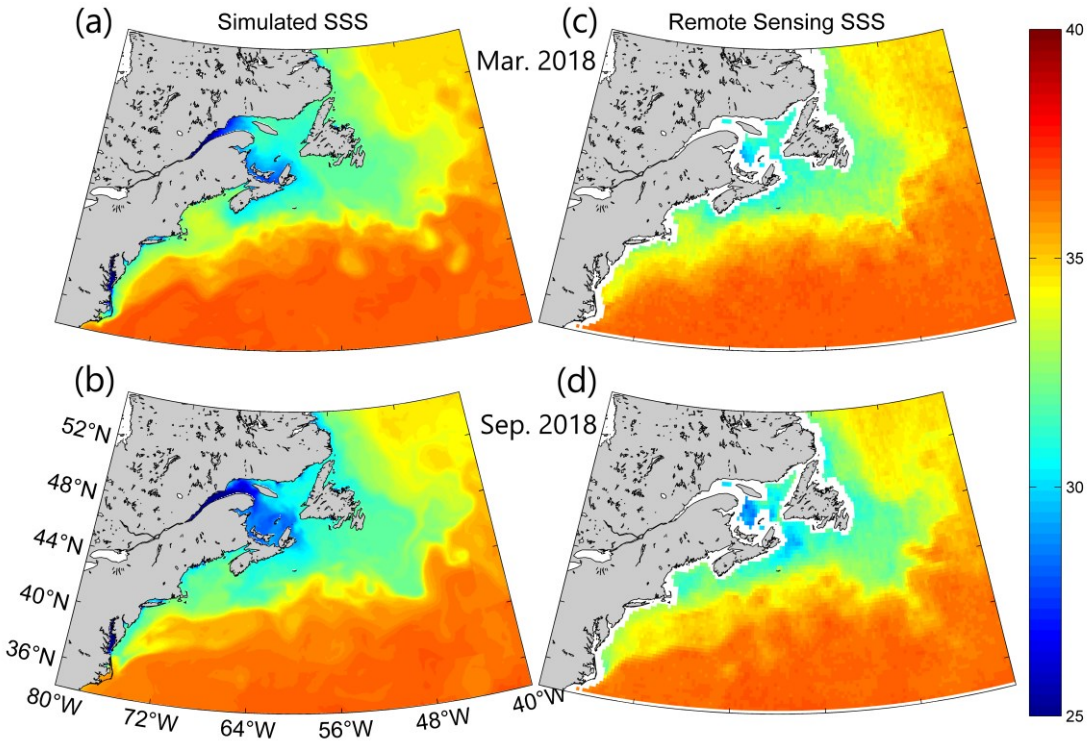

Figure 2.6. Monthly-mean SSS simulated by submodel L1 in (a) March and (c) September 2018. The monthly-mean remote sensing SSS data in (b) March and (d) September 2018 extracted from the Sea Surface Salinity Essential Climate Variable (ECV) dataset (version 1.8) produced by the European Space Agency's (ESA) Climate Change Initiative (CCI).

The monthly-mean SSS in March 2018 produced by submodel L1 ranges from 25 to 37 (psu) over the model domain (Figure 2.6a). The simulated March-mean SSS is relatively low and varies from 25 to 29 (psu) over the St. Lawrence Estuary (SLE) and coastal waters off PEI. Over the BoF, GoM, coastal and shelf waters of the ScS, NFS, LS, GB, and eastern GSL, the simulated March-mean SSS is generally between 30 and 34. Over deep ocean waters off

the seCS, the simulated March-mean SSS is relatively high and ranges from 34 to 37. Submodel L1 also generates some relatively fine-scale salinity front structures over the slope water regions of the ECS and deep ocean waters off the GB.

Figure 2.6c shows the monthly-mean SSS in September 2018 simulated by submodel L1. In this month, the simulated monthly-mean SSS ranges from 25 to 29 (psu) over most of the western GSL and coastal waters off Cape Breton Island. Over the western GSL and coastal waters off Cape Breton Island, the monthly-mean SSS is lower in September than in March 2018. Previous studies demonstrated that the SSS in the GLS, ScS and GoM is affected significantly by freshwater discharges from major rivers in the region including the SLR. Based on the monthly-mean discharge data constructed by the SLGO, the SLR had relatively larger freshwater discharges in March (1.7524×10^4 m^3 s^{-1}), April (1.5895×10^4 m^3 s^{-1}), May (1.7765×10^4 m^3 s^{-1}), and June (1.3418×10^4 m^3 s^{-1}) in 2018 than the counterparts in other months from December 2017 to December 2018. The numerical study made by Ohashi and Sheng (2013) demonstrated that the variability of freshwater flux from the SLE takes about 100 days to reach the Cabot Strait. Therefore, the relatively lower SSS over the western GSL and off Cape Breton Island in the summer months (in comparison with the counterpart during the winter) in 2018 is due mainly to the seaward transport of the relatively large discharges of the SLR during the spring season (particularly between March and June). In addition, the relatively weak vertical mixing and strong vertical stratification in the summer months (in comparison with the counterparts during the winter) also contribute partially to the seasonal SSS differences between winter and summer in this region.

The performance of submodel L1 of NGMS-seCS in simulating SSS is assessed by comparing simulated SSS fields (Figure 2.6a,c) with the satellite remote sensing SSS data extracted from the Sea Surface Salinity Essential Climate Variable (ECV) dataset (version 1.8) produced by the European Space Agency's (ESA) Climate Change Initiative (CCI)

(Figure 2.6b,d). A comparison of the left panels with the right panels in Figure 2.6 demonstrates that submodel L1 reproduces reasonably well the general large-scale features of monthly-mean SSS over the model domain in both March and September 2018. Submodel L1 reasonably reproduces the observed high SSS over deep ocean waters off the ECS and the observed low SSS over coastal and shelf waters of the ECS in these two months. Over the GSL, the simulated SSS (Figure 2.6a,c) is also comparable with the remote sensing data (Figure 2.6b,d), even though the remote sensing SSS data are unavailable near the coast of the GSL. Submodel L1 also has satisfactory skills in reproducing the observed monthly-mean SSS features associated with salinity fronts over the slope water regions of the seCS, GB, NFS, and LS. In both March and September 2018, the typical length scales and locations of monthly-mean salinity fronts produced by the NGMS-seCS are in general agreement with satellite data. It should be noted that there is no spectral nudging or data assimilation other than the semi-prognostic method applied in the top 30 m in the coupled model run using the NGMS-seCS.

Figure 2.7a shows the monthly-mean sea ice concentration (represented by fraction) in February 2018 simulated by submodel L1. Model results feature the high sea ice concentration over the LS, northeastern NFS, the SLE, Strait of Belle Isle, and coastal waters off western PEI. Over these sub-regions, the local ice production is large in winter months associated with strong negative heat flux (i.e., the net heat loss from the ocean surface to the atmosphere) and relatively low SSS in comparison with other subregions of the seCS. The freezing temperature points for sea ice are higher for lower salinity waters, leading to more local ice production. *Urrego-Blanco* (2014) demonstrated that both thermodynamics and sea ice dynamics play important roles in affecting the sea ice concentration in the GSL. Furthermore, over the LS and northern NFS, the sea ice conditions are also affected by the

southward advection of some Arctic and Sub- Arctic Sea ice equatorward carried by the Labrador Current in winter months (*Reeh*, 1985; *Mertz et al.*, 1993).

Figure 2.7a,b demonstrates that submodel L1 has satisfactory skills in reproducing the observed monthly-mean sea ice concentration over the LS, Strait of Belle Isle, northern GSL, and northeastern NFS. However, submodel L1 has large deficiencies in simulating the sea ice concentration over the southwestern GSL and coastal waters off Cape Breton Island and eastern PEI. The main reason for the large model deficiencies in simulating sea ice conditions is still under investigation. One possible reason is that the thermodynamics over these local areas may not be simulated well due to the deficiency in the parametrization of local vertical mixing. Another plausible reason is less accurate values of the net heat flux during the ice formation period.

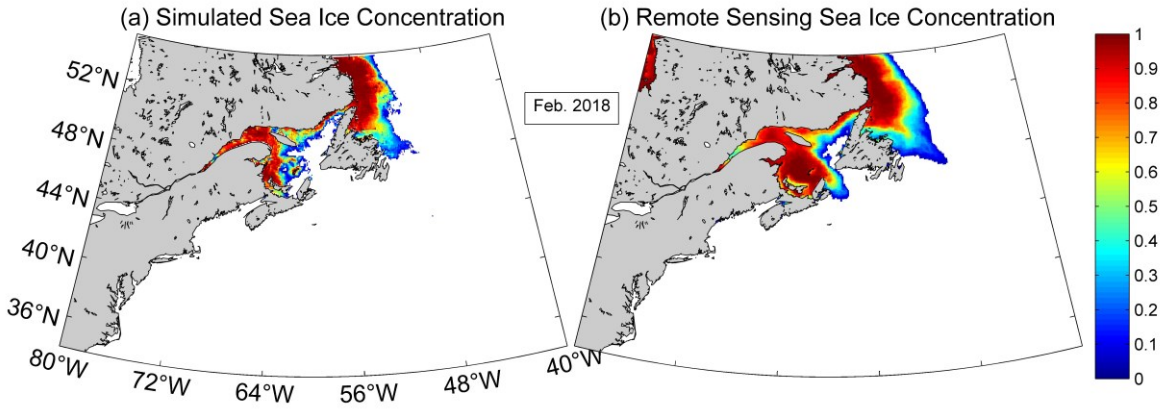

Figure 2.7. Monthly-mean sea ice concentration (in fraction) in February 2018 (a) produced by NGMS-seCS and (b) inferred from the daily GHRSST Level 4 CMC0.1deg Global Foundation Sea Surface Temperature Analysis (GDS version 2) dataset over the domain of submodel L1.

We next assess the performance of submodel L2 in simulating SST by comparing model results with remote sensing SST extracted from the daily GHRSST Level 4 CMC0.1deg Global Foundation Sea Surface Temperature Analysis (GDS version 2) dataset. Figure 2.8a shows the distribution of monthly-mean SST in February 2018 simulated by submodel L2. The simulated monthly-mean SST in this month is relatively cold and ranges from -2 °C to 5 °C over the ScS, GSL, BoF, and southwestern NFS. Over the GoM and slope water region of the ScS, the simulated February-mean SST ranges from 5 °C to 15 °C. Over deep ocean waters off the ScS and GoM, the simulated February-mean SST is warm and ranges from 15 °C to 21 °C. Submodel L2 also simulates some relatively fine-scale SST features associated with thermal fronts and the meandering of the slope water jet over the slope water region of the southern ScS and adjacent deep ocean waters.

Figure 2.8d shows the distribution of the monthly-mean SST in August 2018 simulated by submodel L2. In this month, the simulated monthly-mean SST is relatively cold and ranges from 10 °C to 20 °C over the northern GSL, BoF, and southwestern NFS. Over coastal waters of the ScS, the August-mean SST generally ranges from 14 °C to 21 °C. The cold SST over the BoF and coastal waters off Yarmouth is mainly due to the temperature vertical stratification in summertime and local strong tidal mixing. Over the western GoM, slope water regions of the ScS, and coastal waters off the PEI, the August-mean SST ranges from 20 °C to 25 °C. Over deep ocean waters off the southern ScS and GoM, the simulated monthly-mean SST is relatively warm and ranges from 25 °C to 28 °C. Submodel L2 also simulates some fine-scale SST features associated with local tidal mixing and topography over the Georges Bank.

The performance of submodel L2 in simulating SST is assessed by comparing simulated SST fields with remote sensing SST (Figure 2.8). Figure 2.8a,b demonstrates that

submodel L2 reasonably reproduces the general features of observed monthly-mean SST over the L2 model domain in February 2018. In particular, submodel L2 reproduces very well the observed cold SST over the GSL and coastal waters of the ScS and southwestern NFS and the observed warm SST over deep ocean waters off the southern ScS in February 2018. Submodel L2 also has certain skills in reproducing the observed monthly-mean SST features associated with thermal fronts and the meandering of the slope water jet over the slope water region of the southern ScS. The length scales and general locations of monthly-mean simulated and observed thermal fronts are highly comparable.

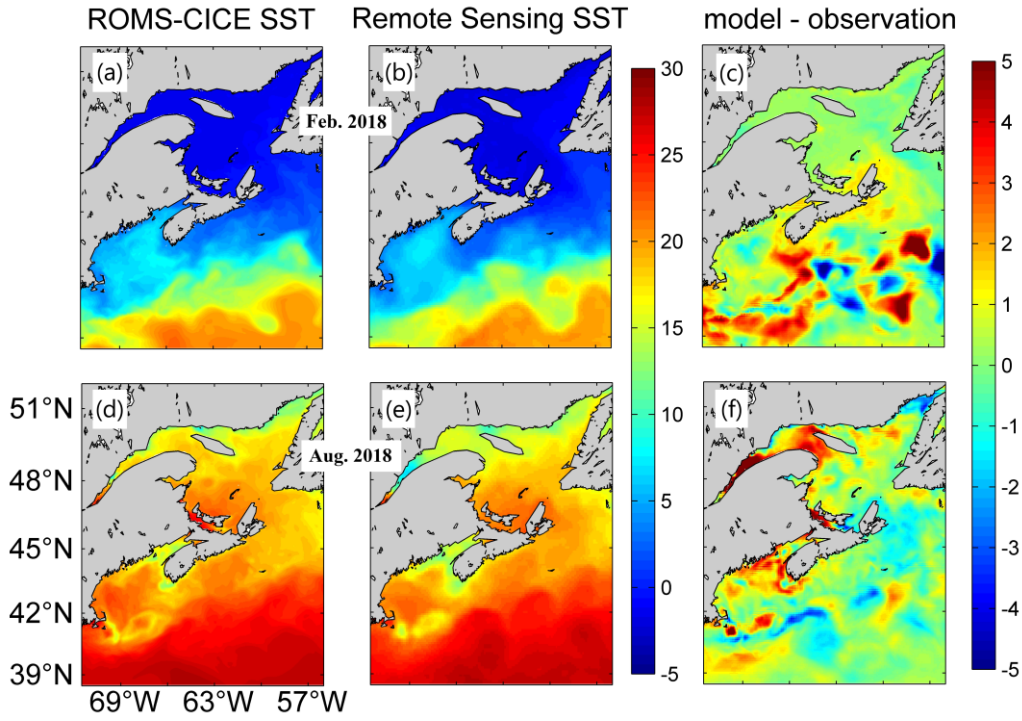

Figure 2.8. Monthly-mean SST in (a) February and (d) August 2018 calculated from results produced by submodel L2. Monthly-mean remote sensing SST in (b) February and (e) August 2018 are respectively calculated from daily remote sensing SST data in February and August 2018 over the domain of submodel L2. Monthly-mean SST differences in (c) February and (f) August 2018 are calculated by subtracting monthly-mean remote sensing SST (b and e) from monthly-mean simulated SST (a and d).

Figure 2.8c presents the differences between simulated (Figure 2.8a) and observed (Figure 2.8b) monthly-mean SST in February 2018. The main differences between the simulated and remote sensing February-mean SST are associated mainly with small-scale thermal front structures and meso-scale eddies over the slope water region of the southern ScS. It should be noted that no data assimilation is applied in submodel L2, except for the semi-prognostic method and the spectral nudging method (under 30 m). Over coastal waters off south Nova Scotia, the simulated SST is slightly higher (up to 1°C) than the remote sensing SST. One possible reason is the model deficiency in simulating wind-induced vertical mixing and upwelling/downwelling over inner shelf waters because of the relatively coarse horizontal resolution of wind forcing. Another possible reason is the combined effect of unresolved processes in the NGMS-seCS. Furthermore, the model deficiencies of submodel L1 affect the accuracy of submodel L2 through the open boundaries conditions of submodel L2, which are specified using the results produced submodel L1. As mentioned above, the satellite remote sensing data have relatively lower accuracy of SST over coastal and inshore waters than in the offshore deep waters (*Minnett et al.*, 2019; *Meneghesso et al.*, 2020).

An examination of Figure 2.8d,e demonstrates that submodel L2 reproduces reasonably well the general distribution of observed monthly-mean SST over the domain of submodel L2 in August 2018. In particular, submodel L2 reproduces very well the observed relatively cold SST over inshore waters of the northern GSL, the observed relatively warm SST over the southern GSL and coastal waters of the ScS and southwestern NFS, and the observed very warm SST over deep ocean waters off the southern ScS and GoM. Submodel L2 also reasonably reproduces SST cooling due to strong tidal mixing over the BoF and coastal waters off Yarmouth. Figure 2.8f presents the differences between the simulated (Figure 2.8d) and observed (Figure 2.8e) monthly-mean SST in August 2018. Over the SLE and northern GoM, submodel L2 overestimates the monthly-mean SST. One possible reason

is that the freshwater discharges and the temperature of freshwater runoffs over these areas are from the climatology, which may be different from their realistic values in this month. In addition, there are fine-scale thermal front structures over the SLE and northern GoM. The coupled circulation-ice modelling system has deficiencies in reproducing fine-scale thermal fronts since these frontal structures are highly nonlinear and could not be simulated realistically by any circulation model without data assimilation.

Due to limited in-situ observations below the sea surface over the whole domain of submodel L2, the performance of submodel L2 in simulating subsurface circulation and hydrography is assessed by comparing model results with the reanalysis data from the GLORYS 12V1 dataset. This dataset contains physical variables such as temperature, salinity, and currents produced by the NEMO model with assimilations of various satellite remote sensing data and in-situ observations (https://resources.marine.copernicus.eu). More details about the numerical modelling and data assimilations of the GLORYS 12V1 dataset are available on the reference website.

In February 2018, the monthly-mean simulated temperature (Figure 2.9a) at the subsurface (40 m) is relatively cold and generally ranges from 0 °C to 10 °C over the GoM, BoF, ScS, GSL, and southwestern NFS. Over shelf breaks and slope water regions of the ScS and GoM, submodel L2 generates some subsurface (40 m) temperature features associated with thermal fronts and the meandering of the slope water jet. The February-mean simulated temperature ranges from 10 °C to 15 °C at 40 m over these regions. Over deep ocean waters off the ScS and GoM, the February-mean simulated temperature at 40 m is warm and ranges from 15 °C to 22 °C.

The August-mean simulated temperature (Figure 2.9c) at 40 m is relatively cold and varies from 1 °C to 10 °C over the GSL, western GoM, ScS, and southwestern NFS. Over

the BoF, southern GoM, and slope water regions of the ScS and GoM, the simulated August-mean subsurface (40 m) temperature generally ranges from 10 °C to 20 °C. Over deep ocean waters off the ScS and GoM, the simulated monthly-mean temperature is warm and ranges from 20 °C to 26 °C at 40 m. Submodel L2 also simulates some fine-scale temperature features associated with tidal mixing and topography over the Georges Bank and some fine-scale thermal front structures over slope water regions of the ScS and GoM at 40 m.

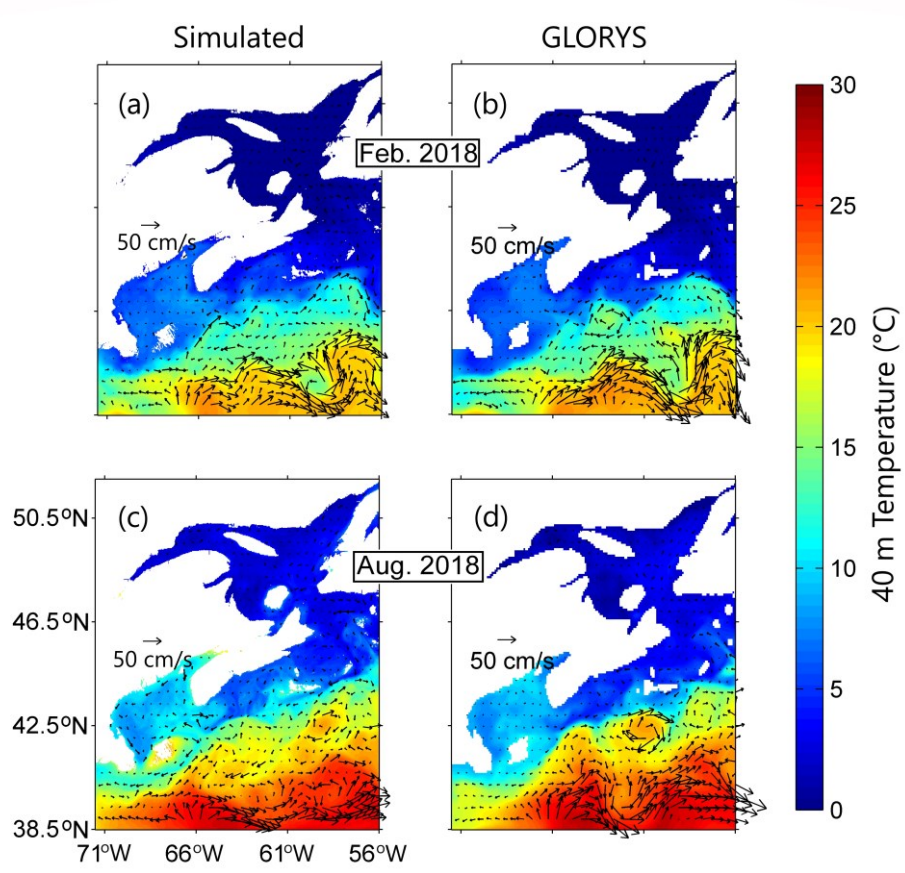

Figure 2.9. Monthly-mean subsurface (40 m) temperature and circulation simulated by submodel L2 in (a) February and (c) August 2018. The monthly-mean reanalysis temperature and circulation at 40 m in (b) February and (d) August 2018 are calculated from the daily-mean reanalysis data of GLORYS of over the domain of submodel L2. For clarity, velocity vectors are plotted at every 12th model grid point.

Figure 2.9a,c reveals that submodel L2 generates many recognized features of monthly-mean circulation at 40 m over the GoM, ScS and adjacent deep ocean waters in February and August 2018. At 40 m of the deep ocean waters off the ScS, submodel L2 generates the intense ocean currents from the Gulf Stream. Submodel L2 also simulates relatively large currents along with the shelf breaks of the ScS and GoM at the subsurface, due mainly to the effect of topographic steering. In addition, submodel L2 generates relatively large southwestward alongshore circulation at 40 m over inner shelf waters of the ScS.

The performance of submodel L2 in simulating temperature and circulation is assessed by comparing the model results (Figure 2.9a,c) with the reanalysis data (Figure 2.9b,d) at 40 m. A comparison between Figure 2.9a,b demonstrates that submodel L2 reproduces very well the general features of temperature and circulation at 40 m in February 2018. Specifically, submodel L2 reproduces reasonably well the warm subsurface temperature over the deep ocean waters off the southern ScS and the cold subsurface temperature over the GSL and coastal waters of the domain of submodel L2 (i.e., GoM and coastal waters of the ScS and southwestern NFS) in February 2018. Submodel L2 also has satisfactory skills in generating the monthly-mean thermal fronts and the temperature and circulation features associated with the meandering of the slope water jet at 40 m over slope water region of the southern ScS. The length scales and general locations of monthly-mean thermal fronts in Figure 2.9a,b are comparable, although the fine-scale features of thermal fronts in these two figures are not in a good agreement.

Figure 2.9c,d reveals that submodel L2 simulates adequately the well-known features of temperature and circulation at 40 m over the domain of submodel L2 in August 2018. In particular, submodel L2 reproduces reasonably well the warm temperature over the deep ocean waters, relatively warm temperature over the slope water regions, and cold temperature over the GSL and coastal waters of the ScS and southwestern NFS at 40 m in August 2018.

The length scales of thermal fronts in Figure 2.9c,d are comparable, but the general locations and fine-scale features of thermal fronts in these two figures are not in accord.

There are some differences between the monthly-mean simulated and reanalysis temperature at 40 m over several local areas (e.g., the BoF, coastal waters of Yarmouth, and GeB) in this month. Over the BoF, GeB, and coastal waters off Yarmouth, the August-mean temperature differences at 40 m between model results and reanalysis data are mainly due to strong tides. Tides are specified through open boundary conditions in the coupled circulation-ice modelling system, while the numerical modelling applied in the GLORYS 12V1 dataset excludes tidal forcing. As a result, the reanalysis data do not represent well the subsurface warming due to strong tidal mixing over the BoF, GeB, and coastal waters off Yarmouth during the summer.

In February and August 2018, the simulated monthly-mean circulation (Figures 2.9a,c) at 40 m are highly comparable with the reanalysis data (Figure 2.9b,d). A comparison of the left and right panels of Figure 2.9 demonstrates that submodel L2 has satisfactory skills in reproducing the magnitudes and general directions of the large currents from the Gulf Stream. Submodel L2 also reasonably reproduces some relatively large currents along shelf breaks and over inner shelf waters (e.g., the Nova Scotia Current) of the ScS. There are some differences between the monthly-mean simulated and reanalysis circulation at 40 m over several local areas of the domain of submodel L2 in February and August 2018. The differences in the meso-scale eddies and detailed circulation features of the Gulf Stream between the left and right panels of Figure 2.9 are due mainly to the lack of data assimilation in the NGMS-seCS. In addition, as mentioned earlier, the numerical model used in producing the GLORYS dataset does not include the tides, and the GLORYS reanalysis data do not represent well the monthly-mean circulation features associated with tides. Furthermore, the

model errors, different atmospheric forcing, unresolved processes in numerical models also affect the accuracy of simulated ocean circulation.

The satellite remote sensing data of SSS shown in Figure 2.6c,d have a coarse horizontal resolution of about 50 km and are unavailable over most inner shelf waters of the domain of submodel L2. As a result, model results of surface salinity and circulation produced by submodel L2 are validated against the GLORYS reanalysis dataset. Figure 2.10a presents the monthly-mean surface salinity and circulation in February 2018 simulated by submodel L2. The February-mean simulated SSS is relatively low and in the range from 25 to 31 over the SLE, southern GSL, and inner shelf waters of the ScS. Over the GoM, the February-mean simulated SSS is typically about 33 (psu). Over slope water region of the ScS, the simulated February-mean SSS varies from 31 to 35. Over deep ocean waters off the ScS and GoM, the simulated monthly-mean SSS is high and generally over 35. Over the slope water region of the southern ScS and adjacent deep ocean waters, submodel L2 simulates some monthly-mean salinity fronts and fine-scale SSS features associated with the meandering slope water jet.

Figure 2.10c presents the distributions of monthly-mean surface salinity and currents in August 2018 simulated by submodel L2. The simulated August-mean SSS is relatively low and varies from 25 to 29 over the western GSL and coastal waters off Cape Breton Island. The relatively low August-mean SSS over these areas is due mainly to the increased river discharges (caused by ice melting on land) during the spring and the horizontal advection of river runoffs from the SLR. Over the eastern GSL, southwestern NFS, GoM, and coastal waters of the ScS (except for coastal waters off the Cape Breton Island), the August-mean simulated SSS generally ranges from 30 to 32. Over slope water regions of the ScS, the simulated August-mean SSS ranges from 31 to 34. Over deep ocean waters off the ScS and GoM, the simulated August-mean SSS is high and generally over 35. Submodel L2 also

simulates some fine-scale monthly-mean SSS features associated with salinity fronts over the GSL, GoM, slope water regions of the southern ScS, and deep ocean waters off ScS and GoM.

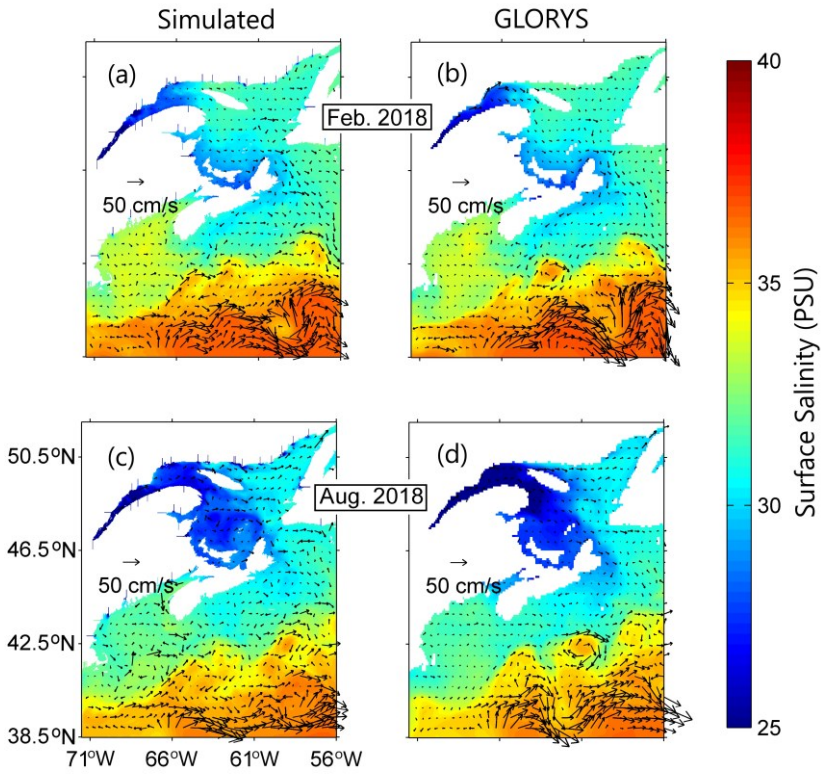

Figure 2.10. Monthly-mean salinity and currents at the sea surface simulated by submodel L2 in (a) February and (c) August 2018. The monthly-mean reanalysis salinity and currents at the sea surface in (b) February and (d) August 2018 are respectively calculated from daily-mean GLORYS reanalysis circulation and salinity data in February and August 2018 over the domain of submodel L2. For clarity, velocity vectors are plotted at every 12th model grid point.

Figure 2.10a,c also reveals that submodel L2 simulates many well-known monthly-mean surface circulation features over the GoM, ScS and adjacent deep ocean waters in February and August 2018. Over deep ocean waters off the ScS, submodel L2 simulates large monthly-mean surface currents from the Gulf Stream. Submodel L2 also simulates relatively large

monthly-mean surface circulation along the shelf break of the GoM (caused mainly by topographic steering). Furthermore, submodel L2 simulates relatively large monthly-mean currents induced by strong tidal currents over the BoF, GoM, and coastal waters off Yarmouth.

An examination of Figure 2.10a,b demonstrates that both submodel L2 and GLORYS reanalysis reasonably reproduce the general features of February-mean salinity and circulation at the sea surface over the domain of submodel L2. Submodel L2 reproduces the high February-mean SSS over the deep ocean waters off the GoM and southern ScS and the low February-mean SSS over the SLE, southern GSL, and inner shelf waters of the ScS. Submodel L2 also has certain skills in reproducing the February-mean SSS features associated with salinity fronts and meandering slope water jets over slope water regions. The length scales of salinity fronts in Figure 2.10a,b are highly comparable. However, the actual positions fine-scale features of salinity fronts from model results and reanalysis data are not in accord.

Figure 2.10c,d demonstrates that both submodel L2 and GLORYS reanalysis reproduces reasonably well the general features of surface salinity and circulation over the domain of submodel L2 in August 2018. Submodel L2 reproduces the high SSS over deep ocean waters off the GoM and southern ScS, relatively high SSS over the eastern GSL and coastal waters of the ScS (except for coastal waters off the Cape Breton Island) and southwestern NFS, and low SSS over the western GSL and coastal waters off Cape Breton Island in August 2018. The length scales of surface salinity fronts shown in Figure 2.10c,d are comparable. It should be noted that the actual positions and shapes of fine-scale surface salinity fronts produced by submodel L2 and GLORYS reanalysis differ significantly. The differences between the August-mean simulated and reanalysis SSS also occur over several local areas (e.g., the BoF, coastal waters off Yarmouth, and St. Lawrence Estuary). Over the BoF and coastal waters off Yarmouth, the August-mean SSS differences between the model results and reanalysis data are due mainly to strong tidal mixing (more details about the

effects of tides are available in the Process Study section of Chapter 3). As mentioned earlier, the numerical model used in the GLORYS reanalysis does not include tidal forcing and the GLORYS reanalysis does not represent the temporal and spatial variability of hydrography and circulation induced by tidal forcing.

Over the SLE and adjacent waters, large differences occur in August-mean SSS between the NGMS-seCS results and GLORYS reanalysis data (Figure 10), with several reasons. Firstly, tides are relatively strong over these areas, with maximum tidal elevations over 2 m. Strong tidal mixing significantly reduces the vertical gradients of salinity during the summer. Therefore, tides increase the SSS over these areas. As mentioned above, the tidal forcing is included in driving the NGMS-seCS, but not included in generating the GLORYS reanalysis. Secondly, the methodology used in the NGMS-seCS for specifying freshwater discharges from the SLR and other rivers in the study region (section 2.2) differs from the methodology used in the GLORYS reanalysis. Freshwater discharges from the SLR significantly affect the SSS over the SLE and adjacent coastal waters. These different methodologies can result in the differences in salinity distribution over these areas between NGMS-seCS and GLORYS reanalysis. Thirdly, large differences occur between the NGMS-seCS and GLORYS reanalysis in local topography, horizontal resolution, and horizontal eddy diffusivities over the SLE and adjacent waters. These large differences also affect the circulation and hydrography over these areas.

The large-scale features of monthly-mean surface circulation in February and August 2018 simulated by submodel L2 are comparable with the reanalysis data (Figure 2.10). In particular, submodel L2 has satisfactory skills in reproducing the large surface currents associated with the Gulf Stream over the deep ocean water off the southern ScS and the relatively large surface currents associated with the southeastward outflow from the GSL along the Laurentian Channel. As mentioned above, with/without tidal forcing, different

atmospheric forcing, model errors and different sub-grid scale mixing parameterizations used in the NGMS-seCS and GLORYS reanalysis all contribute to differences in 3D currents shown in Figure 2.10.

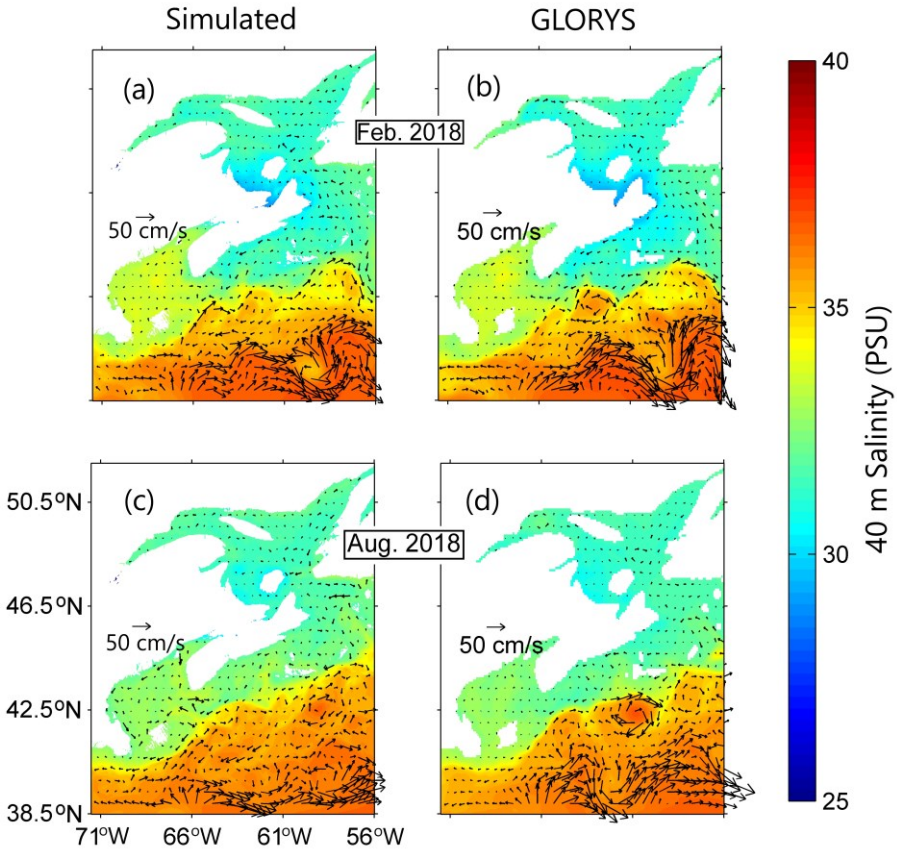

Figure 2.11. Monthly-mean salinity and circulation at 40-meter depth simulated by submodel L2 in (a) February and (c) August 2018. Monthly-mean reanalysis salinity and circulation at 40-meter depth in (b) February and (d) August 2018 are respectively calculated from daily reanalysis salinity and circulation data in February and August 2018 over the domain of submodel L2. For clarity, velocity vectors are plotted at every 12th model grid point.

To assess the performance of submodel L2 in simulating subsurface salinity, the simulated salinity at 40 m is compared with reanalysis data from the GLORYS dataset. Figure 2.11a shows the monthly-mean subsurface salinity and circulation at 40 m in February 2018 simulated by submodel L2. Over subsurface (40 m) waters of the GSL, ScS, and southwestern NFS, the February-mean simulated salinity is relatively low and generally ranges from 30 to 32. Over shelf breaks and slope water regions of the ScS and GoM, the simulated February-mean salinity ranges from 32 to 35 at the depth of 40 m. Over deep ocean waters off the ScS and GoM, the simulated February-mean salinity at 40 m is high and generally over 35. Over slope water regions of the ScS and GoM, submodel L2 simulates some fine-scale salinity front structures at 40 m and the subsurface salinity features due to the meandering of slope water jets.

Figure 2.11c presents distributions of the August-mean simulated salinity and circulation at 40 m in 2018. The August-mean simulated salinity at 40 m is relatively low and generally ranges from 31 to 33 over the GSL, southwestern NFS, ScS, BoF, and GoM. Over slope water regions of the ScS and GoM, the subsurface (40 m) monthly-mean simulated salinity generally ranges from 33 to 36. Over shelf breaks of the ScS and GoM, submodel L2 simulates some fine-scale monthly-mean salinity features associated with salinity fronts and the meandering of slope water jets at 40 m. Over deep ocean waters off the ScS and GoM, the monthly-mean simulated salinity at 40 m is high and generally over 36.

The performance of submodel L2 in simulating subsurface salinity is assessed by comparing model results (Figure 2.11a,c) with reanalysis data (Figure 2.11b,d). Figure 2.11a,b demonstrates that submodel L2 reasonably reproduces the general salinity distribution at 40 m over the domain of submodel L2 in February 2018. Submodel L2 reasonably reproduces the high subsurface (40 m) salinity over deep ocean waters off the southern ScS and GoM and the low subsurface (40 m) salinity over the GSL, GoM, and

coastal waters of the ScS and southwestern NFS in February 2018. Submodel L2 also has certain skills to reproduce the February-mean salinity features associated with salinity fronts and meandering slope water jets at 40 m over slope water regions of the southern ScS and GoM. The length scales and general positions of salinity fronts produced by submodel L2 and GLORYS reanalysis are comparable (Figure 2.11a,b), with significant differences in the fine-scale features of salinity fronts with reasons given above.

Figure 2.11c,d demonstrates that submodel L2 also reasonably reproduces the general salinity features at 40 m in August 2018. Submodel L2 reasonably reproduces the high subsurface (40 m) salinity over deep ocean waters off the ScS and GoM and the low subsurface (40 m) salinity over the GSL, southwestern NFS, ScS, BoF, and GoM in August 2018. The length scales and positions of salinity fronts produced by submodel L2 and GLORYS reanalysis (Figure 2.11c,d) are comparable, with major differences in the fine-scale features of salinity fronts. Over the BoF and coastal waters off Yarmouth, the August-mean simulated salinity at 40 m produced by submodel L2 is slightly higher than the reanalysis data due mainly to the strong tidal mixing, which was not included in the numerical model in generating the GLORYS reanalysis dataset as mentioned earlier.

2.4 Summary and Conclusions

A coupled circulation-ice modelling system for the southeastern Canadian Shelf (NGMS-seCS) was presented in this chapter. This coupled modelling system was developed by the Regional Ocean Modelling Group at Dalhousie University based on the Regional Ocean Modeling System (ROMS, www.myroms.org) and Los Alamos Sea Ice Model (CICE, *Hunke et al*., 2017). The NGMS-seCS has three submodels, with the outermost submodel (L1) for the southeastern Canadian shelf (seCS) and the innermost submodel (L3) for the coastal waters off southwest Nova Scotia. Model results of temperature, salinity, circulation,

and sea surface elevations were compared with the available satellite remote sensing data, reanalysis, and in-situ observations. It was demonstrated that NGMS-seCS has satisfactory skills in reproducing tidal elevations at Halifax and Yarmouth tidal gauge stations. NGMS-seCS also has satisfactory skills in reproducing non-tidal sea surface elevations at these two locations, with the model performance quantitively comparable to the shelf circulation models in simulating non-tidal surface elevations (*Shan*, 2010; *Shan and Sheng*, 2012). The co-phases and co-amplitudes of two major tidal constituents (M_2 and K_1) produced by NGMS-seCS were shown to agree well with the barotropic tidal results produced by the Oregon State University Tidal Inversion System (with horizontal resolution of 1/6º) and previous numerical studies (*Han et al.*, 2010; *Wang et al.*, 2020). In comparison with the satellite remote sensing data and ocean reanalysis, NGMS-seCS was found to have reasonable skills in reproducing the general distributions of monthly-mean temperature, salinity, and circulation at the sea surface and subsurface during the winter (February and March) and summer months (August and September) of 2018. NGMS-seCS also has satisfactory skills in reproducing the observed monthly-mean sea ice concentration over the Labrador Shelf, Strait of Belle Isle, northern GSL, and northeastern Newfoundland Shelf. The nested-grid modelling system, however, has large deficiencies in simulating the sea ice concentrations over the southeastern GSL and coastal waters off Cape Breton Island and eastern PEI, which deserves more investigations.

CHAPTER 3

NUMERICAL STUDY OF HYDRODYNAMICS OVER COASTAL WATERS OF THE SCOTIAN SHELF

Circulation and hydrography over the Scotian Shelf (ScS) are affected by many forcing functions, including tides, winds and buoyancy forcing, as mentioned in the previous chapters. Model results in four numerical experiments with different external forcing in 2018 are examined in this chapter to quantify the effects of wind forcing and tides on temperature, salinity, and currents over coastal waters of the ScS. The coupled circulation-ice modelling system based on the ROMS and the CICE (NGMS-seCS) is used here. More details of the model setup and validation were discussed in Chapter 2.

The first numerical experiment is the Control Run (CR, Table 3.1), in which the NGMS-seCS is driven by all external forcing discussed in Chapter 2, including tidal forcing, wind stress, atmospheric pressures, the net heat/freshwater fluxes at the sea surface, and river discharges. The second numerical experiment is case NoWind (NW), which is the same as Control Run except for turning off winds in both submodels L2 and L3 (Figure 3.1). The third numerical experiment is case NoL3Wind, which is the same as Control Run except for turning off wind forcing in submodel L3. The fourth numerical experiment is case NoTide (NT), which is the same as Control Run except for turning off tidal forcing.

For convenience, the wind forcing applied over the domain of submodel L2 is termed as L2Wind. Similarly, the wind forcing applied only over the domain of submodel L3 is termed as L3Wind. Model results from NW and NoL3Wind are used to examine the effects

of local and non-local winds on hydrography and currents over coastal waters off southwest Nova Scotia. It should be noted that the latent and sensible heat fluxes are proportional to the wind speed, resulting in the absence of latent and sensible heat fluxes in case NW and NoL3Wind. Since these numerical experiments are implemented to investigate the wind and tidal effects over the coastal waters, we still apply the semi-prognostic method from *Sheng et al.* (2001) and the spectral nudging method from *Thompson et al.* (2007) in submodels L1 and L2 to reduce the systematic model errors in the seasonal cycle of large-scale circulation.

A new coordinate system (Figure 3.1b) is used in this chapter to examine the spatial variability of model results over coastal waters of the southwestern ScS. The x-axis of this new coordinate system is in the alongshore direction and positive to be northeastward, and the y-axis is in the cross-shelf direction and positive to be northwestward. In addition, model results along three transects (PP', EE', and PQ) are discussed in this chapter. Transect PP' originates from Liverpool Bay of Nova Scotia and is parallel to the y-axis. Transect EE' is a north-south transect originating from Yarmouth of Nova Scotia. Transect PQ is the extension of Transect PP' over the domain of submodel L2.

Table 3.1. List of four numerical experiments using the NGMS-seCS.

Numerical Experiment	Tidal forcing	Wind forcing in submodel L2	Wind forcing in submodel L3	Other forcing
CR	Yes	Yes	Yes	Yes
NW	Yes	No	No	Yes
NoL3Wind	Yes	Yes	No	Yes
NT	No	Yes	Yes	Yes

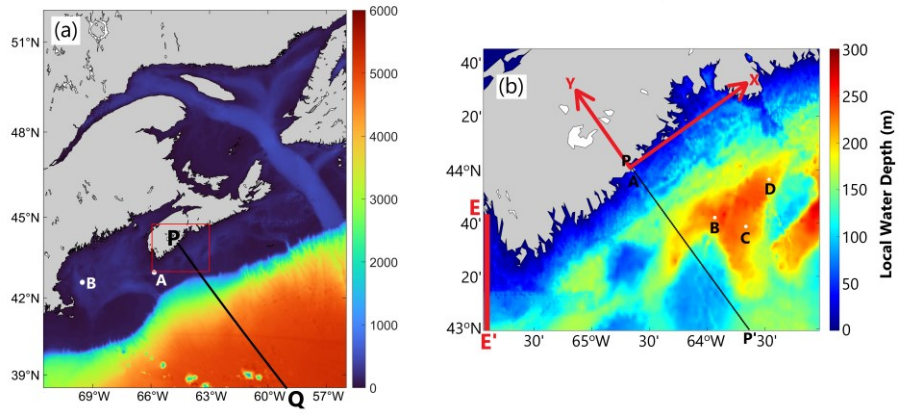

Figure 3.1. Major topographic features over domains of (a) submodel L2 and (b) submodel L3. The color image represents local water depths. The red box in the left panel marks the L3 domain. The right panel shows a new coordinate system and two transects used to examine model results in this chapter. Transect PP' is a cross-shelf transect originating from Liverpool Bay. Transect PQ is the extension of transect PP' over the domain of submodel L2. Transect EE' is a north-south transect originating from Yarmouth, which is close to the western open boundary of submodel L3. Points A, B, C and D in the right panel represent locations of in-situ observations for the oxygen model validation to be discussed in Chapter 4; Points A and B in the left panel represent locations of chlorophyll concentration and respiration rate observations from *Packard and Christensen* (2004) to be discussed in Chapter 4.

3.1 Roles of Winds over the L2 Domain

To examine the role of wind forcing over coastal waters of the ScS, we compare the monthly mean results produced by submodel L2 in cases CR and NW in August 2018. We also calculate differences in the August-mean model results between the two cases to quantify the role of wind forcing on the 3D circulation and hydrography. It should be noted that winds are normally weaker in summer months than in winter months over the ScS. Nevertheless, the wind forcing plays a very important role in affecting the 3D currents and hydrography

over coastal waters of the ScS in summer, particularly during the upwelling/downwelling-favorable wind events.

The monthly-mean currents and hydrography in August 2018 produced by the NGMS-seCS in case CR (Control Run) have been discussed in Chapter 2. For a direct comparison, Figure 3.2 presents the monthly-mean temperature and currents in both cases CR and NW in August 2018 at the surface (Figure 3.2a,b) and 40 m (Figure 3.2d,e) respectively over the L2 domain (i.e., GSL, ScS, GOM, southwestern NFS, and adjacent deep ocean waters). The August-mean model results in both cases CR and NW (Figure 3.2a,b) show the relatively low SST over the BoF, Georges Bank, and coastal waters off Yarmouth due mainly to strong tidal mixing over these areas, and relatively high SST over the southwestern GLS, central ScS and central GOM. In comparison with model results in case CR, the August-mean simulated SST in case NW is warmer almost everywhere in the L2 domain, due mainly to the unrealistically weak vertical mixing and strong temperature vertical stratification.

Figure 3.2c presents differences in the monthly-mean SST ($\Delta\bar{T}_0^{CR-NW}$) and sea surface currents ($\Delta\vec{\bar{U}}_0^{CR-NW}$) over the L2 domain between cases CR and NW in August 2018. The values of $\Delta\bar{T}_0^{CR-NW}$ are negative over the L2 domain except for some local areas, with the maximum negative value of about to -7 °C. This is expected since the vertical mixing in the surface mixed layer without wind forcing in case NW is unrealistically weak and the thermal energy generated by the positive surface heat fluxes in summer months is trapped mainly in the very thin surface layer, resulting in unrealistically warm sea surface waters in case NW. It should be noted that the values of $\Delta\bar{T}_0^{CR-NW}$ are positive over several local areas, including the BoF, Georges Bank and coastal waters off Yarmouth (Figure 3.2c). Over these local areas,

wind-induced horizontal mixing/advection and the large positive net heat flux associated with winds reduce significantly the SST cooling generated by strong tidal mixing and advection.

The effect of wind forcing on currents can be categorized into the direct and indirect types. The direct effect of wind forcing includes the wind-driven currents known as the Ekman currents and shelf waves excited by winds. The indirect effect of winds includes the density-driven currents generated by winds and wind-induced modulations of nonlinear circulation features such as eddies and fronts.

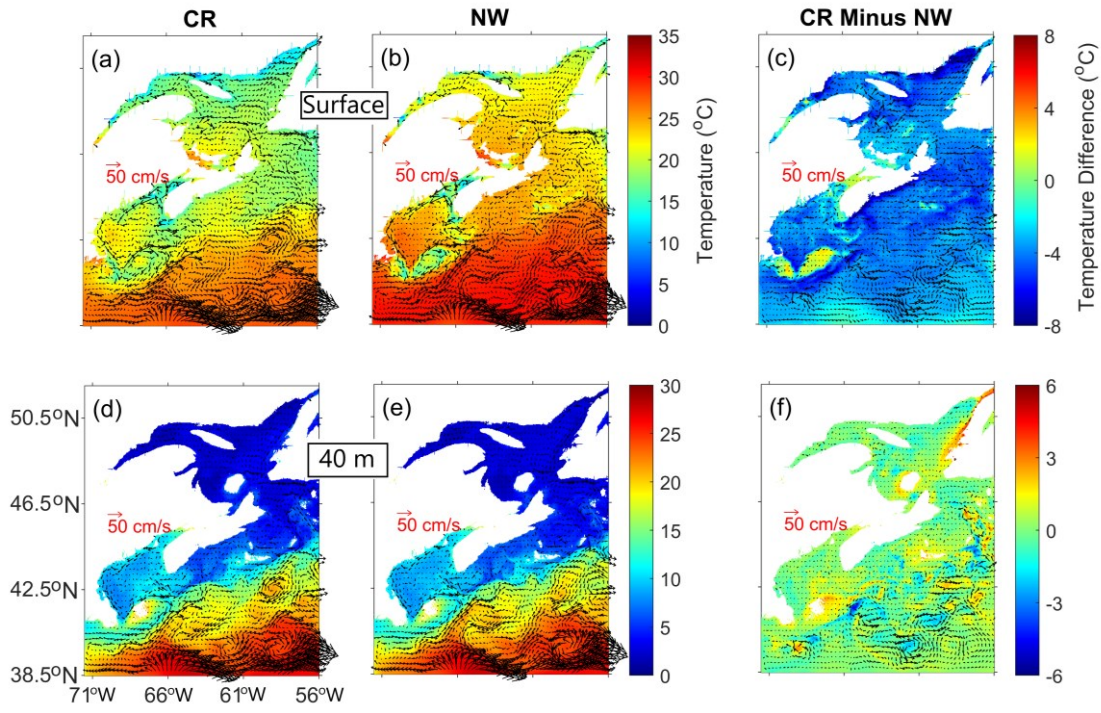

Figure 3.2. Monthly-mean temperature and currents in August 2018 produced by submodel L2 at (a,b) the sea surface and (d,e) subsurface of 40 m over the L2 domain in cases (a,d) CR and (b,e) NW. Differences in temperature and currents between cases CR and NW at the (c) sea surface and (f) 40 m. For clarity, velocity vectors are plotted at every 12th model grid point.

The values of $\Delta\vec{\overline{U}}_0^{CR-NW}$ in August 2018 (Figure 3.2c) are relatively small and about 10 cm/s over the ScS and GoM, and relatively large and up to 20 cm s^{-1} in the GSL. Large values of $\Delta\vec{\overline{U}}_0^{CR-NW}$ also occur over the slope water region off the ScS and GoM. The non-zero values of $\Delta\vec{\overline{U}}_0^{CR-NW}$ over these shelf waters demonstrate the direct effect of wind forcing in affecting the monthly-mean surface currents in August 2018. It should be noted that large values of $\Delta\vec{\overline{U}}_0^{CR-NW}$ in the slope water region and also over the western GSL between Anticosti Island and PEI are associated mainly with wind-induced modulations of meanders/rings/eddies, rather than the wind-driven currents.

The large-scale features of August-mean subsurface temperature and currents at 40 m are highly comparable in both cases CR (Figure 3.2d) and NW (Figure 3.2e). This can be explained by the fact that the wind stress is generally weak and the thermal stratification in the vertical is strong in the top 10 m in summer months. As a result, the wind stress does not affect significantly the sub-surface currents and hydrography below the surface mixed layer in summer months except for coastal waters during the upwelling/downwelling favorable strong wind events. Figure 3.2f presents the differences in the monthly-mean subsurface (40 m) temperature ($\Delta\overline{T}_{40}^{CR-NW}$) and currents ($\Delta\vec{\overline{U}}_{40}^{CR-NW}$) between cases CR and NW in August 2018. Different from values at the sea surface, $\Delta\overline{T}_{40}^{CR-NW}$ in August 2018 are positive over the L2 domain, except for areas with cold-water patches over slope waters off the ScS and GoM (Figure 3.2f). The positive values of $\Delta\overline{T}_{40}^{CR-NW}$ mean that subsurface waters are cooler in summer months without wind forcing in case NW, in comparison with the counterparts in case CR. This can be explained by the fact that the heat at the sea surface could not penetrate easily downward in summer months in case NW due to the weak vertical mixing and strong stratification if the wind forcing is turned off. There are many small-scale features with

negative values of $\Delta\bar{T}_{40}^{CR-NW}$ over the slope water region off the ScS and GoM shown in Figure 3.2f. These noticeable negative values of $\Delta\bar{T}_{40}^{CR-NW}$ indicate the effect of wind forcing on mesoscale eddies over the slope water region.

The values of $\Delta\vec{\bar{U}}_{40}^{CR-NW}$ shown in Figure 3.2f are relatively small over the coastal and shelf waters of the L2 domain, due to the facts that winds are weak in August and the direct effect of wind forcing occurs mainly in the top 10 m. By comparison, the values of $\Delta\vec{\bar{U}}_{40}^{CR-NW}$ are relatively large over the slope water region off the ScS and GOM, which are associated mainly with the wind-induced modulations in intensities and positions of meanders and warm-core and cold-core eddies. As mentioned earlier, the warm-core eddies (anticyclonic with the clockwise rotation), which pinch off from the north side of the Gulf Stream, entrap warm (and salty) waters and transport them north to the ECS (*Webb*, 2019, p. 201; *Zhang and McGillicuddy*, 2020). Since the wind forcing used in driving submodels L1 and L2 is in large-scale (with a horizontal resolution of about 32 km), the large-scale wind forcing tends to reduce some meso-scale eddies. As a result, the wind forcing generally makes the warm-core eddies transport less warm (and salty) waters to the ECS in case CR, in comparison with the counterparts in case NW. In addition, the wind forcing modifies the positions and intensities of these warm-core eddies. Therefore, the values of $\Delta\bar{T}_{40}^{CR-NW}$ associated with the counterclockwise $\Delta\vec{\bar{U}}_{40}^{CR-NW}$ shown in Figure 3.2f are negative. For the same reason, Figure 3.2f shows positive values of $\Delta\bar{T}_{40}^{CR-NW}$ over the slope water areas with clockwise $\Delta\vec{\bar{U}}_{40}^{CR-NW}$.

As mentioned earlier, the wind forcing results in the sea surface warming over the Georges Bank, BoF, and coastal waters off Yarmouth during the summer through wind-induced horizontal mixing/advection and latent and sensible heat fluxes. As a result, L2Wind enhances the subsurface (40 m) warming induced by strong tidal mixing over these areas (i.e.,

the Georges Bank, BoF, and coastal waters off Yarmouth). Over the eastern GSL, the August-mean surface currents in case CR feature relatively large eastward currents (toward the northwest shore of Newfoundland), which do not appear in case NW. This implies that L2Wind induces some coastal downwelling events off northwest Newfoundland in August 2018 and thus significantly warms up subsurface waters over the area (Figure 3.2f).

Figure 3.3 presents the monthly-mean salinity in cases CR (Figure 3.3a,d) and NW (Figure 3.3b,e) at the sea surface (Figure 3.3a,b) and 40 m (Figure 3.3d,e) over the L2 domain in August 2018. In comparison with results in case CR, the August-mean SSS over the SLE and northwestern GSL in case NW (Figure 3.3b) is much lower than the counterpart in CR (Figure 3.3a). This can be explained by the important role of wind-induced vertical mixing in case CR. The SLR, which is one of the most important freshwater sources in the GSL, had a monthly-mean discharge rate of about 1.0954×10^4 m^3 s^{-1} in August 2018 (from SLGO data). As mentioned earlier, the vertical mixing in case NW is unrealistically weak, in comparison with case CR. The large amount of freshwater runoff from the SLR is mainly trapped in the thin surface layer in case NW, resulting in unrealistically fresh surface waters over the SLE and northwestern GSL, in this case. Figure 3.3c,f presents the differences in the August-mean salinity between CR and NW at the sea surface ($\Delta\bar{S}_0^{CR-NW}$) and 40 m ($\Delta\bar{S}_{40}^{CR-NW}$) over the study region. The values of $\Delta\bar{S}_0^{CR-NW}$ in August 2018 are positive over the L2 domain, except for slope waters off the ScS and GoM (Figure 3.3c). These positive values of $\Delta\bar{S}_0^{CR-NW}$ indicate that surface waters are fresher in summer months without wind forcing in case NW, in comparison with the counterparts in case CR. Physically, this can be explained by the weak vertical mixing and strong stratification in case NW in the surface mixed layer in summer months without wind forcing.

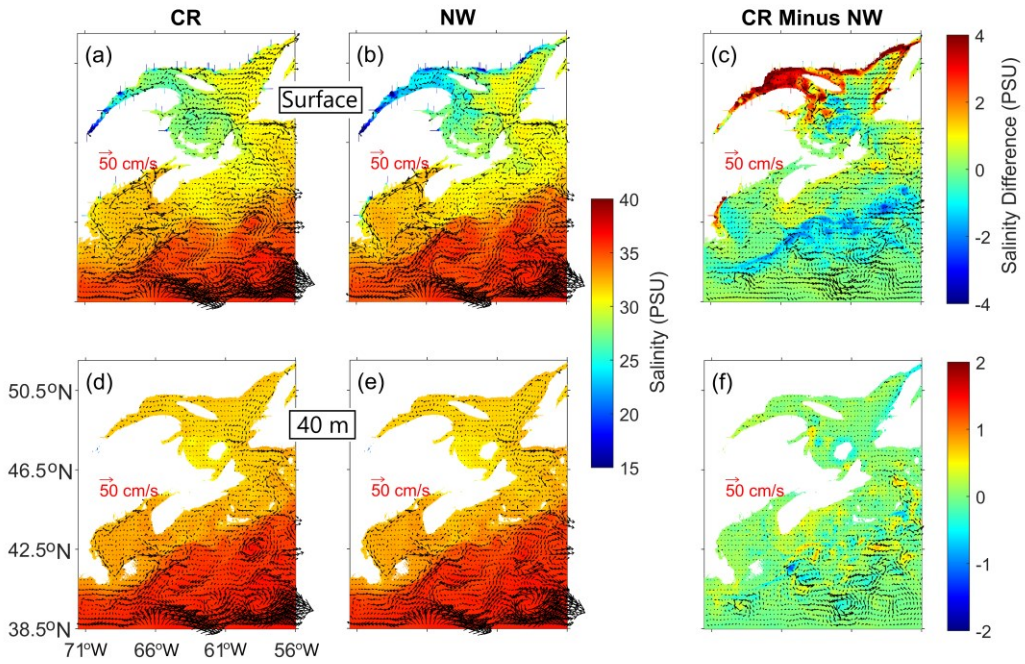

Figure 3.3. Same as Figure 3.2, except for the August-mean salinity (upper panels) at the sea surface and (lower panels) at 40 m.

The values of $\Delta\bar{S}_0^{CR-NW}$ (Figure 3.3c) are also positive and large over inshore waters of the northern GSL and western GoM. This can be explained by the effect of wind forcing in vertical mixing, seaward spreading of river runoffs, and horizontal mixing and advection over these coastal waters. Because of ice melting on land and the relatively large precipitation, freshwater discharges and fluxes are generally large over estuary areas in the summer. Winds reduce the retentions of these low-salinity waters through wind-induced mixing and advection and thus result in the large and positive values of $\Delta\bar{S}_0^{CR-NW}$ over some estuary areas of the L2 domain in summer months. Over the slope water region off the ScS and GoM,

by comparison, $\Delta\bar{S}_0^{CR-NW}$ in August 2018 features a noticeable negative-value zone (Figure 3.3c) due to the wind effect.

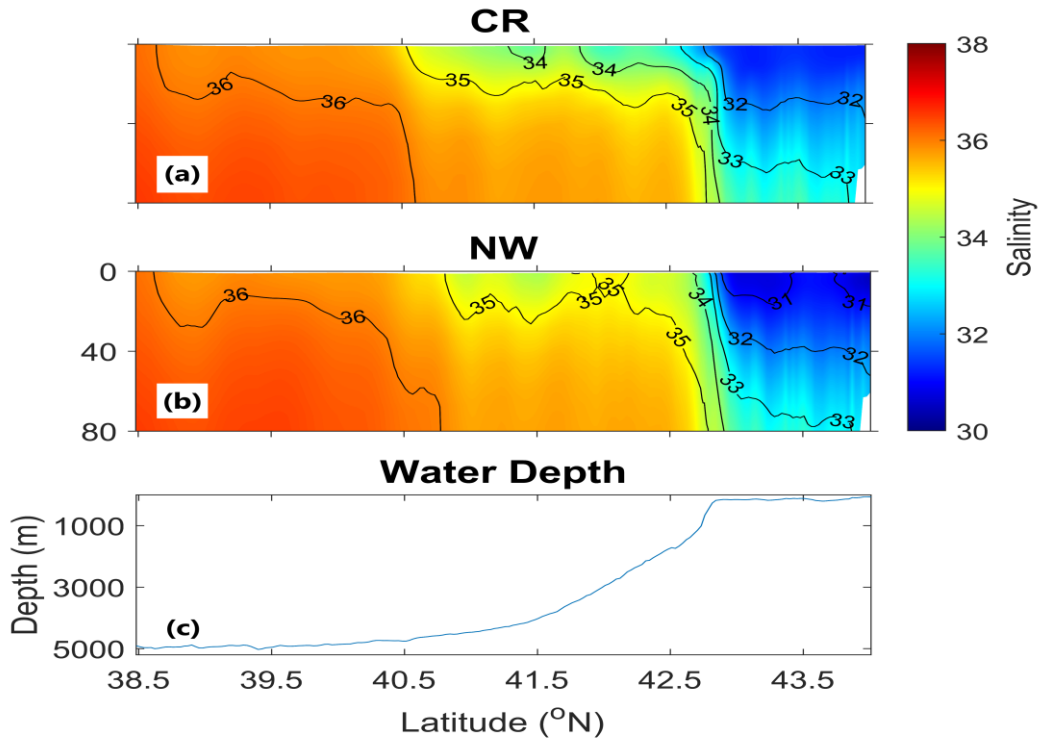

Figure 3.4. Vertical distributions of monthly-mean salinity in the top 80 m produced by submodel L2 in cases (a) CR and (b) NW along cross-shelf transect PQ (marked in Figure 3.1a). The bottom panel shows the profile of water depth along transect PQ.

To further demonstrate the role of wind forcing in generating the negative values of $\Delta\bar{S}_0^{CR-NW}$ over the shelf slope region, we examine the salinity distribution along PQ, which is a cross-shelf transect over the western ScS (Figure 3.1) in the two cases. The vertical profiles of August-mean salinity in the top 80 m along PQ (marked in Figure 3.1a, the extension of Transect PP' over the L2 domain) are shown in Figure 3.4a for case CR and

Figure 3.4b for case NW. The salinity front in the top 20 m is much broader over the shelf slope (between 41.5 ºN and 42.7 ºN, Figure 3.4c) of PQ in case CR than the counterpart in case NW, which is due mainly to the effect of wind-induced horizontal mixing and advection. As a result, the August-mean SSS over the shelf slope region in case CR (Figure 3.4a) is lower than the counterpart in case NW (Figure 3.4b). For the same reason, negative values of $\Delta\bar{S}_0^{CR-NW}$ also occur over other slope water regions of the L2 domain (Figure 3.3c).

3.2 Roles of Local and Remote Wind Forcing over the L3 Domain

To quantify the roles of the local and non-local wind forcing on the 3D currents and hydrography over the ScS, model results produced by submodel L3 in cases CR, NW, and NoL3Wind are analyzed. In this study, the local wind forcing case is defined as the one in which wind forcing is used only in driving submodel L3 without any wind forcing for submodel L2. The remote wind forcing case is defined the one in which wind forcing is used only in driving submodel L2 without wind forcing in driving submodel L3. Based on these definitions, differences in model results between cases CR and NoL3Wind can be used to quantify the role of local winds (i.e., L3Wind) over the L3 domain. Differences in results produced by submodel L3 between cases NoL3Wind and NW can be used to quantify the effects of non-local winds (i.e., L2Wind) on hydrography and ocean currents over coastal and shelf waters of the western ScS.

The monthly-mean SST in August 2018 produced by submodel L3 in case CR is between 14 ºC and 18 ºC near the coast and over coastal and deep waters off Yarmouth and about 20 ºC over the rest of the L3 domain (Figure 3.5a). The narrow strip of relatively cool surface waters of about 16 ºC near the coast shown in Figure 3.5a are associated with wind-induced coastal upwelling in summer (*Garrett and Loucks*, 1976; *Dever et al.*, 2018; *Scrosati*

and Ellrich, 2020). Figure 3.5a,b demonstrates that the August-mean SST in 2018 in case NoL3Wind is significantly warmer than the counterpart in case CR over the interior of the L3 domain. In particular, the model in case NoL3Wind does not generate a narrow strip of relatively cool surface waters near the coast of the western ScS. The main differences in August-mean SST between CR and NoL3Wind result from the effect of wind-induced mixing, which is included in CR but not in NoL3Wind.

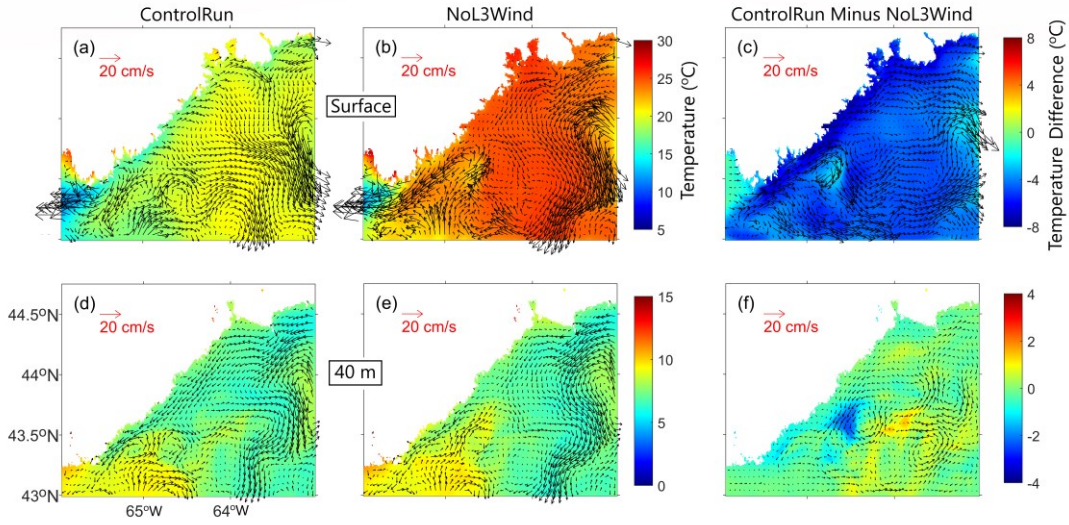

Figure 3.5. Monthly-mean temperature and currents in August 2018 based on model results produced by submodel L3 in (a,d) CR and (b,e) NoL3Wind at (a,b) the sea surface and (d,e) subsurface of 40 m over the L3 domain. Right panels present the differences in August-mean temperature and currents between CR and NoL3Wind at (c) the surface and (f) subsurface (40 m). For clarity, velocity vectors are plotted at every 6th model grid point.

The August-mean surface currents over the L3 domain in case CR (Figure 3.5a) are characterized by a weak alongshore (roughly northeastward) coastal jet of about 5 cm s^{-1} at the coast, and offshore currents in the deep water of the inshore shelf of the western ScS. In

addition, the NGMS-seCS in case CR also generates the western portion of a large-size intense cyclonic gyre over the middle shelf adjacent to the eastern open boundary (the southwest portion of Emerald Basin) and northern portion of a large-size intense anti-cyclonic gyre over the middle shelf adjacent to the south open boundary of the L3 domain (Figure 3.5a). The August-mean surface currents in case NoL3Wind (Figure 3.5b) differ significantly from the counterparts in case CR (Figure 3.5a) over the interior of the L3 domain, due mainly to the effect of the local wind forcing in the momentum equation, which is included in case CR but not in case NoL3Wind. Over the areas close to the open boundaries of the L3 domain, the August-mean SST and surface currents in case NoL3Wind are highly similar to the counterparts in case CR, due to horizontal advection and mixing of outside water masses and momentum through the open boundaries of the L3 domain in case NoL3Wind.

Figure 3.5c presents the differences in August-mean temperature and currents produced by submodel L3 at the sea surface between CR and NoL3Wind ($\Delta\bar{T}_0^{CR-NoL}$, $\Delta\vec{\bar{U}}_0^{CR-NoL}$), which represent changes in monthly-mean SST and surface currents in August 2018 generated by the local wind forcing. The values of $\Delta\bar{T}_0^{CR-NoL}$ generated by the local wind forcing are negative and about -5.5 ºC over the interior of the L3 domain. The local wind forcing also generates alongshore (roughly northeastward) monthly-mean currents of about 10 cm s^{-1} over the inner shelf of the western ScS (Figure 3.5c), and broad and eastward surface currents with several small-scale gyres over the middle shelf of the western ScS in August 2018. Physically, the strong temperature stratification in summer is established in the surface mixed layer due to the large and positive surface heat fluxes over the ScS and other coastal and shelf waters of the ECS. The vertical mixing induced by the local wind forcing mixes the warm surface waters downward in summer months. The local wind forcing also generates currents in the surface mixed layer and coastal upwelling in summer months over

the ScS. Furthermore, the local wind forcing also modifies the path of the Nova Scotia Current and thus alters the fine-scale features of hydrography and circulation in August 2018 over the L3 domain.

The August-mean subsurface (40 m) temperature produced by submodel L3 in case CR is relatively warm and about 9 ºC over coastal waters off Yarmouth (i.e., southwestern area of the L3 domain), and nearly uniform and about 7 ºC over the rest of the L3 domain (Figure 3.5d). The August-mean subsurface (at 40 m) currents in case CR are characterized by a broad alongshore (southwestward) coastal current of about 8 cm s^{-1} entering the L3 domain over the northern section of the eastern open boundary (Figure 3.5d). This coastal current splits into two branches, with one branch continuing to flow southwestward near the coast and the second branch veering cyclonically to flow southward to exit the L3 domain through the eastern section of the southern open boundary. There are several recirculation gyres following the bottom topography over the L3 domain (Figure 3.5d). *Loder et al.* (1997) and *Hannah et al.* (2001) demonstrated that the flows over the ScS have clockwise (counterclockwise) circulation tendencies over the shallow (deep) areas. The topographic-scale recirculation features shown in Figure 3.5d are generally consistent with the previous finding related to topographic steering from *Loder et al.* (1997) and *Hannah et al.* (2001). In particular, submodel L3 in case CR reproduces the north portion of the relatively intense clockwise gyre (associated with shallow water depths, shown in Figure 3.1b) near the south open boundary (between 65.0 ºW and 64.5 ºW), the relatively weak large-size clockwise gyre over middle shelf waters (between 64.5 ºW and 64.0 ºW and between 43 ºN and 43.5 ºN) close to the south open boundary, and the intense large-size counterclockwise gyre (associated with deep topography) near the eastern open boundary at 40 m. These monthly-mean gyres generally following the bottom topography are partly due to topographic steering of throughflow, with some contributions from tidal rectification and local baroclinic

hydrodynamics (*Hannah et al.*, 2001). This indicates significant effects of bottom topography and topographic steering to the spatial variability of meso-scale circulation and cross-shore meanders over the southwestern ScS.

The August-mean subsurface temperature and currents in case NoL3Wind are highly similar to the counterparts in case CR over the deep waters of the inner shelf of the western ScS (Figure 3.5d,e), with some differences in the alongshore (roughly southwestward) coastal currents over the inner shelf waters. Similar to model results in case CR, submodel L3 also simulates these clockwise and counterclockwise gyres associated with the bottom topography in case NoL3Wind. The cyclonic flow around Emerald Basin (over middle shelf waters close to the eastern open boundary) is of great importance to the hydrodynamic connectivity between the eastern and western portions of the ScS, while there is an offshore turning of the southwestward coastal current close to the north section of the eastern open boundary of the L3 domain (*Han et al.*, 1997).

Figure 3.5f presents the differences in monthly-mean temperature and currents produced by submodel L3 at 40 m between cases CR and NoL3Wind ($\Delta\bar{T}_{40}^{CR-NoL}$, $\Delta\vec{\bar{U}}_{40}^{CR-NoL}$). The local wind forcing generates several small-scale gyres with magnitudes of about 5 cm/s. The local wind forcing also generates several small-scale patches of positive and negative values of $\Delta\bar{T}_{40}^{CR-NoL}$ (Figure 3.5f). It should be noted that both $\Delta\bar{T}_{40}^{CR-NoL}$ and $\Delta\vec{\bar{U}}_{40}^{CR-NoL}$ are smaller than $\Delta\bar{T}_{0}^{CR-NoL}$ and $\Delta\vec{\bar{U}}_{0}^{CR-NoL}$ respectively, indicating that the local wind forcing plays a minor role in the subsurface hydrodynamics below 40 m in comparison with hydrodynamics in the surface mixed layer.

The August-mean SSS in 2018 over the L3 domain produced by submodel L3 in case CR is relatively high and about 32.5 (psu) in the offshore waters off Yarmouth (i.e., the area

adjacent to the southwestern corner of the L3 domain), and relatively low and about 31.5 (psu) over the rest of the L3 domain (Figure 3.6a). An examination of Figure 3.6a,b demonstrates that the August-mean SSS in 2018 in case NoL3Wind is relatively lower than the counterpart in the CR over the L3 domain, due to the effect of vertical mixing generated by the local wind forcing, which is included in case CR but not in case NoL3Wind.

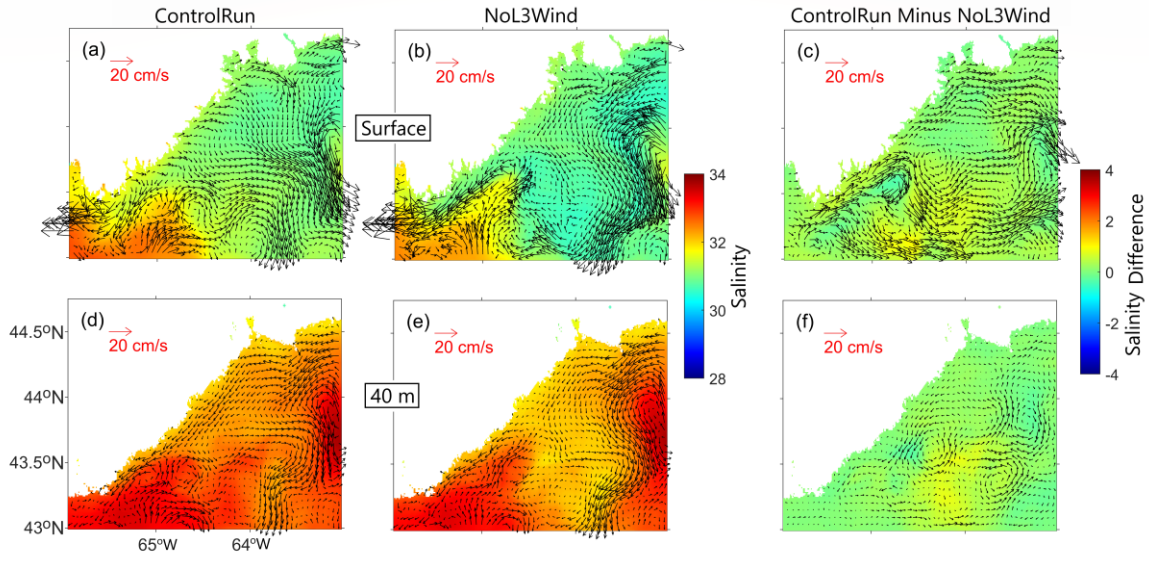

Figure 3.6. Monthly-mean salinity and currents in August 2018 based on model results in (a,d) CR and (b,e) NoL3Wind at (a,b) the sea surface and (d,e) subsurface of 40 m over the L3 domain. Right panels show differences in August-mean salinity and currents between CR and NoL3Wind at (c) the surface and (f) subsurface (40 m). For clarity, velocity vectors are plotted at every 6th model grid point.

Figure 3.6c demonstrates that the differences in the August-mean SSS between case CR and case NoL3Wind ($\Delta\bar{S}_0^{CR-NoL}$) are positive and about 0.7 (psu) over the L3 domain, except for areas with the anticyclonic gyres (Figure 3.6c). The positive values of $\Delta\bar{S}_0^{CR-NoL}$ represent the effect of vertical mixing generated by the local wind forcing, which is the same as $\Delta\bar{T}_0^{CR-NoL}$ shown in Figure 3.5c. The negative values of $\Delta\bar{S}_0^{CR-NoL}$ are generated by

downwelling associated with the anticyclonic gyres (*Mizobata et al.*, 2002; *Schütte and Karstensen*, 2016).

We next examine the role of remote wind forcing on the hydrodynamics over the coastal and shelf waters of the western ScS. Figure 3.7a,b presents the monthly-mean temperature and ocean currents at the sea surface over the L3 domain in August 2018 in cases NoL3Wind and NW. The August-mean SST results in both cases NoL3Wind and NW are highly similar over the L3 domain, with noticeable differences over areas adjacent to open boundaries of submodel L3. As mentioned earlier, the August-mean SST without the wind-induced vertical mixing in NoL3Wind is significantly warmer than the results in case CR (Figure 3.5a,b). This implies that the August-mean SST over the L3 domain is affected significantly by the local wind forcing. The remote wind forcing plays a minor role in the August-mean SST shown in Figure 3.7a,b. It should be noted that the 3D fields of temperature and salinity are affected by the shelf waves generated remotely by non-local wind forcing. In both cases NoL3Wind and NW, shelf waves generated by wind forcing over the L1 domain propagate into submodels L2 and L3, affecting hydrography and circulation over the southwestern ScS. Nevertheless, shelf waves generated by L2Wind are present in case NoL3Wind but absent in case NW. The propagation of these shelf waves (generated by L2Wind) can modify circualtion and hydrography over coastal and shelf waters of the ScS (*Cutchin and Smith*, 1973; *Allen*, 1976; *Smith and Schwing*, 1991; *Danielson et al.*, 2014).

The August-mean surface currents in case NW (Figure 3.7b) differ significantly from the counterparts in case NoL3Wind (Figure 3.7a) and in case CR (Figure 3.5a). The August-mean surface currents in case NW are characterized by a strong throughflow running westward from the northern section of the eastern open boundary which veers southward and exits from the eastern section of the southern open boundary of the L3 domain (Figure 3.7b). The recirculation gyres over the middle shelf water and the southwestern portion of the L3

domain in case NW (Figure 3.7b,e) (e.g., the anticyclonic gyre show in Figure 3.7e) also differ from the counterparts in case NoL3Wind (Figure 3.7a,d) and in case CR (Figure 3.5a,d). It should be noted that the model results in NoL3Wind include the effect of shelf waves generated by the remote wind forcing (produced by submodel L2), which is not included in the results in case NW.

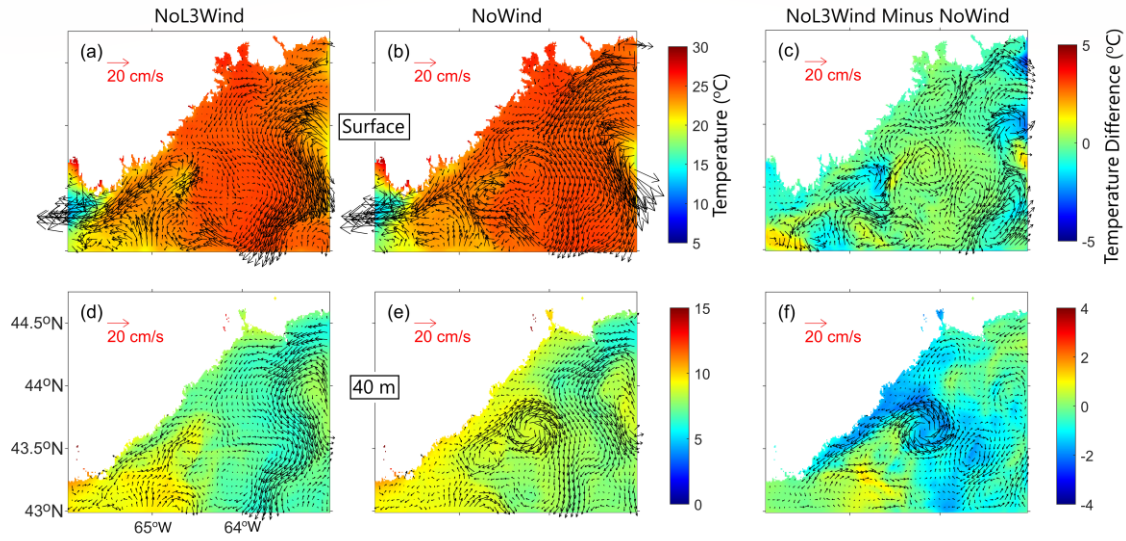

Figure 3.7. Monthly-mean temperature and currents in August 2018 based on model results produced by submodel L3 in (a,d) NoL3Wind and (b,e) NW at (a,b) the sea surface and (d,e) subsurface of 40 m over the L3 domain. Right panels show differences in August-mean temperature and currents between NoL3Wind and NW at (c) the surface and (f) subsurface (40 m). For clarity, velocity vectors are plotted at every 6th model grid point.

Figure 3.7c presents differences in the August-mean SST and surface currents over the L3 domain between case NoL3Wind and case NW ($\Delta\bar{T}_0^{NoL-NW}$, $\Delta\vec{\bar{U}}_0^{NoL-NW}$), which represent the role of remote wind forcing in generating the August-mean SST and surface currents over the L3 domain. The field of $\Delta\vec{\bar{U}}_0^{NoL-NW}$ features many small-scale circulation features

associated with the influence of shelf waves generated by remote wind forcing (Figure 3.7c). These shelf waves enter the coastal and shelf waters of the western ScS through the open boundaries of the L3 domain. The values of $\Delta\bar{T}_0^{NoL-NW}$ are small over the L3 domain except for areas with small-size cyclonic and anticyclonic gyres and areas adjacent to open boundaries of the L3 domain (Figure 3.7c).

The August-mean subsurface temperature and currents at 40 m in case NW (Figure 3.7e) are similar to the results in case NoL3Wind (Figure 3.7d), except for the presence of an intense anticyclonic gyre over the central area of the L3 domain in case NW and existence of the narrow southwestward coastal jet in case NoL3Wind. Figure 3.7f shows the differences in the August-mean subsurface temperature and currents at 40 m between case NoL3Wind and case NW ($\Delta\bar{T}_{40}^{NoL-NW}$, $\Delta\vec{\bar{U}}_{40}^{NoL-NW}$). Both the fields of $\Delta\bar{T}_{40}^{NoL-NW}$ and $\Delta\vec{\bar{U}}_{40}^{NoL-NW}$ have relatively large values, with significant spatial variability, indicating the importance of the remote wind forcing for hydrodynamics and hydrography in the layers below the surface mixed layer.

Figure 3.8 shows the vertical distributions of August-mean temperature and salinity in 2018 on transect PP' based on results produced by submodel L3 in three cases: CR, NoL3Wind and NW. The model in case CR generates the realistic distributions of August-mean temperature and salinity along this transect, with three layers in the vertical which include a warm and fresh surface layer in the top ~10 m, a relatively cold and fresh intermediate layer between 20 m and 80 m and a slightly warm and salty bottom layer below 80 m (Figure 3.8a,d). The three-layer system for temperature is usually well-established between the late spring and early autumn (*Smith et al.*, 1978). The August-mean thermocline along transect PP' in case CR is nearly horizontal and at about 10-15 m over the middle shelf (beyond about 50 km away the coast), tilts up over the inner shelf, and reaches the surface

near the coast (Figure 3.8a). The tilts of the August-mean thermocline and 31.5-salinity layer over the inner shelf (Figure 3.8a,d) are generated by coastal upwelling induced by the northeastward winds.

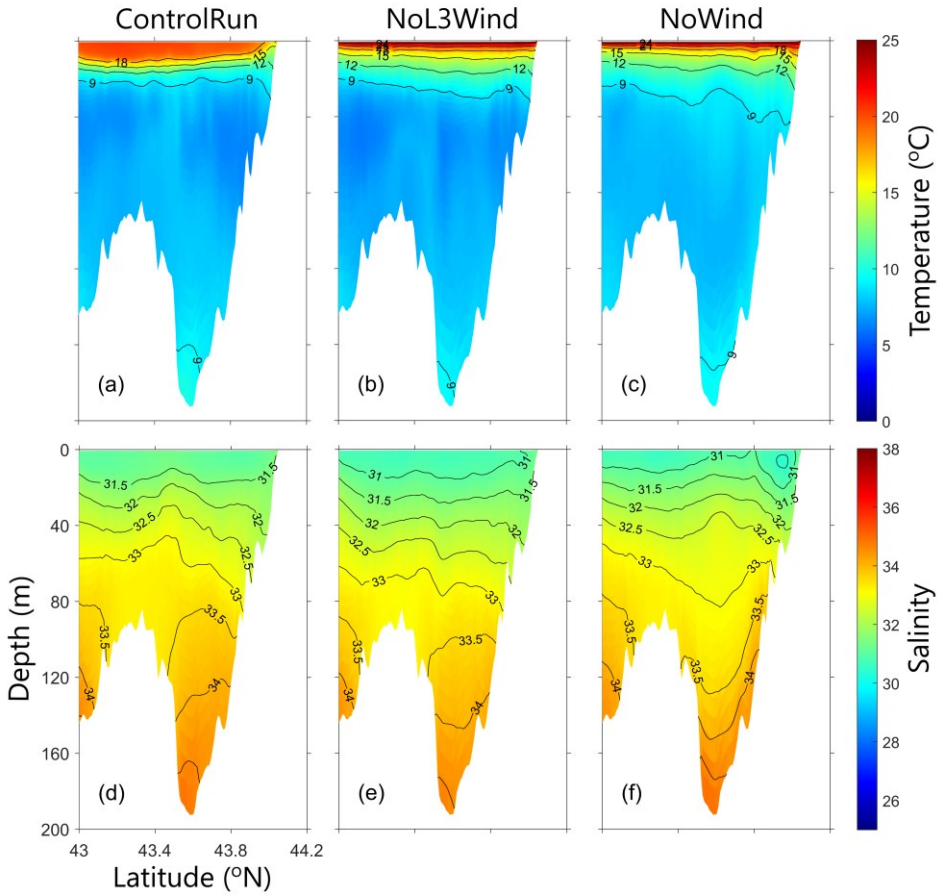

Figure 3.8. Vertical profiles of August-mean temperature (upper panels) and salinity (lower panels) in 2018 along transect PP' (marked in Figure 3.1b) based on model results in (a,d) case CR, (b,e) case NoL3Wind, and (c,f) case NoWind.

In comparison with results shown in Figure 3.8a, the August-mean thermohalines on transect PP' in cases NoL3Wind and NW are unrealistically shallow over the middle shelf

(Figure 3.8b,c), due to the exclusion of vertical mixing induced by the local wind forcing in these two cases. Furthermore, the August-mean thermohalines in cases NoL3Wind and NW do not tilt up over the inner shelf due to the absence of coastal upwelling induced by the local surface winds. Below 30 m, the vertical distributions of August-mean temperature and salinity along PP' in case NoL3Wind (Figure 3.8b,e) are very similar to the counterparts in case CR (Figures 3.8a,d). By comparison, the August-mean temperature and salinity below 30 m along transect PP' in case NW (Figure 3.8c,f) have vertical distributions different from the counterparts in case CR (Figure 3.8a,d). This indicates the important role of horizontal advection generated by the remote wind forcing for temperature and salinity distributions in the intermediate and bottom layers over the coastal and shelf waters of the western ScS.

The above analyses demonstrated the important roles of local and remote wind forcing in generating the August-mean circulation and hydrography over the coastal and shelf waters of the ScS. The local and remote wind forcing also affects significantly the 3D circulation and hydrography over the ECS at short timescales particularly during storm wind events such as winter storms and tropical storms (*Sheng et al.*, 2006; *Wang and Sheng*, 2016).

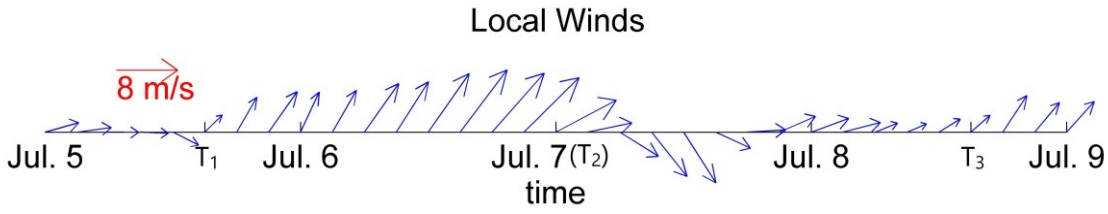

Figure 3.9. Time series of the area-mean wind velocity vectors averaged at all wet points over the L3 domain. Letters T_1, T_2 and T_3 denote respectively specific times before (15:00 UTC on 5 July), during (0:00 on 7 July), and after (15:00 on 8 July) a strong wind event in July 2018.

In early July 2018, a strong wind event occurred over the ScS, GoM, GSL and adjacent waters. We will examine the model results during this event to demonstrate the role of wind forcing in the 3D hydrodynamics over the southern ScS during this event. Figure 3.9 presents time series of wind speeds averaged over areas with wet-points of the L3 domain during the strong wind event. The area-mean wind speeds over the southern ScS were weak on 5 July, reached a maximum of about 12 m s^{-1} on 7 July, and died down significantly on the next day (Figure 3.9).

Figure 3.10 presents the horizontal distributions of surface winds over the L2 domain at three specific times during this strong wind event. At T_1 (15:00 on 5 July, 2018) before the event, surface winds were relatively weak and nearly northeastward over the southern ScS (i.e., the L3 domain, which is the area marked by the black box in Figure 3.10a) and much weaker over the eastern ScS and adjacent waters. The surface winds at this time were relatively strong (about 6 m s^{-1}) and nearly eastward in the deep ocean waters to the south of the ScS, and also relatively strong (about 4 m s^{-1}) and northeastward in the GoM (Figure 3.10a). At T_2 (00:00 on 7 July, 2018) during the event, the surface winds were very strong and nearly northeastward on the ScS and adjacent slope waters (Figure 3.10b). The maximum speed of surface winds on the ScS reached about 12 m s^{-1}. In the GoM and GSL, the surface winds at this time were also relatively strong and about 7 m s^{-1}. At T_3 (15:00 on 8 July) after the event, the winds were relatively weak over the western ScS, GoM and adjacent waters, and relatively strong over the eastern ScS, GSL and adjacent waters (Figure 3.10c).

Model results produced by submodel L3 in case CR are analyzed to examine the hydrodynamical responses to this strong wind event over coastal and shelf waters off southwest Nova Scotia. Figure 3.11 presents instantaneous currents, temperature and salinity at the sea surface over the L3 domain at these specific times in early July 2018.

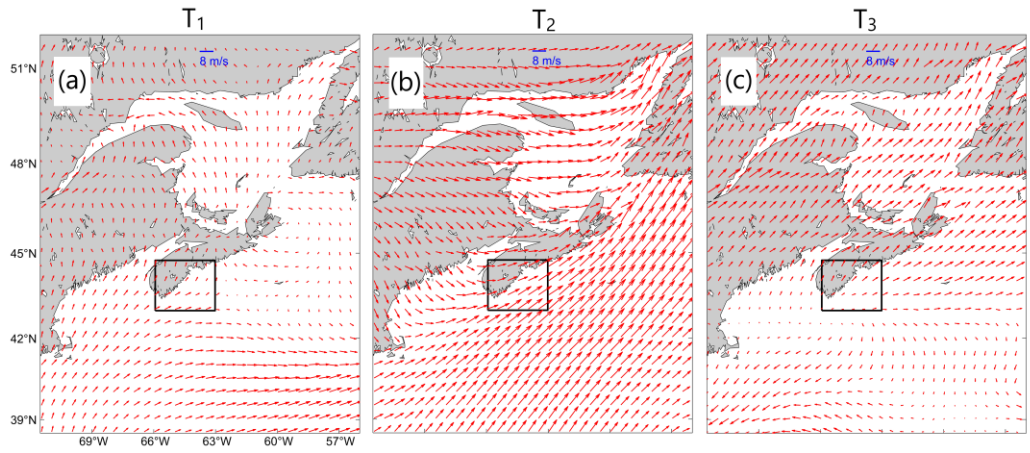

Figure 3.10. Horizontal distributions of surface wind velocities over the L2 domain at specific times before (T_1), during (T_2), and after (T_3) the strong wind event in early July 2018.

At time T_1 (15:00 UTC on 5 July) before the wind event, the surface circulation features relatively weak and southwestward currents near the coast and a strong southward jet with a small-scale cyclonic gyre in the middle shelf waters over the eastern portion of the L3 domain and several small-scale recirculation gyres over the southwestern portion of the L3 domain (Figure 3.11a). The SST at time T_1 is relatively warm and about 21 ^{o}C in St. Margaret's Bay and adjacent coastal waters and over coastal waters around Yarmouth (Figure 3.11a). The SST is relatively cool and about 11 ^{o}C in the offshore waters to the south of Cape Sable Island and also relatively cool and about 14 ^{o}C in the deep waters with the cyclonic gyre close to the eastern open boundary, due mainly to strong upwelling over these areas. Over the rest of the L3 domain, the SST at T_1 is relatively cool and about 16 ^{o}C (Figure 3.11a). The SSS at time T_1 is relatively high and about 32.0 (psu) over two local SST cooling areas and relatively low and about 30.5 (psu) over the rest of the L3 domain.

At time T_2 (0:00 on 7 July) during the peak of the winds, surface currents over the L3 domain are strong and nearly uniform to flow roughly southeastward due mainly to the effect

of strong local wind forcing (Figure 3.10b). An intense southeastward coastal jet of about 0.8 m s^{-1} occurs over coastal waters between Yarmouth and Cape Sable Island due mainly to the combined effect of wind-induced alongshore jets and baroclinic tidal currents. There are strong eastward currents of about 1 m s^{-1} over coastal waters to the south of Cape Sable Island at this time due to strong tidal mixing. The SST at T_2 is relatively cool and about 8.0 ºC near the coast of the L3 domain due to the wind-induced coastal upwelling (Figure 3.11b). The SST at this time is also relatively cool and about 8 ºC over coastal waters off Cape Sable Island. Over the rest of the L3 domain, the SST is nearly uniform and about 14.0 ºC at T_2 (Figure 3.11b). The SSS at time T_2 has the horizontal distribution similar to the counterpart at time T_1 (Figure 3.11d,e).

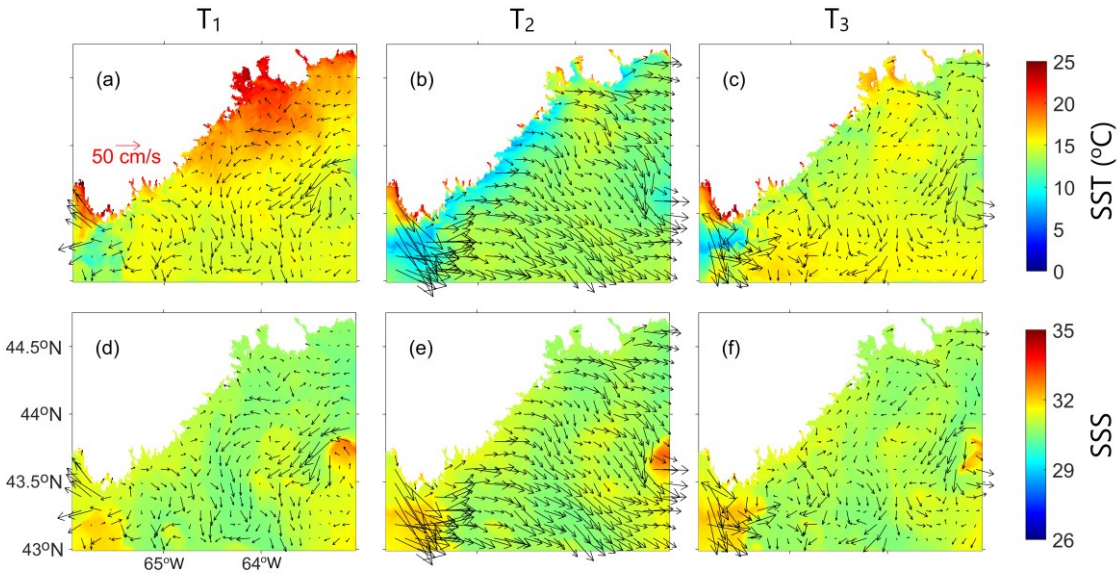

Figure 3.11. Distributions of instantaneous currents (vectors), temperature (image in upper panels) and salinity (image in lower panels) at the sea surface produced by submodel L3 in case CR over the L3 domain at times T_1 (15:00 UTC on 6 July), T_2 (0:00 on 7 July) and T_3 (15:00 on 8 July) in 2018. For clarity, velocity vectors are plotted at every 11th model grid point.

At time T_3 (15:00 on 8 July) after the winds die down, the surface currents and SSS over the L3 domain are very similar to the counterparts at time T_1. Except for coastal waters adjacent to St. Margaret's Bay and off Cape Sable Island, the SST at T_3 have horizontal features similar to the counterpart at T_1.

Figure 3.12 presents the instantaneous subsurface (40 m) currents and temperature over the L3 domain. The subsurface currents at time T_1 (before the wind event) are characterized by a narrow southwestward jet of about 20 cm s^{-1} with significant meander behaviours in the deep waters of the inner shelf and strong westward currents over coastal waters off Cape Sable Island (Figure 3.12a). There are northward inflows over areas close to the southern open boundary of the L3 domain at time T_1. The subsurface currents are relatively weak currents over the rest of the inner shelf at this time. The subsurface temperature at time T_1 is about 9 ºC over the L3 domain, with several narrow zones of relatively cool subsurface waters of about 4ºC (due mainly to the relatively intense throughflow from the Nova Scotia Current over the north section of the eastern open boundary and its meander behaviours and the associated small-scale gyres).

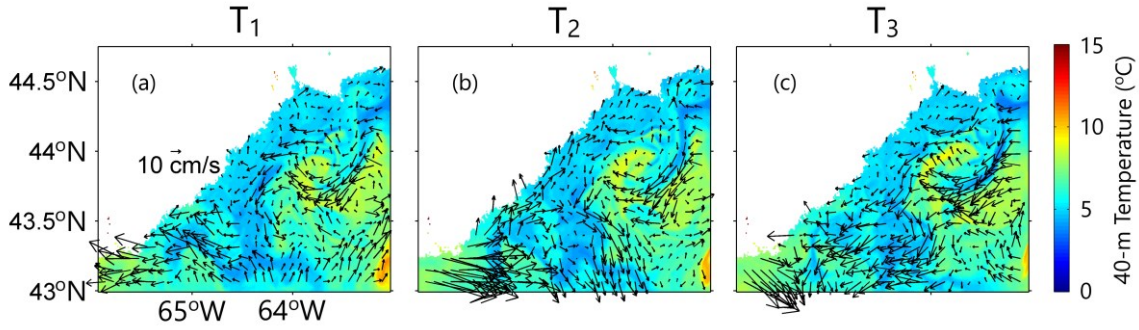

Figure 3.12. Distributions of instantaneous subsurface currents (vectors) and temperature (image) at 40 m produced by submodel L3 in case CR over the L3 domain at times T_1 (15:00 UTC on 6 July), T_2 (0:00 on 7 July) and T_3 (15:00 on 8 July) in 2018. For clarity, velocity vectors are plotted at every 11th model grid point.

At time T_2 (during the peak of the strong wind event), the subsurface (40 m) circulation features are characterized by intense eastward currents of about 0.7 m s^{-1} over coastal waters off Cape Sable Island, strong alongshore and northeastward currents of about 0.2 m s^{-1} following the coast, and strong and nearly southward currents of about 0.2 m s^{-1} over offshore areas adjacent to the middle section of the southern open boundary due to the effect of wind forcing (Figure 3.12b). A narrow southwestward jet of about 0.3 m s^{-1} occurs over the middle shelf close to the eastern open boundary at time T_2, which is very similar to the counterpart at T_1.

The subsurface currents at time T_3 (after the wind event) have circulation features similar to the counterparts at time T_1 over the inner shelf of the L3 domain, except for stronger magnitudes at T_3. At this time, there are strong southwestward currents over the middle shelf close to the eastern open boundary, and strong and southeastward subsurface currents over coastal waters off Cape Sable Island (Figure 3.12c). The subsurface temperature at time T_3 has the horizontal distribution very similar to the counterpart at time T_1.

3.3 Roles of Tides

The tidal forcing affects the 3D circulation and hydrography in two ways. Firstly, tides affect the advection terms in the momentum equations through tidal currents. Secondly, tides modify the temperature and salinity distributions through tidal currents and tidal mixing. The modifications of temperature and salinity distributions, in return, alter the density-driven currents. Several studies were made in examining the tidal impacts on the monthly mean large-scale circulation over the ECS (*Han et al*., 2010; *Wang et al.* 2020). Based on model results produced by NEMO-LIM, *Wang et al.* (2020) demonstrated that the tidal impacts are relatively small over the Labrador Shelf (LS) and Newfoundland Shelf (NFS), moderate over the Scotian Shelf (ScS), and particularly large over the central eastern GoM, the upper BoF,

and the northern flank of Georges Bank (GeB). In this section, the model results produced by the NGMS-seCS in cases CR (control run) and NT (no tide) are analyzed to examine the role of tidal forcing in the monthly mean circulation in the GSL, ScS and GoM, with a special emphasis on the 3D currents and hydrography over coastal and shelf waters of the southwestern ScS.

Figure 3.13a presents the surface M_2 tidal current ellipses in June 2018 over the L2 domain based on model results in case CR. The amplitude and phase of the surface M_2 tidal currents are calculated from the hourly time series of surface circulation in June 2018 using the Matlab program t_tide (*Pawlowicz et al.*, 2002). The surface M_2 tidal ellipses in this month show considerable spatial variability over the L2 domain, with the strongest M_2 surface currents over 1 m/s in the BoF, due mainly to the resonant characteristics of M_2 tidal currents over the area (*Ohashi et al.*, 2009b). Large M_2 surface currents also occur over the southwestern ScS and the southern flank of the GeB, with the major axes of tidal ellipses normal to the local isobathic contours. Over the BoF, southern flank of the GeB, and coastal waters off southwest Nova Scotia, the surface M_2 tidal ellipses produced by the NGMS-seCS are highly comparable with the baroclinic tidal ellipses from *Wang et al.* (2020) (Figure 3.13b, baroclinic tidal ellipses are plotted in red), including the magnitudes of M_2 surface currents and directions of the major axes of surface M_2 tidal ellipses. Figure 3.13a also shows relatively strong M_2 surface currents over outer-shelf waters of the ScS, which generally agree with the results of *Ohashi et al.* (2009b) and *Wang et al.* (2020). The M_2 surface currents decrease gradually from the southern flank of the southeastern GeB to the deep ocean water off the southwestern ScS, which consist with the results of *Katavouta et al.* (2016) and *Wang et al.* (2020). The surface M_2 tidal currents are very weak over the rest of the deep ocean waters (beyond the 1000 m isobathic contours) in the L2 domain. Over the Northumberland Strait, the surface M_2 tidal ellipses produced by submodel L2 are highly comparable with the

results of *Ohashi et al.* (2009b), including the magnitudes and directions of the strong rectilinear M_2 surface currents over the area.

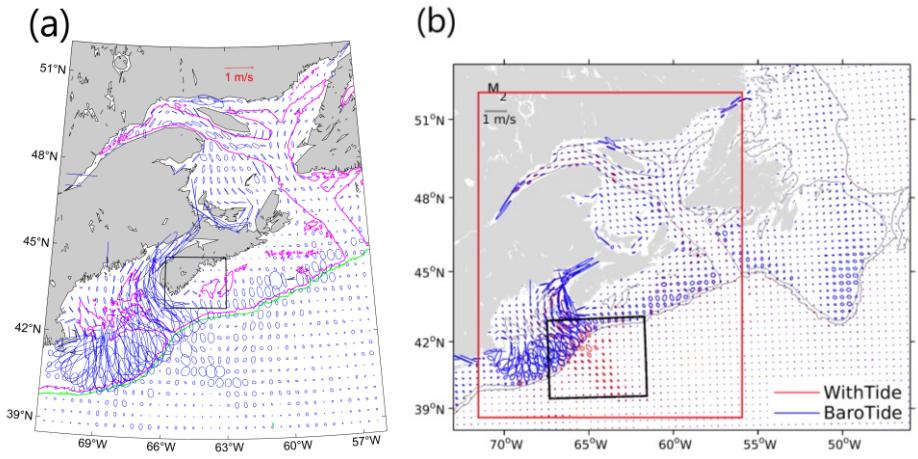

Figure 3.13. Surface M_2 tidal current ellipses calculated from the model results in June 2018 in case CR (*left panel*) and Figure A2 from *Wang et al.* (2020) (*right panel*). For clarity, Figure 3.13a presents M_2 tidal ellipses at every 14th grid point of the L2 domain. The M_2 tidal ellipses in (outside) the black box of Figure 3.13a are based on model results produced by submodel L3 (submodel L2). The red box of Figure 3.13b indicates the L2 domain of the NGMS-seCS.

Figure 3.14 presents the differences in the monthly-mean currents, temperature, and salinity at the sea surface ($\Delta\vec{\bar{U}}_0^{CR-NT}$, $\Delta\bar{T}_0^{CR-NT}$, $\Delta\bar{S}_0^{CR-NT}$) and 40 m ($\Delta\vec{\bar{U}}_{40}^{CR-NT}$, $\Delta\bar{T}_{40}^{CR-NT}$, $\Delta\bar{S}_{40}^{CR-NT}$) produced by submodel L2 between cases CR and NT in August 2018. Large values of $\Delta\vec{\bar{U}}_0^{CR-NT}$ occur in the deep waters off the shelf break of the ScS and GoM, due to modulations in the Gulf Stream, eddies and meanders by tides (Figure 3.14a). Large values of $\Delta\vec{\bar{U}}_0^{CR-NT}$ also occur in the BoF, northern GOM, Georges Bank and adjacent waters, southwestern ScS, western GSL, and Cabot Strait, which are mainly the density-driven currents associated with tide-induced modulations in the local density gradients. The general

features of $\Delta\vec{\overline{U}}_0^{CR-NT}$ shown in Figure 3.14a generally agree with multi-year averaged August-mean circulation differences shown in Figure 9d of *Wang et al.* (2020).

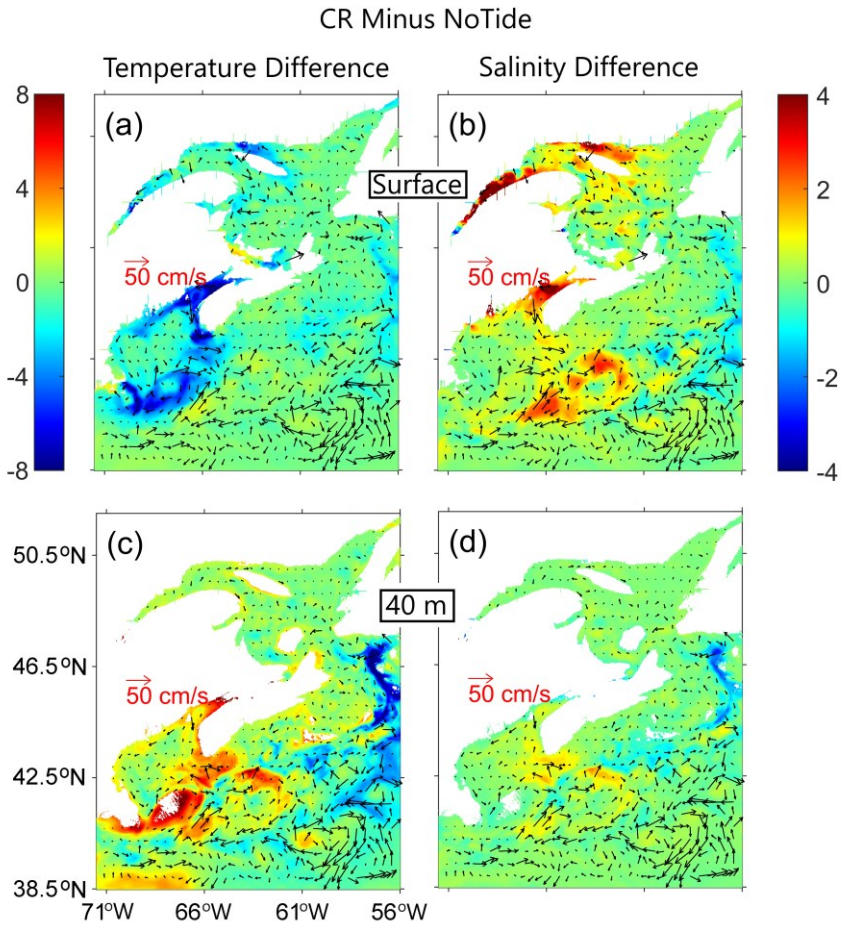

Figure 3.14. Differences in monthly-mean currents (black arrows), temperature (image in the left panels), and salinity (image in the right panels) in August 2018 between cases CR and NT at the surface (upper panels) and 40 m (lower panels) based on results produced by submodel L2 over the L2 domain. For clarity, velocity vectors are plotted at every 12th model grid point.

The tidal forcing also generates the August-mean SST cooling over the BoF, coastal waters of the northern GoM, GeB and adjacent waters, and southwestern ScS, with large and

negative values of $\Delta\bar{T}_0^{CR-NT}$ up to -7 °C (Figure 3.14a). Some noticeable SST cooling induced by tides occurs in the northern GSL and outer shelf waters of the eastern ScS and adjacent waters, due mainly to tidal mixing. In summer months, the large and positive net heat flux at the sea surface significantly warms up the surface water and causes the strong temperature vertical stratification over the L2 domain. Strong vertical mixing induced by tides is the main reason for large SST cooling shown in Figure 3.14a, with some contributions from the horizontal transport of different water masses by tide-induced mean currents.

The tide-induced vertical mixing is also responsible for large and positive values of $\Delta\bar{S}_0^{CR-NT}$ over the coastal and shelf waters of the L2 domain, with the maximum value of about 3.5 (Figure 3.14b). In the deep North Atlantic waters off the ScS and GoM, there are small-scale patches of positive and negative values of $\Delta\bar{S}_0^{CR-NT}$ due to tide-induced modulations in the Gulf Stream, eddies and meanders, as mentioned above.

The tide-induced changes in currents at 40 m over the L2 domain (Figure 3.14c) have similar circulation features as those at the sea surface, except for relatively smaller magnitudes at 40 m. Relatively large and positive values of $\Delta\bar{T}_{40}^{CR-NT}$ occur in the BoF, coastal waters of the GoM, Georges Bank and adjacent waters, and southwestern ScS, due mainly to strong vertical mixing induced by tides. By comparison, the tide-induced modulations in eddies and meanders are mainly responsible for large and positive values of $\Delta\bar{T}_{40}^{CR-NT}$ in the deep ocean waters off the GoM and southwestern ScS, and large and also negative values of $\Delta\bar{T}_{40}^{CR-NT}$ over the southeastern portion of Laurentian Channel and deep ocean waters off the ScS (Figure 3.14c).

The tide-induced changes in the subsurface August-mean salinity at 40 m ($\Delta\bar{S}_{40}^{CR-NT}$) are relatively small in the GSL and northeastern ScS and relatively large and positive over the southwestern ScS. The latter is generated by the tide-induced horizontal transport. In the

deep ocean waters off the southwestern ScS and GoM, there are small-scale patches of positive $\Delta\bar{S}_{40}^{CR-NT}$ due mainly to the tide-induced modulations in fronts, eddies and meanders.

To further demonstrate the role of tidal forcing in the vertical stratification, we examine the vertical distributions of August-mean temperature and salinity produced by submodel L2 in cases CR and NT along a north-south transect off Yarmouth marked as EE' in Figure 3.1b. As shown in Figure 3.15a, the August-mean temperature in case CR is vertically uniform over the northern section of transect EE' (within 40 km from the coast), and weakly stratified in the vertical over the southern section of the transect (beyond 40 km from the coast). The August-mean temperature in case NT without tidal forcing is highly stratified in the top 20 m and nearly uniform below 40 m along transect EE' (Figure 3.15b). There are also significant differences in the August-mean salinity along transect EE' between cases CR and NT. The above comparisons and discussions demonstrate clearly the important role of tidal mixing in the vertical distributions of temperature and salinity along transect EE'.

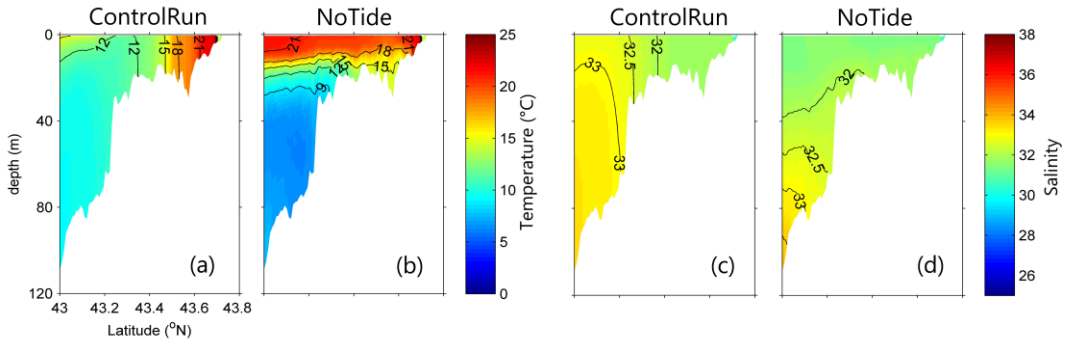

Figure 3.15. Vertical distributions of monthly-mean (a,b) temperature and (c,d) salinity in August 2018 along transect EE' off Yarmouth based on results produced submodel L2 in (a,c) case CR and (b,d) case NT.

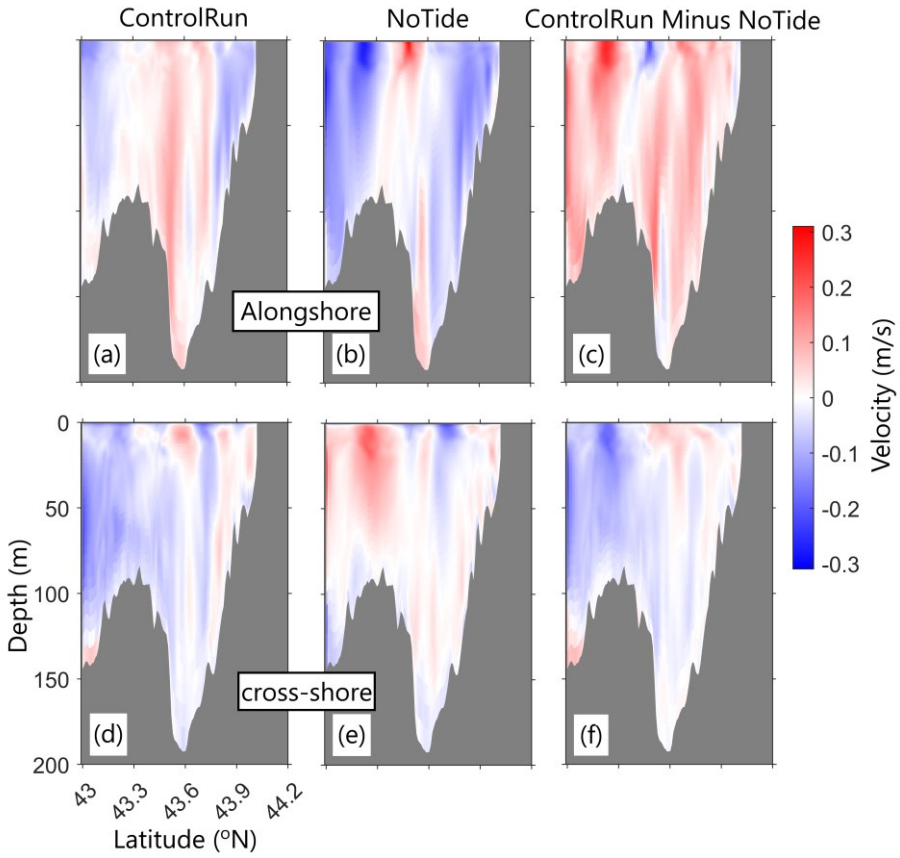

Figure 3.16. Vertical distributions of (a,b) alongshore components and (d,e) onshore components of monthly-mean horizontal currents in August 2018 along transect PP' based on results produced by submodel L3 in (a,d) case CR and (b,e) case NT. Vertical distributions of differences in August-mean (c) alongshore and (f) onshore components between cases CR and NT.

We next examine the alongshore and onshore components of monthly-mean horizontal currents in August 2018 at transect PP' off Liverpool Bay based on results produced by submodel L3 in cases CR and NT. In case CR, the alongshore components are negative (southwestward) and about 0.1 m s^{-1} over the inner section, positive (northeastward) and about 0.1 m s^{-1} over the middle section, and relatively weak (about 0.06 m s^{-1}) and

negative over the outer section of transect PP' (Figure 3.16a). The alongshore components also have significant horizontal and vertical variability at the transect. The onshore components in case CR are mainly onshore over the inner section and offshore over the outer section of the transect (Figure 3.16d).

In comparison with model results in case CR, the alongshore components at transect PP' in case NT (without tidal forcing) have relatively larger negative (southwestward) currents over the inner and outer sections and weaker positive (northeastward) currents over the middle section of transect PP' (Figure 3.16b). The onshore components in case NT are relatively weak over the inner section and relatively strong and positive (onshore) over the outer section of transect PP' (Figure 3.16e).

Figure 3.16c,f represents the tide-induced differences in the alongshore and onshore components ($\Delta\overline{U}_{PP'}^{CR-NT}$, $\Delta\overline{V}_{PP'}^{CR-NT}$) of August-mean horizontal currents in 2018 at transect PP' between cases CR and NT. The values of $\Delta\overline{U}_{PP'}^{CR-NT}$ are mainly positive (northeastward) and large up to 0.25 m s^{-1} at transect PP', except for negative values over a small middle section in the top 30 m (Figure 3.16c). The values of $\Delta\overline{V}_{PP'}^{CR-NT}$ are mainly negative (offshore) over the outer section and relatively small and highly variable over the inner section of the transect (Figure 3.16f). The large differences in the August-mean currents represent the important effect of tidal forcing for horizontal currents at transect PP'.

The vertical stratification of hydrography along transect PP' is also affected by the tidal forcing. Figure 3.17 shows the distributions of monthly-mean temperature and salinity in August 2018 based on model results in cases CR and NT. In comparison with the model results along transect PP' in case NT (Figure 3.17b), the August-mean temperature in CR (Figure 3.17a) is more uniform in the surface mixed layer and the thermohalines are broader than in NT, due mainly to the tide-induced vertical mixing in case CR. In the subsurface layer between 40 m and 80 m over the inner section of transect PP', the August-mean temperature

is vertically more uniform in case CR than the counterparts in case NT. Similarly, the August-mean salinity in the surface mixed layer along transect PP' is more uniform in case CR (Figure 3.17c) than in case NT (Figure 3.17d) due mainly to tidal mixing. In the subsurface between 40 m and 80 m over the outer section of transect PP', the vertical distribution of August-mean salinity in case CR also differs from the counterpart in case NT due to the effect of tidal forcing.

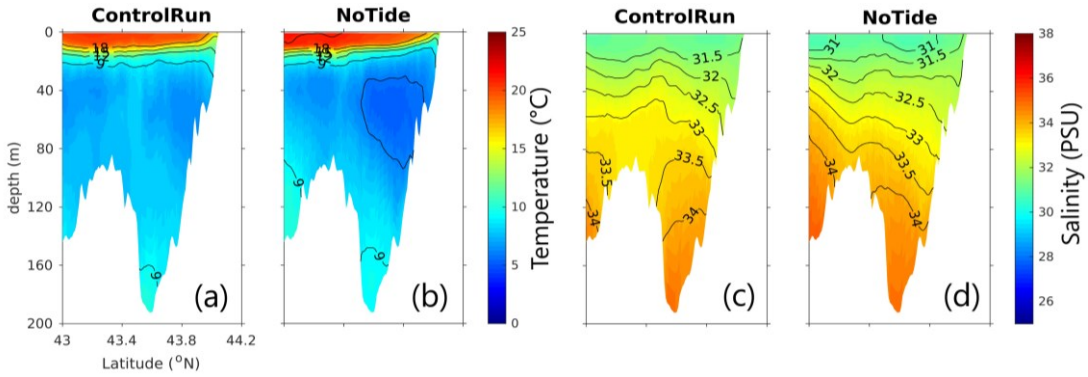

Figure 3.17. Vertical distributions of monthly-mean (a,b) temperature and (c,d) salinity in August 2018 along transect PP' off Liverpool Bay based on results produced submodel L3 in (a,c) case CR and (b,d) case NT.

3.4 Summary and Conclusion

Model results in four numerical experiments (cases ControlRun, NoWind, NoL3Wind and NoTide) were analyzed to investigate the effects of local winds, remote winds, and tides on three-dimensional (3D) circulation and hydrography over coastal waters of the southwestern Scotian Shelf (swScS). The newly developed nested-grid modelling system for the southeastern Canadian Shelf (NGMS-seCS) was used in the four experiments. The NGMS-seCS in case ControlRun (CR) is driven by all external forcing and model results in this case are the realistic simulation of 3D circulation and hydrography over the study region.

Differences in model results between case CR and other three cases (NoWind, NoL3Wind and Notide) are used to quantify the roles of local winds, non-local winds and tides on the study region.

The analysis of model results in the four cases demonstrated that local winds significantly reduced SST and slightly increased SSS over coastal waters of the ScS in summer months through wind-induced vertical mixing. Local winds also induced coastal upwelling over the swScS in August 2018, resulting in a narrow strip of relatively cold surface waters near the coast of the swScS. In August 2018, local wind forcing also significantly affected the monthly-mean circulation features in the surface mixed layer through wind-driven currents and modulated density-driven currents caused by wind-induced modulation of temperature and salinity. The August-mean temperature, salinity, and circulation at 40 m from cases CR and NoL3Wind were generally comparable, indicating the minor role of local wind forcing in hydrodynamics below 40 m in summer months (while the surface mixed layer is about 10-15 m in this month). In comparison with wind intensity in winter over the ScS, local winds are relatively weak during the summer and thus play minor roles in subsurface hydrodynamics below 40 m in summer months.

The August-mean SST results from NW and NoL3Wind were highly similar, with noticeable differences adjacent to the open boundaries. This indicated the secondary role of remote wind forcing in August-mean SST over the swScS, in comparison with the local wind effects. The August-mean surface and subsurface circulation in case NW differed significantly from the counterparts in cases NoL3Wind and CR, indicating the important effect of remote wind forcing in monthly-mean horizontal currents and meso-scale circulation features.

The August-mean model results from cases CR and NT were compared to investigate the tidal effects over the ScS. In general, tidal forcing affects circulation and hydrography through tidal currents and tidal mixing. The tide-induced modulation in hydrography affects the baroclinic hydrodynamics, density-driven currents, and horizontal advections. Over the

L2 and L3 domains, tide-induced modulation in local density gradients led to large density-driven currents over the Bay of Fundy, northern Gulf of Maine, Georges Banks and adjacent waters, and swScS. Over these areas, strong tidal mixing significantly weakened the vertical stratification. In particular, strong tidal mixing reduced SST and increased SSS significantly over these areas in August 2018. Over coastal waters of the swSsS, tidal forcing induced modulations of monthly-mean horizontal currents and weakens the vertical stratification.

CHAPTER 4

INVESTIGATIONS ON VARIABILITY OF DISSOLVED OXYGEN CONCENTRATION OVER COASTAL WATERS OF THE SCOTIAN SHELF USING A SIMPLE OXYGEN MODEL

A simple oxygen model coupled to submodel L3 of the NGMS-seCS is used to investigate the variability of dissolved oxygen concentration (DO) over coastal waters of the ScS. The model-simulated DO is validated against the reanalysis data and in-situ observations to assess the performance of the oxygen model. A sensitivity study is conducted to investigate the effects of net water respiration (NWR) and sediment oxygen consumption (SOC) over coastal waters of the southwestern ScS. The numerical experiments ControlRun, NoL3Wind, and NoTide introduced in Chapter 3 are implemented using the coupled circulation-oxygen model (L3COM) to examine the effects of local winds and tides on DO over coastal waters off southwest Nova Scotia.

4.1 Oxygen Model Setup

Both the physical (e.g., local winds and tides) and biological (e.g., respirations of marine organisms and sediment oxygen consumptions) processes play important roles in affecting the dissolved oxygen concentration (DO) over coastal waters of the ScS. A simple numerical oxygen model (developed by Yi Sui, a doctoral student under supervision of Prof. Jinyu Sheng, based on the simple oxygen model from *Yu et al.*, (2015)) coupled to submodel L3 of the NGMS-seCS (introduced and validated in Chapter 2) is used here to investigate the effects of tides, local winds (L3Wind), net water respiration (NWR), and sediment oxygen

consumption (SOC) on DO over coastal waters of the ScS, with a specific focus on Liverpool Bay and adjacent waters (Figure 3.1b).

The governing equation for the DO in the cartesian coordinates for simplicity is given as

$$\frac{\partial O_2}{\partial t} = -\left(\mathrm{u}\frac{\partial O_2}{\partial x} + v\frac{\partial O_2}{\partial y} + w\frac{\partial O_2}{\partial z}\right) + \frac{\partial}{\partial x}\left(K_h\frac{\partial O_2}{\partial x}\right) + \frac{\partial}{\partial y}\left(K_h\frac{\partial O_2}{\partial y}\right) + \frac{\partial}{\partial z}\left(K_v\frac{\partial O_2}{\partial z}\right) + NWR \quad (4.1)$$

where O_2 represents the DO, (u, v, w) respectively represent the eastward, northward, and upward components of ocean currents, and K_h and K_v are respectively the horizontal eddy diffusivity and vertical eddy viscosity coefficients.

The model setup of submodels L1, L2, and L3 have been discussed previously in Chapter 3. The horizontal and vertical coordinates of the simple oxygen model are respectively the same as the counterparts of submodel L3. Furthermore, the simple oxygen model uses the same parameterizations of horizontal and vertical turbulent mixing as the temperature and salinity in submodel L3. The simple oxygen model and submodel L3 are coupled for every time step (90 seconds). In the other words, the temperature, salinity, ocean currents and turbulent mixing produced by submodel L3 are applied to Equation 4.1 to calculate the instantaneous 3D field of DO over the L3 domain for every 90 seconds.

The boundary conditions (Neumann boundary conditions) for the DO at the sea surface and sea bottom are given as (*Yu et al.*, 2015)

$$K_v\frac{\partial O_2}{\partial z} = 6\cdot 2^{T/10}\cdot\left(1 - exp\left(-\frac{O_2}{30}\right)\right), \text{ at } z = -h(x,y) \quad (4.2)$$

$$K_v\frac{\partial O_2}{\partial z} = \frac{Vk_{O2}}{\Delta z}(O_{2sat} - O_2), \quad \text{at } z = \eta \quad (4.3)$$

where Vk_{O2} is a gas transfer velocity (in unit of cm hr^{-1}) with the parameterization

$$Vk_{O2} = 0.31 \cdot {u_{10}}^2 \cdot (\frac{660}{Sc_{ox}})^{\frac{1}{2}} \quad (4.4)$$

The boundary conditions for the DO at the sea surface and the sea bottom in Eqs. (4.2) and (4.3) represent respectively the air-sea oxygen flux (mmol O_2 m^{-2} d^{-1}) and sediment oxygen consumption (SOC) rate at the sea bottom (mmol O_2 m^{-2} d^{-1}). In Eq. (4.2), T indicates the water temperature in Celsius (°C), $h(x,y)$ represents the local water depth, and $z = -h(x,y)$ represents the vertical Cartesian coordinates of the sea bottom. In Eq. (4.3), $\eta(x,y)$ represents sea surface elevations, $z = \eta$ indicates the vertical Cartesian coordinates of the sea surface, Δz is the thickness of the respective grid space in the vertical direction (as a number, no unit), and O_{2sat} represents the solubility of dissolved oxygen (i.e., the saturated DO, in mmol m^{-3}) at the sea surface, which is a function of temperature and salinity (more details about O_{2sat} can be found in *Fennel et al.*, (2013) and *Yu et al.*, (2015)). In Eq. (4.4), u_{10} represents the wind speed at 10 m above the sea surface (in unit of m s^{-1}), and Sc_{ox} is the Schmidt number for oxygen (*Wanninkhof*, 1992).

The parameterization for the NWR includes two terms: primary production (PP) and respiration (R),

$$NWR = R + PP \quad (4.5)$$

where R is negative-semidefinite (always non-positive) and PP is positive-semidefinite (always non-negative).

The primary production rate describes how fast the organic carbon and dissolved oxygen are produced through biological processes (e.g., photosynthesis) in the ocean. The

respiration rate represents how fast the organic carbon and dissolved oxygen are consumed through biological processes (e.g., decomposition of organic matters) in the ocean.

The observational study made by *Packard and Christensen* (2004) demonstrated that the respiration rate (R) is linearly dependent on the chlorophyll concentration (Chl) over the southwestern ScS:

$$R = a(Chl) + b \tag{4.6}$$

where *a* and *b* are coefficients for the linear dependence. Table 4.1 lists the values of *a* and *b* estimated from observations made at two stations (42 and 48) over the southwestern ScS and three stations (10, 12, 14) in the western GoM (taken from *Packard and Christensen*, 2004). Stations 42 (65° 49.9'W, 42° 57.4'N) and 48 (65° 50.5' W, 42° 57.6'N) are located very close to Point A (in Figure 3.1a) in the southwestern ScS, and Stations 10 (69° 31.1'W, 42° 35.7'N), 12 (69° 31.8'W, 42° 35.2'N), and 14 (69° 31.4'W, 42° 34.8'N) are located very close to Point B (in Figure 3.1a) in the western GoM. In this study, the average values of *a* and *b* estimated from observations at stations 42 and 48 (over the southwestern ScS) are used for the respiration rate in the L3COM, based on

$$\bar{a} = \frac{n_{42}a_{42}+n_{48}a_{48}}{n_{42}+n_{48}} \qquad \bar{b} = \frac{n_{42}b_{42}+n_{48}b_{48}}{n_{42}+n_{48}} \tag{4.6}$$

where *n* represents the number of measurement pairs of Chl and R, and the subscript represents the index of the observation station.

The 3D fields of chlorophyll concentration and primary production rate used in the parameterization for the NWR in the L3COM were extracted from the daily Global Ocean Biogeochemistry Hindcast dataset known as the GLOBAL_REANALYSIS_BIO_001_029 (hereafter GRB29) with a horizontal resolution of 1/4° provided by CMEMS. This dataset

contains several biogeochemical variables including the DO, chlorophyll concentration, primary production, and phytoplankton concentration produced by the Pelagic Interactions Scheme for Carbon and Ecosystem Studies (PISCES) biogeochemical model on the NEMO modelling platform. More details about the model setup and biogeochemical variables of the GRB29 dataset can be found at the website of resources.marine.copernicus.eu/product-detail/GLOBAL_MULTIYEAR_BGC_001_029/. The initial conditions and open boundary conditions for the DO in L3COM were taken from the GRB29 reanalysis dataset.

Table 4.1. Linear relationships between Chl (mg L^{-1}) and R (pmol O_2 min^{-1} L^{-1}) based on *Packard and Christensen* (2004) in the form of $R = a(Chl) + b$. In the table, r^2 represents the square of cross-correlation, n represents the number of measured Chl and R, Δz represents the range of depths considered. Stations 42 and 48 are located in the southwestern ScS (at Point A of Figure 3.1a). Stations 10, 12 and 14 are located in the western GoM (at Point B of Figure 3.1a).

Station	n	Δz	a	b	r^2
10	11	5-75	0.1158	-0.0088	0.721
12	11	1-265	0.1242	0.0246	0.385
14	11	2-230	0.0977	0.0628	0.390
42	12	1-130	0.0616	0.0101	0.945
48	10	1-145	0.0408	-0.0149	0.933

4.2 Performance of the Oxygen Model

The performance of the coupled circulation-oxygen model (L3COM) in simulating 3D currents and hydrography was discussed in Chapter 3. In this section, we focus mainly

on the performance of the coupled modelling system in simulating the DO over the L3 domain by comparing model results with the GRB29 dataset.

The monthly-mean SST in March 2018 produced by L3COM is between 2 ºC and 4 ºC over the inner shelf and about 5 ºC in the offshore deep waters close to the eastern and southern open boundaries (Figure 4.1a). The simulated sea surface dissolved oxygen concentration (SSDO) is relatively high and about 360 mmol m^{-3} over the northeastern portion of the L3 domain and relatively low and about 320 mmol m^{-3} over offshore waters adjacent to the eastern and southern open boundaries (Figure 4.1b). A broad and intense (about 0.3 m s^{-1}) coastal jet in this month enters the L3 domain through the northern part of the eastern open boundary and transports cold surface waters about 2 ºC with high SSDO of about 360-370 mmol m^{-3} southwestward (Figure 4.1a). Before reaching coastal waters to the south of St. Margaret's Bay, this coastal jet splits into two branches: an inshore branch and offshore branch. The inshore branch flows southwestward along the coast, which results in relatively cold SST and relatively high SSDO over inshore waters of the L3 domain, due mainly to horizontal advection, turbulent mixing, and intense air-sea oxygen fluxes caused by low SST. The offshore branch veers cyclonically to flow nearly southward and mixes relatively cool coastal waters with the relatively warm (about 5 ºC) offshore waters with relatively low SSDO (about 320 mmol m^{-3}), resulting in the southwardly extended low SST and high SSDO features over the middle shelf adjacent to the central part of the southern open boundary of the L3 domain.

It should be noted that the SST and SSDO have opposite spatial variability over the L3 domain in March 2018 (Figure 4.1a,b). This can be explained by the fact that the SST affects significantly the SSDO through the air-sea oxygen fluxes. As suggested by *Fennel et al.* (2013) and *Yu et al.* (2015), the solubility of dissolved oxygen (O_{2sat}) increases as the temperature decreases. As a result of the Neumann boundary condition for the DO (Equation

4.3) at the sea surface (i.e., air-sea oxygen flux), cold surface waters dissolve more oxygen than warm surface waters.

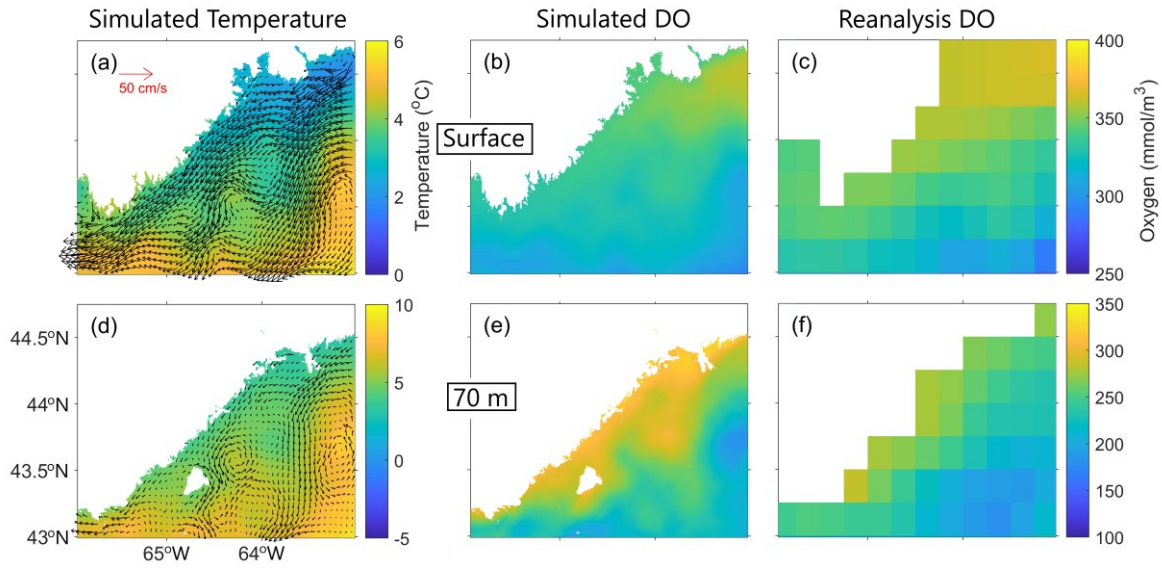

Figure 4.1. Monthly-mean temperature (image in a,d), currents (arrows in a,d), and DO (b,e) produced by L3COM at (a,b) the surface and (d,e) 70 m over the L3 domain in March 2018. For clarity, velocity vectors are plotted at every 6th model grid point. Figure 4.3c,f presents the March-mean DO in 2018 at the sea surface and 70 m over the L3 domain calculated from the daily-mean product of the GRB29 dataset.

The subsurface temperature at 70 m in March 2018 (Figure 4.1d) produced by L3COM is relatively cold and about 4 ºC over the inner shelf and relatively warm and between 7 ºC and 8 ºC in the offshore deep waters close to the eastern and southern open boundaries. The simulated March-mean subsurface DO at 70 m (Figure 4.1e) is relatively high and about 310 mmol m^{-3} over the inner shelf and relatively low and between 200 mmol m^{-3} and 220 mmol m^{-3} in the offshore waters adjacent to the southern and eastern open boundaries (Figure 4.1e). Very similar to the surface circulation shown in Figure 4.1a except for smaller amplitudes, the March-mean subsurface circulation at 70 m in 2018 produced by the L3COM features a

relatively intense and broad alongshore current (roughly southwestward with speeds between 0.1 m s^{-1} and 0.15 m s^{-1}) over the inner shelf close to the northern portion of the eastern open boundary of the L3 domain. This southwestward current also splits into a southwestward inner-shelf branch and a nearly southward offshore branch at 70 m. The inner-shelf branch transports the relatively cold (about 4 ºC) subsurface waters with relatively high DO (about 310 mmol m^{-3}) southwestward. The offshore branch results in a southwardly extended water mass with relatively cold temperature and relatively high DO at 70 m over the middle shelf. The March-mean subsurface currents at 70 m produced by L3COM (Figure 4.1d) also feature several small-scale cyclonic (anticyclonic) gyres with magnitudes of about 0.1 m s^{-1}. These gyres result in upwelling (downwelling) and small-scale patches of warm (cool) temperature and low (high) DO at the subsurface in March 2018. This demonstrates the important role of eddy-induced upwelling/downwelling on the small-scale features of hydrography and DO at 70 m over the L3 domain in the winter months.

Figure 4.1c,f shows the March-mean GRB29 reanalysis of DO in 2018 at the surface and 70 m respectively over the L3 domain. It should be noted that the horizontal resolution of the GRB29 dataset is 1/4° (about 19 km by 28 km over the L3 domain), which is very coarse in comparison with the horizontal resolution of 1/108° (about 0.7 km by 1.0 km) for L3COM. Nevertheless, a comparison between the simulated (Figures 4.1b,e) and reanalysis DO (Figure 4.1c,f) demonstrates that the March-mean DO at the sea surface and 70 m produced by L3COM has the large-scale spatial distribution highly similar to the GRB29 reanalysis over the L3 domain. Both the GRB29 reanalysis and L3COM results have the relatively high DO over the inner shelf and the relatively low DO over offshore waters adjacent to the eastern and southern open boundaries. In comparison with the reanalysis DO, the simulated March-mean DO in 2018 by L3COM is slightly lower at the sea surface and slightly higher at 70 m over the inner shelf. One plausible reason is differences in the vertical

mixing between the NEMO modelling platform used in generating GRB29 reanalysis and L3COM due to different atmospheric forcing and numerical schemes for vertical mixing in the two models. Furthermore, L3COM has a higher horizontal resolution (1/108º) and a better topography than the reanalysis data. As a result, the L3COM can use smaller horizontal diffusivities and resolves more spatial variability and small-scale features of hydrography and circulation (which significantly affect the small-scale features of DO) than the reanalysis data of DO.

Figure 4.2a presents the monthly-mean currents and temperature at the sea surface in August 2018 produced by L3COM. As discussed previously in Chapters 2 and 3, the main features of the August-mean SST in 2018 produced by L3COM show a narrow strip of relatively cool surface waters of about 16 ºC near the coast associated with wind-induced coastal upwelling, and relatively cool water mass of 13 ºC over coastal and deep waters off Yarmouth due mainly to strong tidal mixing. Over other areas of the L3 domain, the SST is relatively warm and about 20 ºC (Figure 4.2a).

The August-mean surface circulation in 2018 produced by L3COM is characterized by a relatively weak and northeastward currents over the inner shelf to the east of Western Head, relatively strong southwestward currents over the inner shelf to the west of Western Head, and strong westward currents over coastal waters off Cape Sable Island. There are several gyres at the sea surface in the middle shelf close to the eastern and southern open boundaries of the L3 domain in August 2018 (Figure 4.2a). In comparison with the March-mean circulation (Figure 4.1a), the August-mean surface currents (Figure 4.2a) in 2018 are significantly weaker, due to the fact that the surface wind stress and wind-induced vertical mixing are weaker in August than in March.

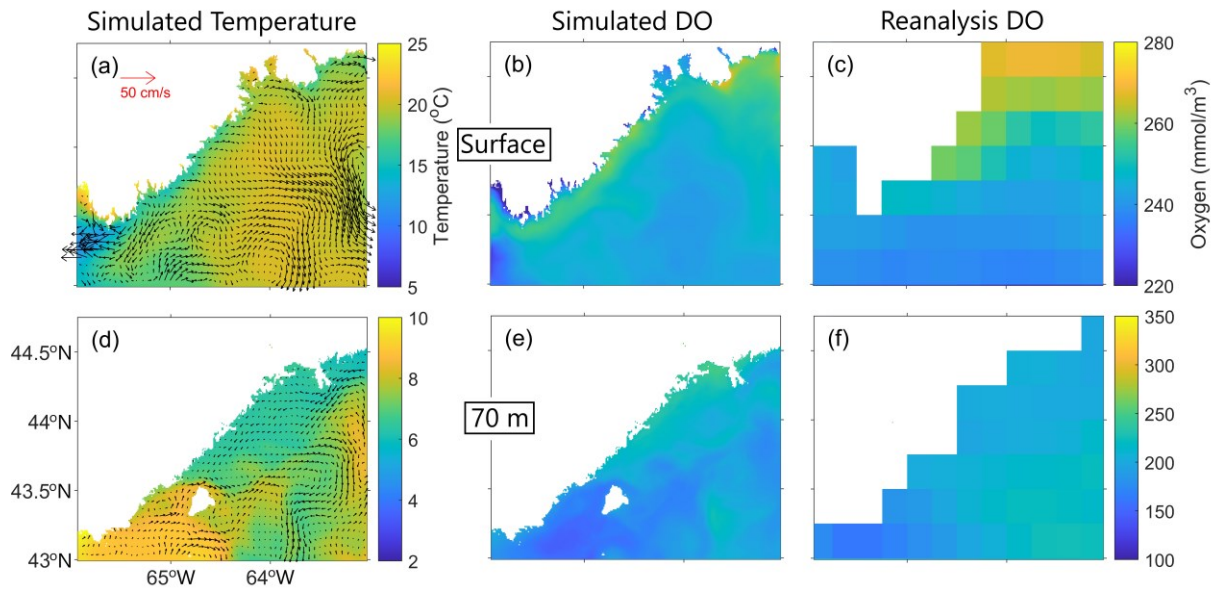

Figure 4.2. The monthly-mean L3COM results (left and middle panels) and reanalysis data (right panels) at the sea surface (upper panels) and 70 m (lower panels) over the L3 domain in August 2018. Otherwise as in Figure 4.2.

The August-mean subsurface temperature at 70 m in 2018 produced by L3COM (Figure 4.2d) is relatively warm and ~9 °C over the southwestern portion of the L3 domain due to the strong tide-induced mixing and advection. The August-mean subsurface circulation at 70 m produced by L3COM features a relatively intense (about 6 cm s^{-1}) alongshore (southwestward) jet in the inner shelf close to the northern part of the eastern open boundary. This alongshore coastal jet splits into two branches, with one branch flowing southwestward along the coast and the other branch meandering southward. These two branches transport relatively cold subsurface waters from the northern part of the eastern open boundary to the inner shelf and offshore waters over the southeastern portion of the L3 domain. Because of relatively weak vertical mixing and strong stratification in August 2018, the horizontal distributions of subsurface temperature and currents at 70 m in August (Figure 4.2d) differ significantly from the counterparts at the sea surface (Figure 4.2a) over the L3 domain.

A comparison between the August-mean simulated DO (Figure 4.2b,e) and GRB29 reanalysis (Figure 4.2c,f) in 2018 demonstrates that the surface and subsurface DO fields produced by L3COM are generally comparable with the reanalysis. In particular, both the L3COM results and the GRB29 reanalysis have the relatively high SSDO (between 260 mmol m^{-3} and 270 mmol m^{-3}) over the inner shelf and relatively low (about 245 mmol m^{-3}) SSDO over the offshore water of the L3 domain. The relatively high SSDO over the inner shelf is due mainly to the combined effect of the air-sea oxygen flux and wind-induced upwelling (the latter was discussed in Chapter 3). The major differences between the simulated and reanalysis DO are due mainly to different horizontal resolutions and model topography used in L3COM and NEMO, which result in significantly different hydrodynamics, such as different circulation and hydrographic features and different values of horizontal eddy viscosity and diffusivity coefficients used in the two models.

Figure 4.2b demonstrates that the relatively high SSDO occurs in the narrow zone with low SST near the coast associated with the wind-induced coastal upwelling in August 2018, due partially to the increased air-sea oxygen flux since the solubility of dissolved oxygen (O_{2sat}) increases as the temperature decreases. Furthermore, the maximum values of DO in the vertical (to be discussed in the process study and sensitivity study section of this chapter) occur at the subsurface (normally between 20 m to 40 m) in August 2018 (Figure 4.2b). As a result, the wind-induced coastal upwelling of the subsurface water with relatively higher DO also contributes to the relatively high SSDO near the coast in August 2018. It should be noted that the surface water adjacent to the western open boundary of the L3 domain has both relatively low SST (about 13 ^{o}C) and low SSDO (about 230 mmol m^{-3}) due mainly to tidally-induced strong vertical mixing and advection over the area.

The DO is significantly affected by the solubility of dissolved oxygen, air-sea oxygen flux, mixing and advection in the upper-water column over the southwestern ScS, as well as

other ocean waters. As discussed in Chapter 2, the NGMS-seCS has a satisfactory skill in reproducing the hydrographic distribution, mixing, and advection over the ScS. The parameterizations for the air-sea oxygen flux, dissolved oxygen solubility and the SOC used in this study were used in many other studies (*Fennel et al*., 2013; *Yu et al.* 2015; *Hetland and DiMarco*; 2008*; Fennel et al*., 2013; *Yu et al.*, 2015).

To demonstrate the performance of L3COM in simulating the vertical structure of DO, the model results are compared with the in-situ observations of DO made at three points (B, C and D) over the southwestern ScS in July 2018 by the Department of Fisheries and Oceans (DFO) Canada (the data request form is available on http://isdm.gc.ca/isdm-gdsi/request-commande/form-eng.asp?s=1). Point B (63.9 °W, 43.7 °N), Point C (63.7 °W, 43.6 °N), and Point D (63.5 °W, 43.9 °N) are marked in Figure 3.1b. The observed DO data at Points B, C, and D were made at 02:27 on 15 July; 08:17 on 15 July; and 16:45 on 14 July respectively in 2018. The in-situ observations of DO at these three points are chosen due to the availability of in-situ observations and the period of interest for this study.

The observed DO in the surface mixed layer (top 10 m) was between 290 mmol m^{-3} and 300 mmol m^{-3} at points B and D and about 275 mmol m^{-3} at point C (Figure 4.3) in July 2018. Below the surface mixed layer, the observed DO increased with depths and reached the maximum values at depths of about 30 m. The maximum values of DO were about 340 mmol m^{-3} at points B, C, and D. From the depths of DO maxima to about 80 m, the observed DO gradually decreased with depths. Below 80 m, the observed DO slowly decreased with depths and reached the minima of about 130 mmol m^{-3} at points B and about 140 mmol m^{-3} at points C and D at the sea bottom.

A comparison between the simulated and observed DO at these three points (Figure 4.3) indicates that L3COM has reasonable skills in reproducing the general vertical structures

of observed DO over the southwestern ScS. The simulated daily-mean DO in the surface mixed layer (top 10 m) are vertically uniform and about 275 mmol m^{-3} at Point D on July 14 (Figure 4.3c) and weakly stratified and about 270 mmol m^{-3} at Points B and C on July 15 (Figure 4.3a,b) in 2018, due mainly to the wind-induced vertical mixing. Below the surface mixed layer, the simulated daily-mean DO increases with depths and reaches the maximum values at depths of about 30 m. The DO maxima produced by L3COM are about 340 mol m^{-3}, which agree reasonably well with the observations (Figure 4.3). Below the depths of DO maxima, the simulated DO gradually decreases with depths and reaches the minima at the sea bottom. The DO minima produced by L3COM are about 140 mmol m^{-3} at Points B and D and about 150 mmol m^{-3} at Points C, which are also in a good agreement with the observations.

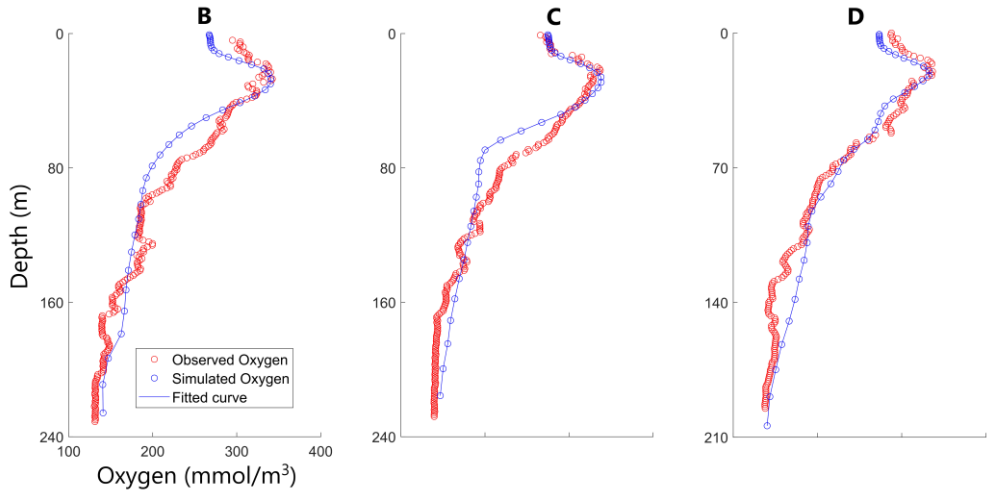

Figure 4.3. Vertical profiles of observed (red dots) and simulated (blue lines) DO at Points B, C, and D over the southwestern Scotian Shelf in July 2018. The blue line in each subplot represents the daily-mean DO by averaging model results at four grid points around each observation point.

Figure 4.3 also demonstrates that L3COM has noticeable deficiencies in reproducing the observed DO between 50 m and 90 m at Points B and C and observed small-scale vertical variations at the three points. One of plausible reasons is the large error in the parameterization for the NWR. The chlorophyll and primary production data from the GRB29 dataset are based on numerical model results without data assimilation and thus can differ significantly from their true values. In addition, the accuracies of the lateral open boundary condition of DO and atmospheric forcing also affect the performance of L3COM. Furthermore, the accuracy of simulated DO can be affected by the model errors in simulated hydrographic distribution and ocean circulation (i.e., the locations of subsurface small-scale eddies which induce upwelling/downwelling and cannot be simulated realistically by any circulation model without data assimilation).

4.3 Sensitivity Study

As mentioned earlier in this chapter, DO over coastal waters of the ScS and other coastal and shelf waters are affected by biogeochemical processes including photosynthesis, respiration, and benthic biological processes. These sophisticated biogeochemical processes are parameterized by numerical schemes (Eqs. 4.2 and 4.5) in L3COM. The parameterized NWR in L3COM represents the combined effect of all local biogeochemical processes which consume or produce dissolved oxygen in the ocean. The parameterized SOC in L3COM represents the combined effect of all benthic biogeochemical processes affecting dissolved oxygen at the sea bottom.

To examine the effects of NWR and SOC on DO over the L3 domain, model results in three numerical experiments with different parameterized biogeochemical processes (Table 4.2) are considered in this section. The first numerical experiment is the Control Run (CR), which includes the NWR, SOC, and all other external forcing presented in Chapter 2.

The second numerical experiment (case NoNWR) is the same as ControlRun except for excluding the NWR. The third numerical experiment (case NoSOC) is the same as ControlRun except for excluding the SOC. These three numerical experiments are integrated from January 1 to November 30 in 2018. Model results in July 2018 in cases NoNWR and NoSOC are compared with the counterparts in case CR to examine the effects of NWR and SOC in the summer of 2018.

Table 4.2. List of three numerical experiments CR, NoNWR, and NoSOC using L3COM with different parameterized biogeochemical processes.

Numerical Experiment	NWR	SOC	All external forcing for driving the coupled circulation-ice modelling system (described in Chapter 2)
ControlRun (CR)	Yes	Yes	Yes
NoNWR	No	Yes	Yes
NoSOC	Yes	No	Yes

4.3.1 Role of Net Water Respiration

We first examine the simulated DO produced by L3COM in cases CR (ControlRun) and NONWR along transect PP' over the southwestern ScS (marked in Figure 3.1b) to demonstrate the role of the net water respiration (NWR) over the southwestern ScS. Figure 4.4 presents vertical distributions of July-mean DO in 2018 along transect PP' in the two

cases. The July-mean DO along transect PP' in case CR has different features in four layers in the vertical. These four vertical layers consist of a thin surface layer (in the top ~10 m) with nearly vertically uniform DO (about 270 mmol m^{-3}), an upper intermediate layer (roughly between 10 m and 40 m) with relatively high DO (between 300 to 340 mmol m^{-3}), a lower intermediate layer (roughly between 40 m to 70 m) with rapid decreases of DO with depths, and a bottom layer (below ~70 m) with gradual decrease of DO with depths. The July-mean DO in case CR has relatively small horizontal gradient in the surface layer, due to the combined role of air-sea oxygen flux at the sea surface and wind-induced mixing and advection in the surface mixed layer. The sub-surface maxima of DO at about 30 m are partially caused by the seasonal variation in temperature stratification from winter to summer, with some contributions from the horizontal advection of outside dissolved oxygen through the open boundaries of the L3 domain. The relatively low DO near the bottom is due mainly to the weak vertical mixing in deep layers, with some contributions from the SOC.

From winter to summer, the SST over the L3 domain increases from -1 ºC to 21 ºC due mainly to the positive net heat flux at the sea surface. The temperature in the upper intermediate layer (between 10 m and 40 m) also rises from winter to summer, but not as much as the temperature increase in the surface mixed layer (less than 10 m). As mentioned earlier, the solubility of dissolved oxygen decreases as the water temperature increases. Because the increase of temperature from winter to summer is much larger in the surface mixed layer than in the upper intermediate layer, the surface mixed layer loses significantly more dissolved oxygen than the upper intermediate layer during the period. Therefore, the vertical gradients of DO over the interface between the surface mixed layer and the upper intermediate layer are very large, and the DO maxima in the vertical occur in the upper intermediate layer in summer months as shown in Figure 4.4a. As a result of relatively weak wind-induced vertical mixing and relatively strong vertical stratification over coastal waters of the ScS in summer months, the subsurface water with the highest DO are trapped in the upper intermediate layer.

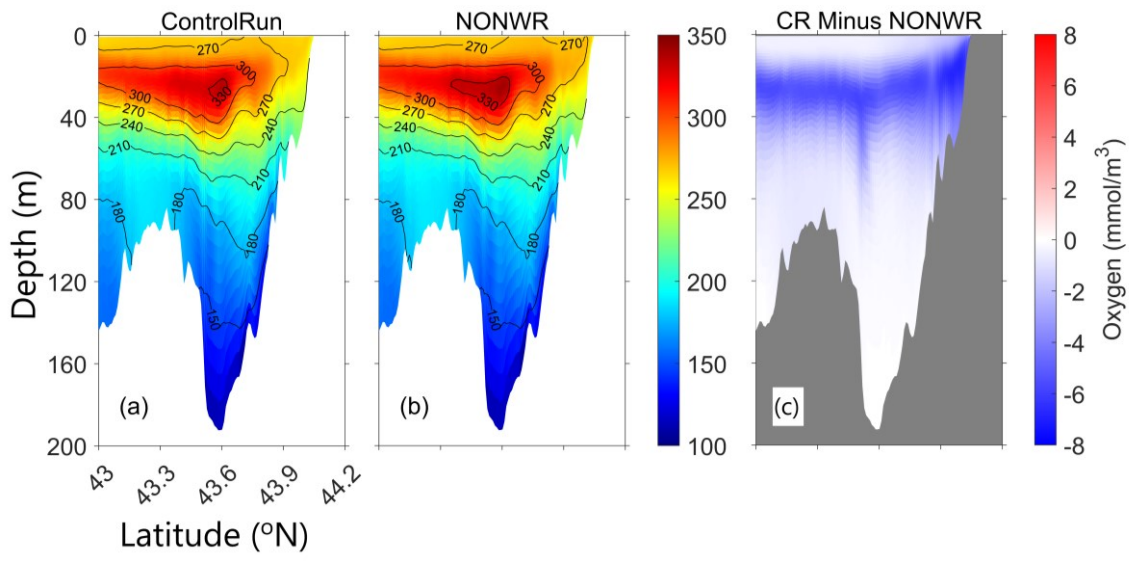

Figure 4.4. Vertical distributions of July-mean DO in 2018 produced by L3COM in cases (a) CR and (b) NoNWR along transect PP' over the southwestern Scotian Shelf. (c) Differences in July-mean DO in 2018 between cases CR and NoNWR along transect PP'.

The vertical distribution of July-mean DO along transect PP' in 2018 in case NoNWR (Figure 4.4b) is highly comparable with the counterpart in case CR (Figure 4.4a). This indicates that the hydrodynamics including turbulent mixing, advection, and air-sea oxygen flux play very important roles on the vertical stratification and distribution of DO over the southwestern ScS. By comparison, the NWR only plays a minor role in the simulated DO in case CR.

The differences in July-mean DO ($\Delta\bar{O}_{PP'}^{CR-NoNWR}$) along transect PP' between cases CR and NoNWR shown in Figure 4.4c can be used to represent the effect of the NWR on DO in case CR. The values of $\Delta\bar{O}_{PP'}^{CR-NoNWR}$ are negative and relatively large in the subsurface between 20 m and 40 m and over coastal waters along transect PP' in July 2018, due mainly to the effects of biomass and chlorophyll distributions. The NWR reduces the July-mean DO in the subsurface and coastal waters along transect PP' by up to 8 mmol m^{-3} in 2018. The maximum negative values of $\Delta\bar{O}_{PP'}^{CR-NoNWR}$ in July 2018 occur at depths of about 30 m, which

are generally consistent with the depths of the highest chlorophyll concentration in the vertical over the southwestern ScS during the summer (*Ross et al.*, 2017; *Laurent et al.*, 2021).

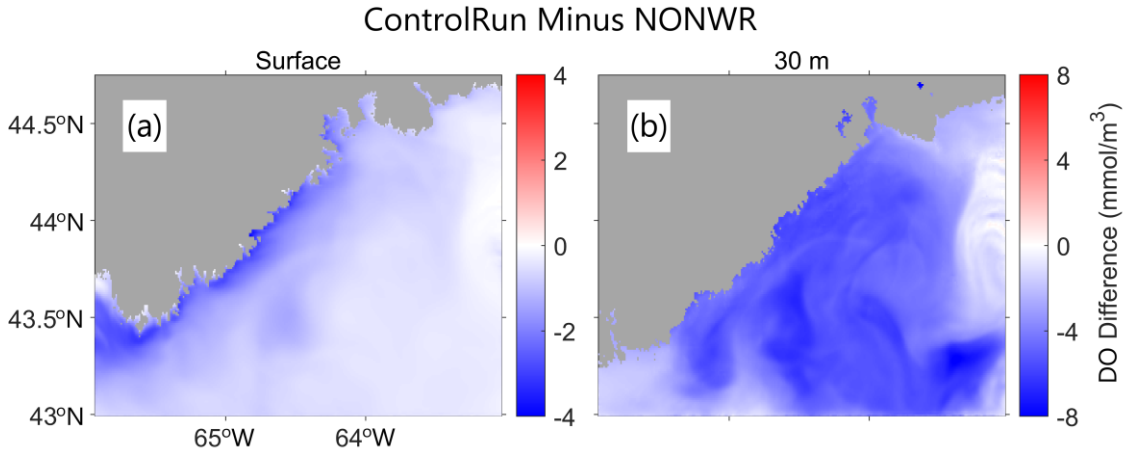

Figure 4.5. Horizontal distributions of the differences in July-mean DO between cases CR and NoNWR over the L3 domain at (a) the sea surface and (b) 30 m.

Figure 4.5a presents the differences in July-mean DO in 2018 at the sea surface between case CR and case NoNWR ($\Delta\bar{O}_0^{CR-NoNWR}$) produced by L3COM over the L3 domain. The values of $\Delta O_0^{CR-NoNWR}$ are relatively small in the offshore deep waters, and negative over the inner shelf, with the maximum negative values of about -4 mmol m^{-3} over coastal waters off Cape Sable Island. By comparison, the differences in July-mean DO at 30 m (Figure 4.5b) between case CR and case NoNWR ($\Delta\bar{O}_{30}^{CR-NoNWR}$) are negative and significantly larger than the counterparts at the sea surface, particularly over the central region of the L3 domain, with the maximum negative values of about -8 mmol m^{-3} over middle shelf waters (64.5 °W, 43.5 °N) to the south of Liverpool Bay. It should be noted that the horizontal advection of outside dissolved oxygen into the L3 domain through the open boundaries results in relatively small differences in July-mean DO near the open boundaries

of the L3 domain. In general, the chlorophyll concentration is relatively high over subsurface and inshore waters of the ScS in summer months. The observational data made by *Ross et al*. (2017) and *Laurent et al.* (2021) demonstrated the highest chlorophyll concentration at depths of about 30 m over the ScS during the summer. Over coastal waters with high chlorophyll concentration, high dissolved oxygen and carbohydrates (essential food nutrients for organisms) are produced by primary production, resulting in large amounts of biomass and high respiration rates over the areas. The relatively large respiration rates (parameterized by the 3D chlorophyll concentration data from the GRB29 dataset) and primary production rates (extracted from the GRB29 dataset) in L3COM result in a relatively large effect of the NWR in the DO at the subsurface between 20 m and 40 m and over coastal waters of the L3 domain.

4.3.2 Role of Sediment Oxygen Consumption

We next examine the role of the sediment oxygen consumption (SOC) in DO over the southwestern ScS. The July-mean DO in 2018 along transect PP' produced by L3COM in case NoSOC is shown in Figure 4.6b. The vertical distribution of July-mean DO in case CR shown in Figure 4.6a is the same as in Figure 4.5a. An examination of Figures 4.6a,b demonstrates that the simulated DO in case NoSOC is almost the same as the counterparts in case CR except for the bottom boundary layer due to the effect of the SOC in case CR. The differences in July-mean DO ($\Delta\bar{O}_{PP'}^{CR-NoSOC}$) between case CR and case NoSOC (Figure 4.6c) are significantly negative and up to -15 mmol m^{-3} at the sea bottom along transect PP', due mainly to the direct effect of the SOC. Outside the bottom boundary layers, the non-zero values of $\Delta\bar{O}_{PP'}^{CR-NoSOC}$ are associated with advection and mixing of low DO from the bottom boundary layers to other layers.

Figure 4.7a,b presents the differences in July-mean DO in 2018 between case CR and case NoSOC over the L3 domain respectively at the sea surface ($\Delta\bar{O}_{0}^{CR-NoSOC}$) and at 40 m ($\Delta\bar{O}_{40}^{CR-NoSOC}$). At the sea surface, $\Delta\bar{O}_{0}^{CR-NoSOC}$ are small over the L3 domain except for areas

near the coast. Over the shallow waters near the coast, the values of $\Delta\bar{O}_0^{CR-NoSOC}$ are negative, with the maximum negative values of about -15 mmol m^{-3}. This is expected since the SOC directly reduces DO in the bottom boundary layer. Advection and mixing are responsible for small negative values (about -5 mmol m^{-3}) of $\Delta\bar{O}_0^{CR-NoSOC}$ in the offshore waters off Cape Sable Island. At 40 m, $\Delta\bar{O}_{40}^{CR-NoSOC}$ are small over the L3 domain except for areas with water depths less than 50 m (Figure 4.7b). The maximum negative values of $\Delta\bar{O}_{40}^{CR-NoSOC}$ are about -13 mmol m^{-3} over the inner-shelf waters due to the shallow water depths. In addition, relatively large negative values of $\Delta\bar{O}_{40}^{CR-NoSOC}$ over offshore waters adjacent to the middle sections of the eastern and southern open boundaries are due mainly to upwelling associated with cyclonic eddies.

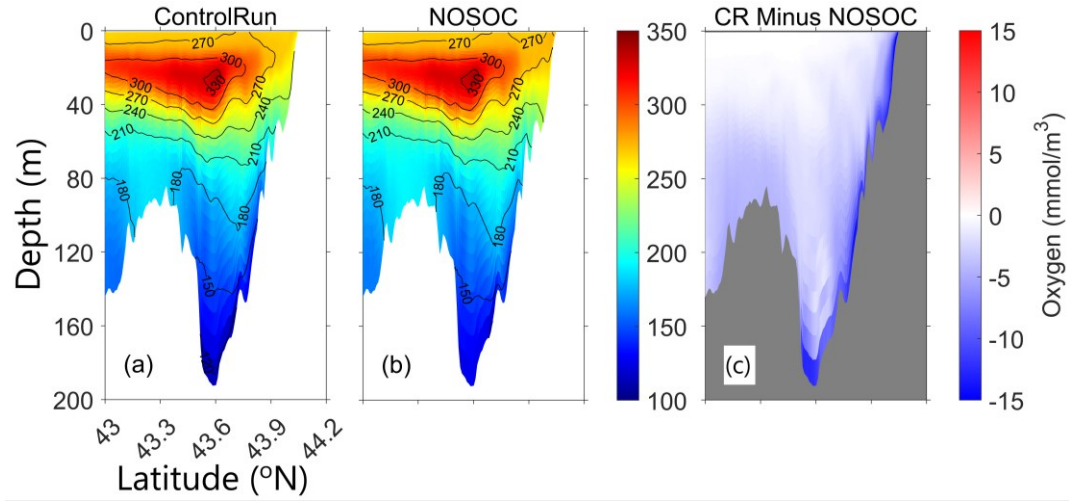

Figure 4.6. Vertical distributions of July-mean DO in 2018 produced by L3COM in cases (a) CR and (b) NoSOC along transect PP' over the southwestern Scotian Shelf. (c) The differences in July-mean DO in 2018 between cases CR and NoSOC along transect PP'.

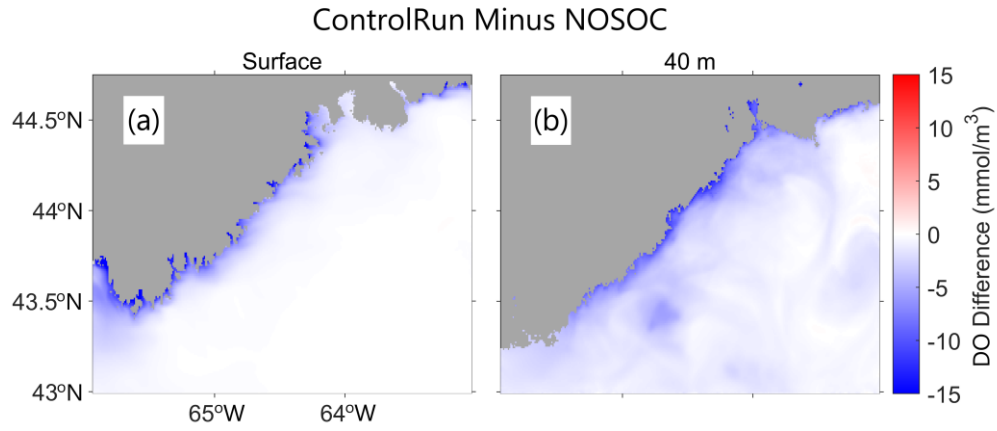

Figure 4.7. Horizontal distributions of the differences in July-mean DO between cases CR and NoSOC over the L3 domain at (a) the sea surface and (b) 40 m.

4.3.3 Effects of Local Winds

The distribution of DO over the southwestern ScS is affected significantly by wind forcing through its effects on air-sea oxygen flux, mixing, and advection. To examine the effects of local winds (i.e., L3Wind) on DO over the southwestern ScS, the numerical experiment NoL3Wind (Table 3.1) is conducted using L3COM with both the NWR and SOC included. In addition, the simulated DO fields in case CR (Table 4.2) at times T_1, T_2, and T_3 (shown in Figures 3.9 and 3.10) are analyzed to examine the DO responses to the strong wind event in early July 2018.

The August-mean surface currents in 2018 produced by L3COM in cases CR and NoL3Wind are shown respectively in Figure 4.8a,b. As discussed in Chapter 3, the August-mean surface currents in case CR are characterized by a weak northeastward coastal jet of about 5 cm s^{-1} at the coast, offshore currents in the deep waters of the inshore shelf of the western ScS, and several gyres over the middle shelf. Differing significantly from the model

results in case CR, the August-mean surface currents in case NoL3Wind have relatively strong southwestward coastal currents and a large-scale and intense anticyclonic gyre over the middle shelf.

The monthly-mean SSDO in August 2018 produced by L3COM in case CR is relatively high (about 270 mmol m^{-3}) near the coast, relatively low (about 230 mmol m^{-3}) to the south of Cape Sable Island, and about 250 mmol m^{-3} over the rest of the L3 domain (Figure 4.9a). The narrow strip of relatively high SSDO (about 270 mmol m^{-3}) near the coast shown in Figure 4.8a is associated with wind-induced coastal upwelling in August 2018. The water mass with relatively low SSDO (about 230 mmol m^{-3}) over the area close to the western open boundary of the L3 domain is due mainly to the strong tidal mixing and advection. In comparison, the August-mean SSDO in 2018 in case NoL3Wind (Figure 4.8b) is significantly higher than the counterparts in case CR over the interior of the L3 domain. Furthermore, model results in case NoL3Wind do not have a narrow strip of relatively high SSDO off southwest Nova Scotia due to the lack of wind-induced coastal upwelling in this case. The main reasons for the large differences in SSDO between cases CR and NoL3Wind in August 2018 are the role of local wind forcing in the air-sea oxygen flux and vertical mixing. It should be noted that the advection and mixing of outside dissolved oxygen through the open boundaries are responsible for highly comparable SSDO over the areas close to the open boundaries of the L3 domain in both cases CR and NoL3Wind (Figure 4.8a,b).

As shown in Eqs. (4.3) and (4.4), the air-sea oxygen flux depends on intensities of wind stress and solubilities of dissolved oxygen at the sea surface. From winter months to summer months, solubilities of dissolved oxygen (O_{2sat} in Eq. 4.3) at the sea surface over the L3 domain gradually decrease due to the seasonal SST warming. As a result, the dissolved oxygen in the upper-column water over the southwestern ScS is gradually released to the atmosphere through the air-sea flux in case CR from winter to summer. If local winds are

turned off, the air-sea oxygen flux is zero since $Vk_{O2} = 0$. As a result, no dissolved oxygen is released to the atmosphere in case NoL3Wind, even though dissolved oxygen in the upper-column water of the southwestern ScS is oversaturated. Furthermore, the vertical mixing over coastal waters of the southwestern ScS is unrealistically weak in case NoL3Wind in comparison with the counterparts in case CR. It should be noted that, although some water mass with high DO in the L3 domain moves out through the open boundaries in case NoL3Wind, a significantly large amount of water with unrealistically high DO still remains in the upper layer of the L3 domain in this case.

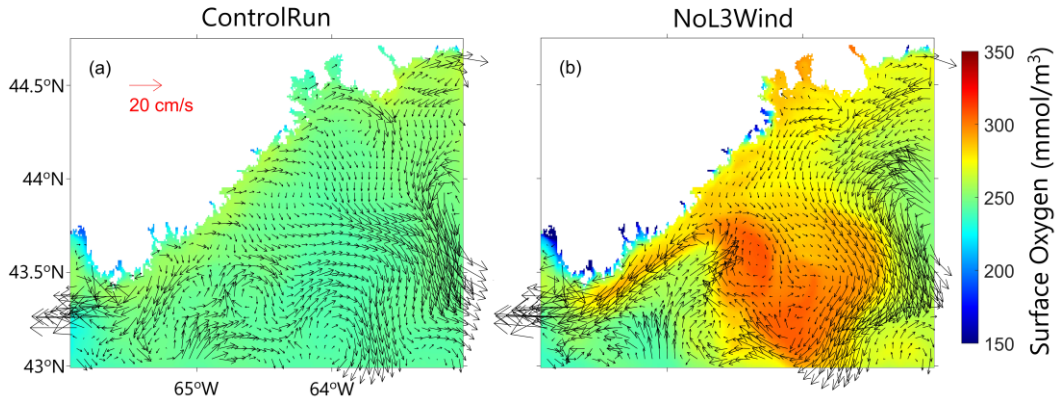

Figure 4.8. Monthly-mean surface currents (arrows) and SSDO (image) in August 2018 produced by L3COM in cases (a) CR and (b) NoL3Wind over the L3 domain. For clarity, velocity vectors are plotted at every 6th model grid point.

Figure 4.9 presents the August-mean DO in 2018 along transect PP' produced by L3COM in cases CR and No3Wind. Similar to the July-mean DO in 2018 shown in Figure 4.4a, the vertical distribution of August-mean DO in 2018 in case CR can also be divided into four layers along transect PP'. In the surface mixed layer (roughly the top ~10 m), the August-mean DO in case CR is nearly uniform (about 250 mmol m^{-3}) in both horizontal and vertical directions along transect PP', due mainly to the wind-induced vertical mixing in case

CR. In the upper-intermediate layer between 10 m and 40 m along transect PP', the August-mean DO in case CR is high and between 270 mmol m^{-3} and 310 mmol m^{-3}, with the maxima at ~20 m in this month. In the lower intermediate layer between 40 m and 70 m, the August-mean DO along transect PP' decreases significantly with depths from ~270 mmol m^{-3} to ~210 mmol m^{-3} within ~30 m. In the bottom layer below 70 m, the August-mean DO in case CR decreases gradually with depths and reaches the minima at the sea bottom (Figure 4.9a).

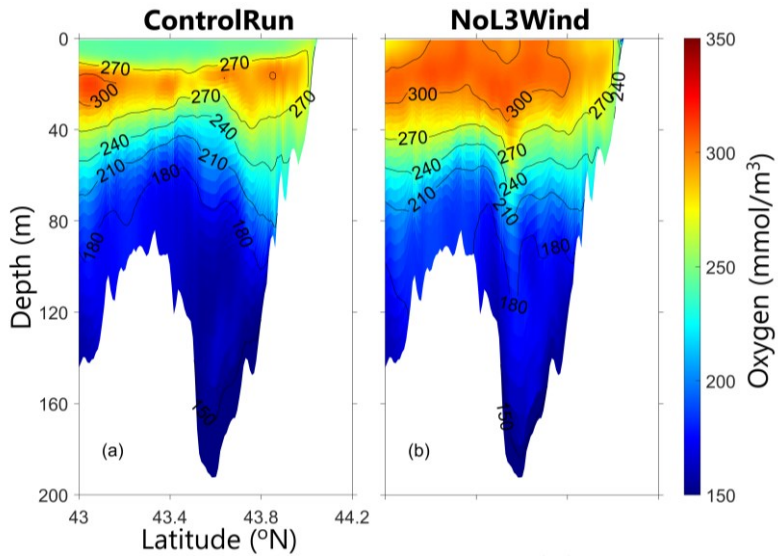

Figure 4.9. Vertical distributions of August-mean DO in 2018 produced by L3COM in cases (a) CR and (b) NoL3Wind along transect PP' over the southwestern Scotian Shelf.

In comparison with results in case CR (Figure 4.9a), the August-mean DO in case NoL3Wind is unrealistically high (between 290 mmol m^{-3} and 310 mmol m^{-3}) in the surface mixed layer (less than 10 m), particularly over the middle shelf water, due to the absence of the air-sea oxygen flux at the sea surface and lack of wind-induced vertical mixing in case

NoL3Wind. The August-mean DO below 40 m on transect PP' in case NoL3Wind, in general, is slightly higher than the counterparts in case CR. From winter to summer, the net heat flux gradually warms the upper-column water of the southwestern ScS and thus reduces the solubility of dissolved oxygen in the upper-column water of the L3 domain in both cases CR and NoL3Wind. In case NoL3Wind, the oversaturated dissolved oxygen in the upper-column water cannot be released to the atmosphere due to the absence of air-sea oxygen flux (Equations 4.3 and 4.4). As a result of vertical mixing and advection induced by the tidal forcing, some oversaturated dissolved oxygen in the upper-column water is transported to the deeper layers in case NoL3Wind (instead of released to the atmosphere in case CR).

4.3.4 Effects of Tides

The distribution of DO is also affected by the tidal forcing, particularly over areas with strong tidal currents and tidal mixing. Figure 4.10 demonstrates that the August-mean DO along transect PP' in case NT has general features of vertical distribution similar to the counterpart in case CR, except for the differences in the DO maxima in the upper-intermediate layer. The maximum values of August-mean DO in case NT are about 330 mmol m^{-3}, which are higher than the maximum values of about 300 mmol m^{-3} in case CR. This can be explained by the effect of tide-induced vertical mixing and tide-induced northeastward circulation over the southwestern ScS (Figure 3.16c). Significant differences also occur in the August-mean DO in the surface mixed layer and lower-intermediate layer between case CR and case NT, which further demonstrate the important role of tidal forcing on the vertical distribution of DO over the southwestern ScS.

To further demonstrate the effect of tidal forcing on circulation and DO over the southwestern ScS, we examine the August-mean DO in the subsurface at 20 m over the L3 domain in both cases CR (Figure 4.11a) and NT (Figure 4.11b). The August-mean subsurface (20 m) currents in cases CR and NT are similar over the inner shelf to the east of Cape Negro Island, and differ significantly due to strong tidal currents and tidal mixing over costal and

offshore waters off Cape Sable Island. The August-mean subsurface currents in these two cases also differ significantly over the middle shelf of the L3 domain (Figure 4.11). In particular, the August-mean subsurface currents in case NT feature a significantly broader westward current entering the L3 domain from the northern section of the eastern open boundary and a stronger westward jet over the southern section of the eastern open boundary than the counterparts in case CR.

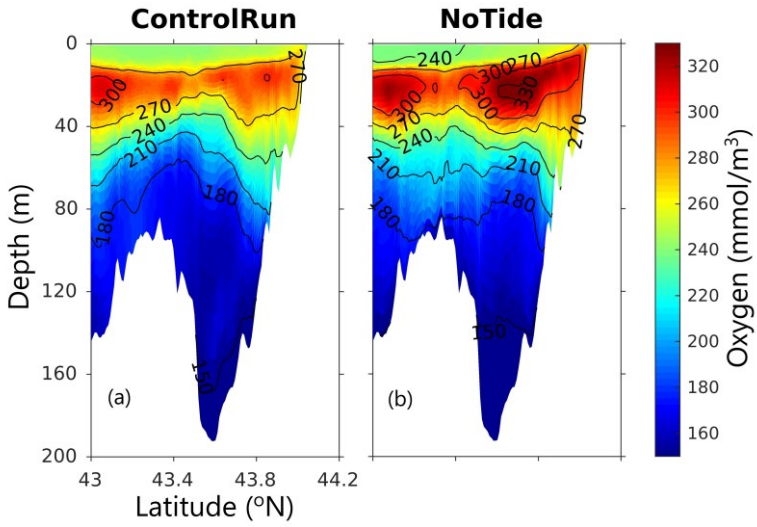

Figure 4.10. Vertical distributions of August-mean DO in 2018 produced by L3COM in cases (a) CR and (b) NT along transect PP' over the southwestern Scotian Shelf.

The August-mean subsurface (20 m) DO in 2018 produced by L3COM in case CR is between 200 mmol m^{-3} and 250 mmol m^{-3} over the southwestern portion and middle shelf close to the eastern open boundary and between 300 mmol m^{-3} and 330 mmol m^{-3} over the rest of the L3 domain (Figure 4.11a). In comparison with the counterpart in case CR, the August-mean subsurface DO in 2018 in case NT (Figure 4.11b) is more horizontally uniform, with the values about 340 mmol m^{-3} over the eastern part and between 290 mmol m^{-3} and 300 mmol m^{-3} over the southwestern part of the L3 domain. In both cases CR and NT, the August-mean subsurface (20 m) DO is relatively low near the coast due to the combined effect of the

SOC and coastal upwelling induced by the local wind forcing. Over the southern portion of the L3 domain, the simulated DO in case NT features two small-scale patches of relatively low DO due mainly to the effect of downwelling associated with anticyclonic eddies.

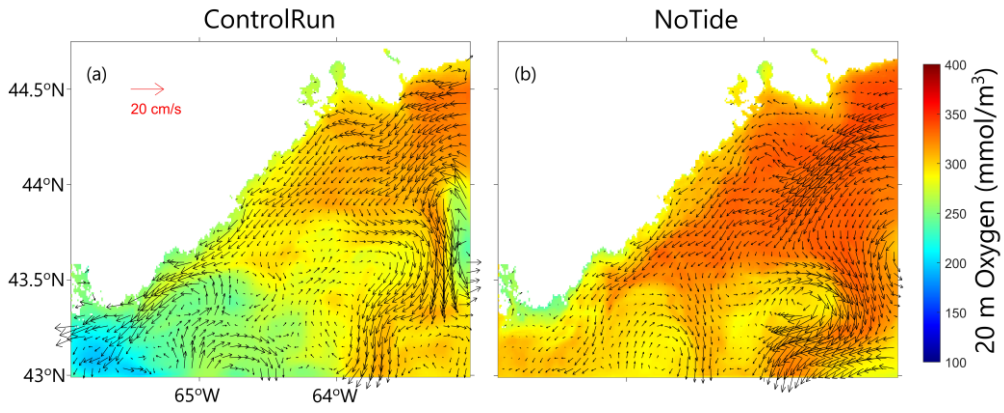

Figure 4.11. August-mean subsurface (20 m) currents (arrows) and DO (image) in 2018 produced by L3COM in cases (a) CR and (b) NT over the L3 domain. For clarity, velocity vectors are plotted at every 6th model grid point.

4.4 Distribution of Dissolved Oxygen Concentration during a Strong Wind Event

The above analyses (in section 4.3.3) demonstrated the important roles of local wind forcing on the August-mean DO over the L3 domain, even though local winds are relatively weaker in summer months than in winter months on average. The local wind forcing also significantly modifies the 3D field of DO over the southwestern ScS through air-sea oxygen flux and wind-induced mixing and advection at short timescales during strong wind events. As mentioned earlier in Chapter 3, strong northeastward winds occurred over the ScS, GoM, GSL and adjacent waters in early July 2018. As shown in Figure 3.9, the area-mean wind velocities over the areas with wet-points in the L3 domain were weak on 5 July, reached the

maxima (about 12 m s^{-1}) from 12:00 on 6 July to 0:00 on 7 July, and died down from 15:00 on 7 July. Instantaneous SSDO results produced by L3COM in case CR at times T_1 (before the event, 15:00 on 5 July), T_2 (during the peak of the event, 0:00 on 7 July), and T_3 (after the event, 15:00 on 8 July) are analyzed to examine the effects of the strong northeastward winds on SSDO over the L3 domain during the strong wind event.

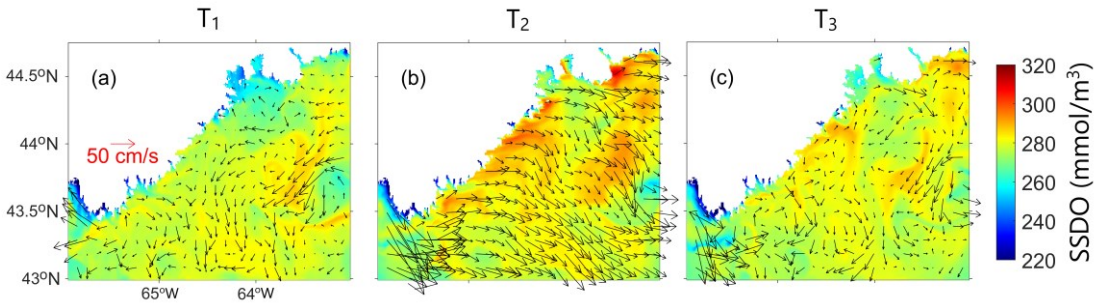

Figure 4.12. Distributions of instantaneous currents (arrows) and DO (image) at the sea surface produced by L3COM in case CR over the L3 domain at times (a) T_1 (15:00 UTC on 6 July), (b) T_2 (0:00 on 7 July) and (c) T_3 (15:00 on 8 July) in 2018. For clarity, velocity vectors are plotted at every 11^{th} model grid point.

Figure 4.12 presents the instantaneous SSDO produced by L3COM in case CR at times T_1, T_2, and T_3 (Figures 3.9 and 3.10). The general characteristics on the surface currents at these three times were discussed in Chapter 3. At time T_1 (15:00 UTC on 5 July) before the wind event, the simulated SSDO is relatively low and between 240 mmol m^{-3} and 260 mmol m^{-3} in St. Margaret's Bay and adjacent coastal waters and over coastal waters between Yarmouth and Cape Sable Island (Figure 4.12a), due mainly to the warm SST over these areas (Figure 3.11a). The SSDO is also relatively low and about 250 mmol m^{-3} in the middle shelf close to the eastern open boundary, due mainly to the upwelling associated with the cyclonic eddy. Over the rest of the L3 domain, the SSDO at T_1 is generally about 280 mmol m^{-3} (Figure 4.12a).

At time T_2 (0:00 on 7 July) during the peak of the wind event (Figure 4.12b), the simulated SSDO is relatively high and about 295 mmol m^{-3} near the coast of the L3 domain, as the combined effect of the high solubility of dissolved oxygen (O_{2sat}) at the sea surface (due to SST cooling), large air-sea oxygen flux (due to intense wind stress and high O_{2sat}), and wind-induced coastal upwelling (vertical transport of the subsurface water with high DO to the sea surface). During this event, the SST is slightly warmer in St. Margaret's Bay, Mahone Bay, and adjacent coastal waters than other areas near the coast (Figure 3.11b), resulting in weaker air-sea oxygen flux (from the atmosphere to the ocean) and relatively lower SSDO (about 275 mmol m^{-3}) over these local areas. At this time, intense eastward currents of about 1 m s^{-1} occur to the south of Cape Sable Island, which transport the outside water masses with significantly low SSDO (due to strong tidal mixing and advection) into the L3 domain through the western open boundary and result in the relatively low SSDO over the southwestern portion of the L3 domain. Over the rest of the L3 domain, the SSDO is about 285 mmol m^{-3}.

At time T_3 (15:00 on 8 July) after the winds die down, the SSDO over the L3 domain is very similar to the counterpart at time T_1. Except for the SSDO over coastal waters near the coast, the SSDO at time T_3 have horizontal features similar to the counterparts at time T_1.

4.5 Distribution of Dissolved Oxygen Concentration during a Coastal Upwelling Event

The above analyses demonstrated the important roles of wind-induced upwelling in affecting the SST and SSDO over inner-shelf waters off southwest Nova Scotia in summer months. To further examine the effects of wind-induced coastal upwelling on temperature and DO in Liverpool Bay and adjacent coastal waters, we analyze the variability of temperature and DO during a coastal upwelling event in October 2018.

In the middle of October 2018, persistent northeastward and southeastward strong winds recurrently occurred over Liverpool Bay and adjacent coastal waters and thus induced several coastal upwelling at Point A in Figure 3.1b. We will examine the hourly temperature and DO at point A produced by L3COM during this coastal upwelling event to demonstrate the role of wind-induced coastal upwelling in the 3D fields of temperature and DO in Liverpool Bay and adjacent coastal waters during this event.

Figure 4.13 presents the time series of wind velocities averaged over areas with wet-points over the L3 domain from 12 to 31 October 2018. Based on the Ekman transport theory and the results of Petrie et al. (1987), persistent strong northeastward winds over the ScS are upwelling favourable winds. As shown in Figure 4.13, persistent local winds (over the L3 domain) with relatively large northeastward components recurrently appeared and thus generated several coastal upwelling in Liverpool Bay and adjacent waters from 15 to 25 October 2018. In addition, intense strong southeastward winds generate intense nearly southward surface currents over middle shelf waters and relatively large seaward surface currents over Liverpool Bay, which also contribute to coastal upwelling in the bay and adjacent inner-shelf waters.

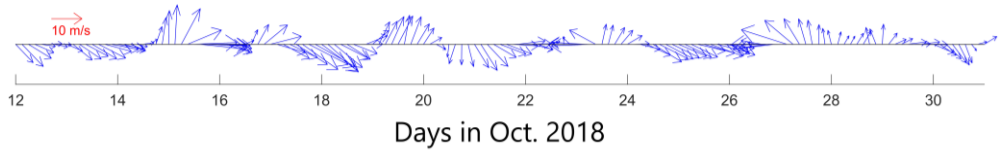

Figure 4.13. Time series of the area-mean wind velocity vectors averaged at all wet points over the L3 domain, from 12 to 31 October 2018.

Figure 4.14 presents the time series of observed (red) and simulated (blue) temperature at 5 m in Liverpool Bay (point A in Figure 3.1b) from October 12 to October 31, 2018. The observation data (collected by sensors in the fish cage) was provided by Prof. Jonathan Grant's research group at Dalhousie University. The observed temperature at point A gradually decreased with time from 16.3 ºC on 12 October to 15.5 ºC on 14 October. On 15 October, the observed temperature (Figure 4.14) had a significant drop of ~5 ºC due mainly to the wind-induced coastal upwelling caused by persistent strong northeastward winds (Ekman transport). After a brief increase caused by intense net heat flux on 16 October, the observed temperature had another significant drop of ~7 ºC on 17 October due to the coastal upwelling caused by intense wind-induced offshore (seaward) currents at the sea surface near the coast (the maximum wind speed of about 18 m s^{-1} in the southeastward direction). The observed temperature maintained relatively cool and about 8 ºC for five days from 18 October to early 22 October due mainly to the occurrence of several coastal upwelling events (due to either the Ekman transports or intense wind-induced offshore currents), and then warmed up to 11.7 ºC on late 23 October (due to the coastal downwelling induced by relatively large westward and northwestward local winds of about 10 m s^{-1}). On 18 October 2018, the persistent strong southeastward winds (with the maximum wind speed of about 20 m s^{-1}) induced the nearly southward surface currents over the middle-shelf and offshore waters and the intense offshore surface currents near the coast, resulting in the coastal upwelling in Liverpool Bay on this day. From 19 to 20 October, relatively strong persistent northeastward winds (with the maximum wind speed of about 10 m s^{-1}) occurred over the L3 domain, resulting in coastal upwelling over the L3 domain during this period due to Ekman transport. From 21 to 22 October, relatively strong southeastward persistent local winds occurred over the L3 domain and induced coastal upwelling in the same way as on 18 October. The observed temperature decreased with time from 24 to 26 October (caused by

coastal upwelling due to wind-induced offshore surface currents near the coast) and then slightly warmed up from 26 to 31 October.

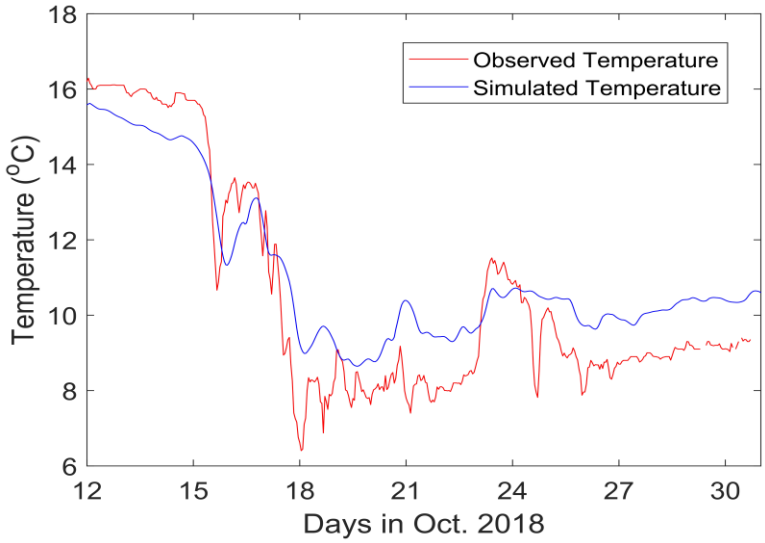

Figure 4.14. Time series of observed (red) and simulated (blue) temperature at the depth of 5 m over Liverpool Bay (Point A of Figure 3.1b) from 12 to 31 October 2018. The observed data were obtained from Prof. Jonathan Grant's research group at Dalhousie University.

A comparison between the observed (red) and simulated (blue) temperature shown in Figure 4.14 demonstrates that L3COM has certain skills to reproduce the temporal variability of temperature in Liverpool Bay. The model reproduces two significant temperature drops and large temperature fluctuations between 15 and 20 October 2018. The coupled model also has noticeable deficiencies in simulating the observed temperature at this point, with the model errors up to 1.5 °C during this period, due mainly to the relatively coarse horizontal and temporal resolutions of the atmospheric forcing.

Figure 4.15 presents the time-depth distributions of simulated temperature and DO produced by L3COM in the whole water column at Point A (shown in Figure 3.1b) from 12

to 21 October 2018. The persistent and strong winds with relatively large northeastward components generate coastal upwelling of offshore cold waters in the bottom layer and thus result in significant temperature drops at 5 m in Liverpool Bay from 15 to 20 October 2018. In addition, persistent local winds with relatively large southeastward components induce intense offshore surface currents near the coast, resulting in coastal upwelling of the subsurface inner-shelf waters with cold temperature. Figure 4.15b demonstrates that the coastal upwelling induced by local winds during this period significantly reduces the subsurface DO below 15 m in Liverpool Bay. The SST cooling caused by wind-induced coastal upwelling gradually increases the DO in the surface mixed layer (top ~15 m) in Liverpool Bay through the positive air-sea oxygen flux.

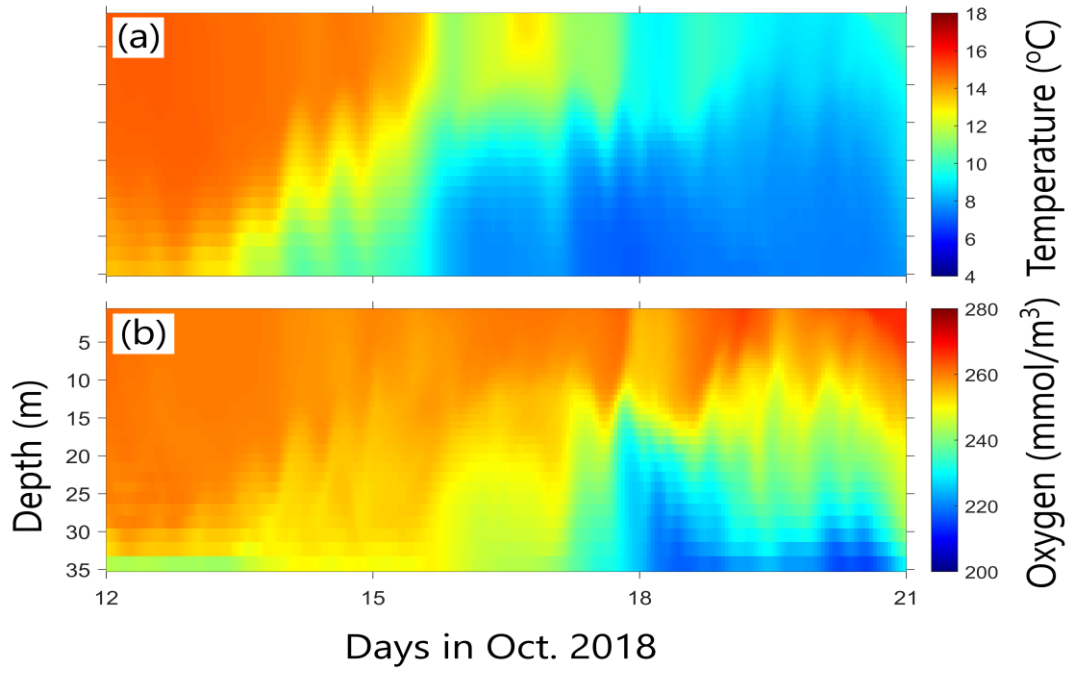

Figure 4.15. Time-depth distributions of (a) temperature and (b) DO produced by L3COM in Liverpool Bay (at Point A of Figure 3.2) from October 12 to October 21, 2018.

4.6 Summary and Conclusion

The dissolved oxygen (DO) over coastal waters of the southwestern Scotian Shelf (swScS) was investigated in this chapter using a simple oxygen model coupled to submodel L3 of NGMS-seCS. The effects of net water respiration (NWR) and sediment oxygen consumption (SOC) on the DO in summer months of 2018 over the study region were quantified by analyzing model results from three numerical experiments. These three experiments include: ControlRun (CR, realistic run by driving the model with all external forcing and parameterized NWR and SOC), NoNWR (same as CR, except for turning off NWR), and NoSOC (same as CR, except for turning off SOC). Model results indicated that the NWR had relatively large effects on DO in the subsurface (between 20 m and 40 m) and inshore waters of the southwestern ScS in the summer, due mainly to the distributions of biomass and chlorophyll. The SOC directly reduced the DO in the bottom boundary layer and indirectly reduced DO in the water columns above the bottom boundary layer through upwelling induced by winds and meso-scale eddies and vertical mixing/advection. The wind and tidal effects on DO over the L3 domain were also examined based on the model results of DO from the numerical experiments CR, NoL3Wind (same as CR, except for turning off local winds in submodel L3), and NoTide (same as CR, except for turning off tidal forcing). Local wind forcing was found to have significantly affect the upper-column DO through the air-sea oxygen flux and wind-induced vertical mixing. Wind-induced upwelling significantly reduced the low-column DO of Liverpool Bay and the coastal adjacent water. Tidal currents and tidal mixing were found to weaken the vertical stratification of dissolved oxygen over areas affected significantly by tides. In particular, tidal currents and tidal mixing reduce the vertical gradients and values of DO maxima in the vertical (occur at ~ 30 m) in summer months over these areas. Strong winds increase the SSDO through the air-sea oxygen flux.

CHAPTER 5

CONCLUSIONS

The nested-grid circulation-ice modelling system developed recently by the regional modelling group at Dalhousie University was used in my thesis research to investigate the variability of circulation and hydrography over coastal and shelf waters of the southwestern Scotian Shelf (swScS). The nested-grid circulation-ice modelling system was based on the Regional Ocean Modeling System (ROMS, www.myroms.org) and the Los Alamos Sea Ice Model (CICE, *Hunke et al*., 2017). The nested-grid modelling system for the southeastern Canadian shelf (named as NGMS-seCS) has three-level nested-grids, with nested domains of successively smaller areas and higher horizontal resolutions. The domain of submodel L1 covers the southeastern Canadian shelf (seCS) and adjacent deep ocean waters between 80 °W and 40 °W, and between 34 °N and 55 °N, with a horizontal resolution of 1/12°. The domain of submodel L2 covers the Gulf of St. Lawrence-Scotian Shelf-Gulf of Maine (GSL-ScS-GoM) and adjacent deep ocean waters between 71.5 °W and 56 °W, and between 38.5 °N and 52 °N, with a horizontal resolution of 1/36°. The domain of submodel L3 covers the coastal waters of the swScS between 66 °W and 63 °W, and between 43 °N and 44.75 °N, with a horizontal resolution of 1/108°. In collaboration with Yi Sui, a simple oxygen model was coupled to submodel L3 of the NGMS-seCS (named as L3COM) for simulating the dissolved oxygen concentration (DO) over the swScS in 2018.

Both the NGMS-seCS and L3COM were validated by comparing model results with available observations and reanalysis data. It was demonstrated that the NGMS-seCS reasonably reproduces temperature, salinity, circulation, and sea surface elevations over the

model domain. The NGMS-seCS also has certain skills in reproducing sea ice concentration in the winter months of 2018. The L3COM was found to have reasonable skills in reproducing the general vertical and horizontal distributions of DO over the swScS.

5.1 Main Results and Their Significance

A process study was made in this thesis to investigate the effects of winds (local and non-local winds) and tides on temperature, salinity, circulation, and DO over the seCS in the summer months of 2018. Four numerical experiments were conducted using the NGMS-seCS and L3COM, which include: the Control Run (CR, realistic run), NoWind (NW, wind forcing turned off in submodels L2 and L3), NoL3Wind (wind forcing turned off in submodel L3) and NoTide (NT, tidal forcing turned off).

Analysis of model results in the four experiments demonstrated that wind-induced vertical mixing significantly reduced SST and slightly increased subsurface (40 m) temperature over most areas of the L2 domain (except for local areas with very strong tidal mixing). Wind-induced vertical mixing also increased SSS over most areas of the L2 domain in the summer of 2018. Over the Georges Bank (GeB), Bay of Fundy (BoF), and coastal waters off Yarmouth, in comparison, wind forcing increased the SST mainly through the latent and sensible heat fluxes and wind-induced horizontal mixing and advection. The wind-induced horizontal mixing and advection also enhanced the spreading of fresh surface waters over coastal and estuary areas of the L2 domain and broadened the salinity fronts in the upper water column of the slope water region. Wind forcing over the L2 domain also modified the intensities and locations of warm and cold-core eddies by modulating the baroclinic instability.

Differences in model results between cases CR (include all external forcing inputs) and NoL3Wind (turn off wind forcing in submodel L3) were used to quantify the role of local

wind forcing (over the L3 domain) in hydrography and circulation over the swScS. It was found that local winds reduced SST and slightly increased SSS over the L3 domain in the summer months of 2018 through wind-induced vertical mixing. In addition, local wind forcing also induced coastal upwelling off the southwest Nova Scotia in August 2018. Local winds significantly modified the surface currents over the inner-shelf and middle-shelf waters and modulated meso-scale gyres and paths of the Nova Scotia Current in the L3 domain in August 2018. These meso-scale circulation features modified the meso-scale temperature and salinity distributions through horizontal transport and eddy-associated upwelling and downwelling. Local winds, in general, were relatively weak in summer months and thus played minor roles in the subsurface hydrodynamics below 40 m during the summer of 2018. In comparison with the effects of local winds, remote (or non-local) wind forcing played a minor role in the August-mean SST in 2018 over the swScS. The shelf waves generated by the remote winds (produced by submodel L2) propagated into the L3 domain through open boundaries, resulting in modulations of surface and subsurface circulation features, which also affected the temperature and salinity distributions through horizontal advection and eddy-associated upwelling and downwelling. The vertical profiles of temperature and salinity produced by L3COM in cases CR, NoL3Wind, and NW were analyzed to investigate the effects of local and remote winds on hydrographic stratification over the L3 domain. The vertical mixing induced by local winds significantly thickened the surface mixed layer and weakened the vertical stratification of temperature and salinity in the upper-water column of the L3 domain. The remote wind forcing played an important role in affecting the horizontal advection below 30 m over the L3 domain and thus modified the temperature and salinity distributions in the intermediate and bottom layers over coastal and shelf waters of the swScS. During the strong wind event in early July 2018, the strong northeastward winds induced the coastal upwelling and strong mixing and advection, resulting in significant SST reduction over most areas of the L3 domain.

The analysis of model results produced by submodel L2 in cases CR and NT (tidal forcing turned off) indicated the important roles of tidal forcing in temperature, salinity and ocean currents over the GSL-ScS-GoM and adjacent deep ocean waters. In the deep water off the ScS and GoM, the tidal forcing modified the Gulf Stream, eddies, and meanders. Over the BoF, northern GoM, GeB and adjacent waters, swScS, western Gulf of St. Lawrence (GSL), and Cabot Strait, tide-induced modulations in local density gradients resulted in large monthly-mean density-driven currents in August 2018. In the summer months of 2018, strong tidal mixing significantly reduced SST and increased subsurface temperature at 40 m in the BoF, coastal waters of the northern GoM, GeB and adjacent waters, and coastal waters off Yarmouth. Similarly, strong tidal mixing also significantly increased SSS over the BoF, coastal waters of the northern GoM, and swScS. The examination of the L3 model results in cases CR and NT demonstrated that the monthly-mean circulation differences between cases CR and NT were generally northeastward and offshore over Liverpool Bay and adjacent coastal waters in August 2018, indicating the important effects of tidal forcing on horizontal advection over the swScS. The tidal forcing also significantly affected the vertical distributions of temperature and salinity over Liverpool Bay and adjacent coastal waters through tide-induced vertical mixing and horizontal advection.

A sensitivity study was made using L3COM to investigate the effects of the net water respiration (NWR) and sediment oxygen consumption (SOC) on DO over coastal waters of the swScS during the summer of 2018. Three numerical experiments were conducted using L3COM, which include cases ControlRun (CR, realistic run), NoNWR (same as CR, except for turning off the parameterized net water respiration) and NoSOC (same as CR, except for turning off the parameterized sediment oxygen consumption). The parameterized NWR in L3COM was found to have relatively large and negative effects on the simulated DO in the subsurface (about 30 m) and inner shelf waters of the swScS in summer months. The SOC,

in comparison, was found to have relatively large effects on DO at the bottom layer. SOC directly reduced the DO at the bottom boundary layer and indirectly affected the DO in the other layers through vertical mixing and upwelling. The vertical distributions of August-mean DO in cases CR, NoNWR and NoSOC were highly comparable, indicating that hydrodynamics including turbulent mixing, advection, and air-sea oxygen flux played significant roles in the vertical stratification and distribution of DO over the swScS.

Model results in three additional numerical experiments using L3COM were analyzed to investigate the effects of local winds and tides on DO over the L3 domain. There three additional experiments include cases CR, NoL3Wind (wind forcing in L3COM was turned off), and NT (tidal forcing was turned off). The air-sea oxygen flux and wind-induced vertical mixing were found to have significant effects on the vertical distribution and stratification of DO over the L3 domain, particularly in the upper water column. The simulated DO in case CR showed the maximum values in the vertical at about 30 m in the summer months of 2018, due mainly to the effects of seasonal SST warming, air-sea oxygen flux, and relatively weak wind-induced vertical mixing. In comparison with model results in case CR, there was unrealistically too much dissolved oxygen trapped in the upper-water column of the L3 domain in case NoL3Wind in the summer 2018, due mainly to the absences of wind-induced vertical mixing and air-sea oxygen flux. In the summer 2018, tide-induced vertical mixing was found to reduce the maximum values of DO at the subsurface between 20 m and 40 m and weaken the vertical stratification of DO over areas affected significantly by tides.

The simulated DO in case CR during a strong wind event in early July 2018 was analyzed to assess the DO response to this event. During the strong wind event in early July, sea surface dissolved oxygen concentration (SSDO) near the coast significantly increased due partially to the relatively large and positive air-sea oxygen flux (caused by strong wind stress at the sea surface and SST cooling resulted from the wind-induced coastal upwelling),

with some contributions from wind-induced coastal upwelling of subsurface waters with relatively high DO.

In the period 15-25 October 2018, persistent local winds with relatively large northeastward and southeastward components recurrently occurred over the L3 domain and induced several coastal upwelling in Liverpool Bay and adjacent inner shelf waters. Persistent strong northeastward winds induced intense coastal upwelling through offshore Ekman transports in the surface layer. Persistent strong southeastward (roughly the offshore direction) winds induced offshore (seaward) surface currents near the coast, also resulting in coastal upwelling. During this period (15-25 October 2018), L3COM reproduced two significant temperature drops and a few relatively large temperature fluctuations at the subsurface of 5 m in Liverpool Bay, demonstrating that the model had a satisfactory skill to reproduce the temporal variability of temperature in Liverpool Bay. The wind-induced coastal upwelling during the period 15-25 October 2018 was found to reduce significantly the subsurface temperature and DO below 15 m in Liverpool Bay. In the upper-column (top ~10 m) water of Liverpool Bay, SST cooling caused by wind-induced coastal upwelling resulted in relatively large and positive air-sea oxygen flux and thus increased the upper-column DO in the top ~10 m.

5.2 Future Work

Significant progress has been made as part of my thesis work on the temporal and spatial variability of hydrodynamics and DO over coastal waters of the ScS. Many important scientific issues remain to be addressed, however, such as the nonlinear interactions between local winds and tides and the effect of climate changes on the 3D circulation over coastal waters of the seCS. The newly developed NGMS-seCS will be used to reconstruct the 3D circulation and hydrography over the GSL-ScS-GoM in the last 20 years and to examine the

retention, dispersion and hydrodynamical connectivity based on the 20-year model results to be produced by the NGMS-seCS.

Additional research is needed to improve the performance of the NGMS-seCS in simulating sea ice conditions over the seCS. As suggested by *Hasumi and Suginohara* (1995) and *Komuro and Hasumi* (2003), the formation, melting and horizontal advection of sea ice are of great importance to surface freshwater and heat fluxes, buoyancy forcing and baroclinic dynamics. Some sensitivity on sea ice conditions, including sea ice concentration, sea ice volume, and sea ice thickness will be important to understand the interaction between seawater and sea ice.

The coupled oxygen-circulation modelling system (L3COM) is a very useful tool that can be used to conduct a multi-year simulation to investigate the interannual variability of DO over the swScS. The multi-year model results to be produced by L3COM will be used to examine whether the main processes affecting DO identified in this thesis research are common during other periods. L3COM can also be applied to other coastal waters of the seCS (such as Bedford Basin and Halifax Harbour), with proper modifications on the parameterization of NWR and SOC.

In order to investigate the biological activities and variability of different dissolved gases over the seCS, a fully-coupled physical-biogeochemical modelling system is needed. The fully-coupled physical-biogeochemical modelling system currently under development will be a very important research tool for investigating the interdependencies among different biogeochemical variables and processes.

APPENDIX A

FORMULATION OF THE CIRCULATION MODEL

The Regional Ocean Modelling System (ROMS, www.myroms.org) is a general class of 3D free-surface and terrain-following numerical ocean models which solve the Reynolds-averaged Navier-Stroke equations with the hydrostatic (the vertical pressure gradient and buoyancy force balance) and Boussinesq (density variations are neglected in the horizontal momentum equations) assumptions [https://www.myroms.org/]. The basic governing equations of the ROMS in the Cartesian coordinates are

$$\frac{\partial u}{\partial t} + \boldsymbol{u} \cdot \nabla u - fv = -\frac{\partial \phi}{\partial x} - \frac{\partial}{\partial z}\left(\overline{u'w'} - \nu \frac{\partial u}{\partial z}\right) + F_u + D_u \tag{A.1}$$

$$\frac{\partial v}{\partial t} + \boldsymbol{u} \cdot \nabla v + fu = -\frac{\partial \phi}{\partial y} - \frac{\partial}{\partial z}\left(\overline{v'w'} - \nu \frac{\partial v}{\partial z}\right) + F_v + D_v \tag{A.2}$$

$$\frac{\partial \phi}{\partial z} = -\frac{\rho g}{\rho_0} \tag{A.3}$$

$$\frac{\partial C}{\partial t} + \boldsymbol{u} \cdot \nabla C = -\frac{\partial}{\partial z}\left(\overline{C'w'} - \nu_\theta \frac{\partial C}{\partial z}\right) + F_C + D_C \tag{A.4}$$

with the continuity equation

$$\frac{\partial u}{\partial x} + \frac{\partial v}{\partial y} + \frac{\partial w}{\partial z} = 0 \tag{A.5}$$

where u, v and w are the x, y, and z-components of the 3D velocity vector $\boldsymbol{u}$. $f(x, y)$ is the Coriolis parameter. ϕ is the dynamic pressure,

$$\phi(x, y, z, t) = \frac{P}{\rho_0} \tag{A.6}$$

C represents the 3D scalar fields (e.g., temperature and salinity). $\overline{u'w'}$, $\overline{v'w'}$, and $\overline{C'w'}$ are the Reynolds stresses and turbulent tracer fluxes. ν and ν_θ are the molecular viscosity and diffusivity. F_u, F_v, F_C are the terms for forcing and source/sink of the scalar field. D_u, D_v, D_C are the horizontal diffusive terms. The total in-situ density is $\rho_0 + \rho(x, y, z, t)$. More details of the formulations and parameterizations of the ROMS are available on https://www.myroms.org/.

APPENDIX B

THE SEMI-PROGNOSTIC METHOD

In the semi-prognostic method, the model hydrostatic equation

$$\frac{\partial P}{\partial z} = -g\rho_m \tag{B.1}$$

is adjusted to

$$\frac{\partial P}{\partial z} = -g[\rho_m + \beta\overline{(\rho_C - \rho_m)}] \tag{B.2}$$

where ρ_m is the prognostic density. ρ_c is the density calculated from the climatological temperature and salinity values. β is the spectral nudging coefficient. The value of β is set to 0.15 in this study. The operator $\overline{(\quad)}$ denotes the spatial average.

The semi-prognostic method introduces a correction term $-\frac{1}{\rho_0}\nabla\hat{P}$ to the horizontal momentum equations, where $\hat{P}$ satisfies

$$\frac{\partial \hat{P}}{\partial z} = -g\beta\overline{(\rho_C - \rho_m)}\ . \tag{B.3}$$

with $\hat{P} = 0$ at z = 0.

The correction term modifies the model-computed circulation and hence alters the simulated temperature and salinity. More details of the semi-prognostic method are available in *Sheng et al*. [2001] and *Greatbatch et al*. [2004].

APPENDIX C

THE SPECTRAL NUDGING METHOD

In the spectral nudging method, the model-computed temperature and salinity are nudged toward the climatological temperature and salinity values at certain frequency bands.

$$\frac{\partial T}{\partial t} + (\boldsymbol{u} \cdot \nabla)T = A \cdot \nabla^2 T + \gamma < T_c - T > \tag{C.1}$$

where the nudging term

$$< T_c - T >= \int_{-\infty}^{0} \phi(\tau)[T_c(t+\tau) - T(t+\tau)]\, d\tau. \tag{C.2}$$

is a weighted average of previous differences between the climatological and prognostic temperature and salinity. $\phi(\tau)$ is a weight function. T represents the prognostic temperature and salinity. T_c represents the climatological temperature and salinity. $\boldsymbol{u}$ represents the 3D velocity vector. More details of the spectral nudging method are available in *Thompson et al*. [2007].

The strength of the spectral nudging is controlled by the parameter γ. In this study, γ increases from 0 to 0.0011 linearly with depths from 30 to 40 m and equals to 0.0011 at depths greater than 40 m.

APPENDIX D

PARAMETERIZATION OF BOTTOM FRICTION

In this study, the logarithmic parameterization of bottom friction is applied. This parameterization assumes that flows have the classic vertical logarithmic profiles in the bottom boundary layer.

$$|u| = \frac{u_*}{\kappa} \ln\left(\frac{z}{z_0}\right) \tag{D.1}$$

where $|u| = \sqrt{u^2 + v^2}$ is the speed, $u_* = \sqrt{|\tau_{bx}| + |\tau_{by}|}$ is the friction velocity, z is the elevation above the sea bottom, κ = 0.41 is the von Karman's constant, and z_0 is the bottom roughness length in unit of meter. z_0 is set to 0.02 m in this study.

The kinematic stresses are parameterized as

$$\tau_{bx} = \frac{\kappa^2 u\sqrt{u^2+v^2}}{ln^2\left(\frac{z}{z_0}\right)} \tag{D.2}$$

$$\tau_{by} = \frac{\kappa^2 v\sqrt{u^2+v^2}}{ln^2\left(\frac{z}{z_0}\right)} \tag{D.3}$$

More discussion on the parameterization for the bottom friction can be found in *Warner et al*. [2006].

REFERENCES

Allen, J. S. (1976). Continental shelf waves and alongshore variations in bottom topography and coastline. *J. Phys. Oceanogr.*, *6*(6), 864-878.

Anderson, C., & Smith, P. C. (1989). Oceanographic observations on the Scotian Shelf during CASP. *Atmos. Ocean*, *27*(1), 130-156.

Auer, S. J. (1987). Five‐year climatological survey of the Gulf Stream system and its associated rings. *J. Geophys. Res. Oceans*, *92*(C11), 11709-11726.

Bender, M. A., Ginis, I., & Kurihara, Y. (1993). Numerical simulations of tropical cyclone-ocean interaction with a high-resolution coupled model. *J. Geophys. Res. Atmospheres*, *98*(D12), 23245-23263.

Black, P. G. (1983). Ocean temperature changes induced by tropical cyclones. (Doctoral dissertation). xxxii+278p.

Bourgault, D., & Koutitonsky, V. G. (1999). Real‐time monitoring of the freshwater discharge at the head of the St. Lawrence Estuary. *Atmos. - Ocean.*, *37*(2), 203-220.

Breitburg, D. L., Grégoire, M., Isensee, K., and Global Ocean Oxygen Network (2018). The ocean is losing its breath: Declining oxygen in the world's ocean and coastal waters. Paris: IOC-UNESCO. 39p.

Brown, O. B., Cornillon, P. C., Emmerson, S. R., & Carle, H. M. (1986). Gulf Stream warm rings: A statistical study of their behavior. *Deep-Sea Res. I: Oceanogr. Res. Pap.*, *33*(11-12), 1459-1473.

Chang, S. W. (1985). Deep ocean response to hurricanes as revealed by an ocean model with free surface. Part I: Axisymmetric case. *J. Phys. Oceanogr.*, *15*(12), 1847-1858.

Chegini, F., Lu, Y., Katavouta, A., & Ritchie, H. (2018). Coastal Upwelling Off Southwest Nova Scotia Simulated With a High-Resolution Baroclinic Ocean Model. *J. Geophys. Res. Oceans*, *123*(4), 2318-2331.

Chislock, M. F., Doster, E., Zitomer, R. A., & Wilson, A. E. (2013). Eutrophication: causes, consequences, and controls in aquatic ecosystems. *Nat. Educ. Knowl.*, *4*(4), 10.

Cutchin, D. L., & Smith, R. L. (1973). Continental shelf waves: Low-frequency variations in sea level and currents over the Oregon continental shelf. *J. Phys. Oceanogr.*, *3*(1), 73-82.

Danielson, S. L., Weingartner, T. J., Hedstrom, K. S., Aagaard, K., Woodgate, R., Curchitser, E., & Stabeno, P. J. (2014). Coupled wind-forced controls of the Bering–Chukchi shelf circulation and the Bering Strait throughflow: Ekman transport, continental shelf waves, and variations of the Pacific–Arctic sea surface height gradient. *Prog. Oceanogr.*, *125*, 40-61.

Del Giorgio, P., & Williams, P. (Eds.). (2005). *Respiration in aquatic ecosystems*. OUP Oxford. 315p.

Dever, M. (2017). *Dynamics of the Nova Scotia Current and linkages with Atlantic salmon migration patterns over the Scotian Shelf* (Doctoral dissertation). xxiv+172p.

Dever, M., Skagseth, Ø., Drinkwater, K., & Hebert, D. (2018). Frontal Dynamics of a Buoyancy‐Driven Coastal Current: Quantifying Buoyancy, Wind, and Isopycnal Tilting Influence on the Nova Scotia Current. *J. Geophys. Res. Oceans*, *123*(7), 4988-5003.

Diaz, R. J., & Rosenberg, R. (2008). Spreading dead zones and consequences for marine ecosystems. *sci.*, *321*(5891), 926-929.

Egbert, G. D., & Erofeeva, S. Y. (2002). Efficient inverse modeling of barotropic ocean tides. *J. Atmos. Oceanic Technol.*, *19*(2), 183-204.

Fennel, K., Hu, J., Laurent, A., Marta-Almeida, M., & Hetland, R. (2013). Sensitivity of hypoxia predictions for the northern Gulf of Mexico to sediment oxygen consumption and model nesting. *J. Geophys. Res. Oceans*, *118*(2), 990-1002.

Fisher, E. L. (1958). Hurricanes and the sea-surface temperature field. *J. Meteorol.*, *15*(3), 328-333.

Gangopadhyay, A., Gawarkiewicz, G., Silva, E. N. S., Monim, M., & Clark, J. (2019). An observed regime shift in the formation of warm core rings from the Gulf Stream. *Sci. Rep.*, *9*(1), 1-9.

Ganju, N. K., Brush, M. J., Rashleigh, B., Aretxabaleta, A. L., Del Barrio, P., Grear, J. S., ... & Vaudrey, J. M. (2016). Progress and challenges in coupled hydrodynamic-ecological estuarine modeling. *Estuaries Coast.*, *39*(2), 311-332.

Garrett, C. J. R., & Loucks, H. (1976). Upwelling along the Yarmouth shore of Nova Scotia. *J. Fish. Res. Board Can.*, *33*(1), 116-117.

Geshelin, Y., J. Sheng, and R. J. Greatbatch (1999), Monthly mean climatologies of temperature and salinity in the western North Atlantic, *Can. Tech. Rep. Hydrogr. Ocean Sci. 153*, 62p, Ocean Sci. Div. of Fish. and Ocean Can., Dartmouth, N. S., Canada.

Gill, A. E., Green, J. S. A., & Simmons, A. J. (1974). Energy partition in the large-scale ocean circulation and the production of mid-ocean eddies. *Deep-Sea Res*. 21, 499-528.

Gill, A. E. (1984). On the behavior of internal waves in the wakes of storms. *J. Phys. Oceanogr.*, *14*(7), 1129-1151.

Greatbatch, R. J., Sheng, J., Eden, C., Tang, L., Zhai, X., & Zhao, J. (2004). The semi-prognostic method. *Cont. Shelf Res.*, *24*(18), 2149-2165.

Greenberg, D. A., Loder, J. W., Shen, Y., Lynch, D. R., & Naimie, C. E. (1997). Spatial and temporal structure of the barotropic response of the Scotian Shelf and Gulf of Maine to surface wind stress: A model ‐ based study. *J. Geophys. Res. Oceans*, *102*(C9), 20897-20915.

Han, G., Hannah, C. G., Loder, J. W., & Smith, P. C. (1997). Seasonal variation of the three-dimensional mean circulation over the Scotian Shelf. *J. Geophys. Res. Oceans*, *102*(C1), 1011-1025.

Han, G., Paturi, S., De Young, B., Yi, Y., & Shum, C. K. (2010). A 3-D data-assimilative tidal model of the northwest Atlantic. *Atmos.-Ocean*, *48*(1), 39-57.

Hannah, C. G., Shore, J. A., Loder, J. W., & Naimie, C. E. (2001). Seasonal circulation on the western and central Scotian Shelf. *J. Phys. Oceanogr.*, *31*(2), 591-615.

Hasumi, H., & Suginohara, N. (1995). Haline circulation induced by formation and melting of sea ice. *J. Geophys. Res. Oceans*, *100*(C10), 20613-20625.

Hedström, K. S. (2009). Technical Manual for a Coupled Sea-Ice/Ocean Circulation Model (Version 3). 158p.

Hetland, R. D., & DiMarco, S. F. (2008). How does the character of oxygen demand control the structure of hypoxia on the Texas–Louisiana continental shelf?. *J. Mar. Syst.*, *70*(1-2), 49-62.

Hood R.R., E.A. Laws, R.A. Armstrong, N.R. Bates, C.W. Brown, C.A. Carlson, F. Chai, S.C. Doney, P.G. Falkowski, R.A. Feely, M.A.M. Estuaries and Coasts Friedrichs, M.R. Landry, J.K. Moore, D.M. Nelson, T.L. Richardson, B. Salihoglu, M. Schartau, D.A. Toole, and J.D. Wiggert. 2006. Pelagic functional group modeling: progress, challenges and prospects. *Deep-Sea Res. II: Top. Stud. Oceanogr., 53*(5): 459–512.

Hunke, E. C., Lipscomb, W. H., Turner, A. K., Jeffery, N., & Elliott, S. (2010). Cice: the los alamos sea ice model documentation and software user's manual version 4.1 la-cc-06-012. *T-3 Fluid Dynamics Group, Los Alamos National Laboratory*, *675*, 500. 76p.

Hunke, Elizabeth, Lipscomb, William, Jones, Philip, Turner, Adrian, Jeffery, Nicole, & Elliott, Scott. (2017, May 12). CICE, The Los Alamos Sea Ice Model (Version 00) [Computer software]. https://www.osti.gov//servlets/purl/1364126.

Katavouta, A., Thompson, K. R., Lu, Y., & Loder, J. W. (2016). Interaction between the tidal and seasonal variability of the Gulf of Maine and Scotian Shelf region. *J. Phys. Oceanogr.*, *46*(11), 3279-3298.

Komuro, Y., & Hasumi, H. (2003). Effects of surface freshwater flux induced by sea ice transport on the global thermohaline circulation. *J. Geophys. Res. Oceans*, 108(C2), 3047, doi:10.1029/2002JC001476.

Large, W. G., & Pond, S. (1981). Open ocean momentum flux measurements in moderate to strong winds. *J. Phys. Oceanogr.*, *11*(3), 324-336.

Laurent, A., Fennel, K., & Kuhn, A. (2021). An observation-based evaluation and ranking of historical Earth system model simulations in the northwest North Atlantic Ocean. *Biogeosciences*, *18*(5), 1803-1822.

Lin, S. (2021). *Study of wave-current-ice interactions over the northwest Atlantic*, Dalhousie University, xxvi+247p. (Doctoral dissertation).

Lin, S., Sheng, J., Ohashi, K., & Song, Q. (2021). Wave‐current interactions during Hurricanes Earl and Igor in the northwest Atlantic. *J. Geophys. Res. Oceans*, e2021JC017609.

Loder, J. W., Han, G., Hannah, C. G., Greenberg, D. A., & Smith, P. C. (1997). Hydrography and baroclinic circulation in the Scotian Shelf region: winter versus summer. *Can. J. Fish. Aquat. Sci.*, *54*(S1), 40-56.

Loder, J. W., Hannah, C. G., Petrie, B. D., & Gonzalez, E. A. (2003). Hydrographic and transport variability on the Halifax section. *J. Geophys. Res. Oceans*, 108(C11). 8003.

Low-Décarie, E., Chivers, C., & Granados, M. (2014). Rising complexity and falling explanatory power in ecology. *Front. Ecol. Environ.*, *12*(7), 412-418.

Marchesiello, P., McWilliams, J. C., & Shchepetkin, A. (2001). Open boundary conditions for long-term integration of regional oceanic models. *Ocean Model.*, *3*(1-2), 1-20.

Mellor, G. L., & Yamada, T. (1982). Development of a turbulence closure model for geophysical fluid problems. *Rev. Geophys.*, *20*(4), 851-875.

Meneghesso, C., Seabra, R., Broitman, B. R., Wethey, D. S., Burrows, M. T., Chan, B. K., ... & Lima, F. P. (2020). Remotely-sensed L4 SST underestimates the thermal fingerprint of coastal upwelling. *Remote Sens. Environ.*, *237*, 111588.

Mertz, G., Narayanan, S., & Helbig, J. (1993). The freshwater transport of the Labrador Current. *Atmos. - Ocean.*, *31*(2), 281-295.

Mesinger, F., DiMego, G., Kalnay, E., Mitchell, K., Shafran, P.C., Ebisuzaki, W., Jović, D., Woollen, J., Rogers, E., Berbery, E.H., & Ek, M.B., (2006). North American regional reanalysis. *Bull. Amer. Meteor. Soc.*, 87(3), 343-360.

Minnett, P. J., Alvera-Azcárate, A., Chin, T. M., Corlett, G. K., Gentemann, C. L., Karagali, I., ... & Vazquez-Cuervo, J. (2019). Half a century of satellite remote sensing of sea-surface temperature. *Remote Sens. Environ.*, 233, 111366.

Mizobata, K., Saitoh, S. I., Shiomoto, A., Miyamura, T., Shiga, N., Imai, K., ... & Sasaoka, K. (2002). Bering Sea cyclonic and anticyclonic eddies observed during summer 2000 and 2001. *Prog. Oceanogr.*, *55*(1-2), 65-75.

Naughten, K.A., Galton-Fenzi, B.K., Meissner, K.J., England, M.H., Brassington, G.B., Colberg, F., Hattermann, T., & Debernard, J.B., (2017). Spurious sea ice formation caused by oscillatory ocean tracer advection schemes, *Ocean Modell.*, 116, 108-117.

Naughten, K.A., Meissner, K.J., Galton-Fenzi, B.K., England, M.H., Timmermann, R., Hellmer, H.H., Hattermann, T., & Debernard, J.B., (2018). Intercomparison of Antarctic ice-shelf, ocean, and sea-ice interactions simulated by MetROMS-iceshelf and FESOM 1.4. *Geosci. Model Dev., 11*(4), 1257-1292.

Navas, J. M., Telfer, T. C., & Ross, L. G., (2011). Application of 3D hydrodynamic and particle tracking models for better environmental management of finfish culture. *Cont. Shelf Res.*, *31*(6), 675-684.

Ohashi, K., Sheng, J., Thompson, K. R., Hannah, C. G., & Ritchie, H. (2009a). Numerical study of three-dimensional shelf circulation on the Scotian Shelf using a shelf circulation model. *Cont. Shelf Res.*, *29*(17), 2138-2156.

Ohashi, K., Sheng, J., Thompson, K. R., Hannah, C. G., & Ritchie, H. (2009b). Effect of stratification on tidal circulation over the Scotian Shelf and Gulf of St. Lawrence: a numerical study using a three-dimensional shelf circulation model. *Ocean Dyn.*, *59*(6), 809-825.

Ohashi, K., & Sheng, J. (2013). Influence of St. Lawrence River discharge on the circulation and hydrography in Canadian Atlantic waters. *Cont. Shelf Res.*, *58*, 32-49.

Packard, T. T., & Christensen, J. P. (2004). Respiration and vertical carbon flux in the Gulf of Maine water column. *J. Mar. Res.*, *62*(1), 93-115.

Pawlowicz, R., (2020). "M_Map: A mapping package for MATLAB", version 1.4m, [Computer software], available online at www.eoas.ubc.ca/~rich/map.html.

Pawlowicz, R., Beardsley, B., & Lentz, S. (2002). Classical tidal harmonic analysis including error estimates in MATLAB using T_TIDE. *Comput and Geosci.*, *28*(8), 929-937.

Peng, G., Meier, W. N., Scott, D. J., & Savoie, M. H. (2013). A long-term and reproducible passive microwave sea ice concentration data record for climate studies and monitoring. *Earth Syst. Sci. Data*, *5*(2), 311-318.

Petrie, B., Topliss, B. J., & Wright, D. G. (1987). Coastal upwelling and eddy development off Nova Scotia. *J. Geophys. Res. Oceans*, *92*(C12), 12979-12991.

Price, J. F. (1981). Upper ocean response to a hurricane. *J. Phys. Oceanogr.*, *11*(2), 153-175.

Price, J. F. (1983). Internal wave wake of a moving storm. Part I. Scales, energy budget and observations. *J. Phys. Oceanogr.*, *13*(6), 949-965.

Reeh, N. (1985). Greenland ice-sheet mass balance and sea-level change. *Glaciers, ice sheets, and sea level: Effect of a CO2 induced climatic change. Seattle: United States Department of Energy*. 155-171

Robinson, A. R., Glenn, S. M., Spall, M. A., Walstad, L. J., Gardner, G. M., & Leslie, W. G. (1989). Forecasting Gulf Stream meanders and rings. *EOS (Transactions, American Geophysical Union)*, *70*(45), 1464-1473.

Rose K.A., J.I. Allen, Y. Artioli,M. Barange, J. Blackford, F. Carlotti, R. Cropp, U. Daewel, K. Edwards, K. Flynn, S. Hill, R. Hille Ris Lambers, G. Huse, S. Mackinson, B.A. Megrey, A. Moll, R. Rivkin, B. Salihoglu, C. Schrum, L. Shannon, Y. Shin, S.L. Smith, C. Smith, C. Solidoro, M. St John, and M. Zhou. 2010. End-to-end models for the analysis of marine ecosystems: challenges, issues, and next steps. *Mar. Coast.*, *2*(1), 115-130. 115–130.

Ross, T., Craig, S. E., Comeau, A., Davis, R., Dever, M., & Beck, M. (2017). Blooms and subsurface phytoplankton layers on the Scotian Shelf: insights from profiling gliders. *J. Mar. Syst.*, *172*, 118-127.

Schindler, D. W. (2006). Recent advances in the understanding and management of eutrophication. *Limnol. Oceanogr. Lett.*, *51*(1part2), 356-363.

Schmidtko, S., Stramma, L. & Visbeck, M. (017). Decline in global oceanic oxygen content during the past five decades. *Nature,* 542, 335-339.

Schütte, F., Brandt, P., & Karstensen, J. (2016). Occurrence and characteristics of mesoscale eddies in the tropical northeastern Atlantic Ocean. *Ocean Sci. 12*(3), 663-685.

Schwing, F. B. (1989). Subtidal response of the Scotian Shelf bottom pressure field to meteorological forcing. *Atmos. Ocean*, *27*(1), 157-180.

Schwing, F. B. (1992). Subtidal response of Scotian Shelf circulation to local and remote forcing. Part II: Barotropic model. *J. Phys. Oceanogr.*, *22*(5), 542-563.

Scrosati, R. A., & Ellrich, J. A. (2020). Latitudinal and seasonal changes in intertidal sea surface temperature along the Atlantic coast of Nova Scotia, Canada. *Front. Mar. Sci.*, *7*, 592.

Shan, S. (2010). Numerical study of three-dimensional circulation and hydrography in Halifax Harbour using a nested-grid ocean circulation model. (Master dissertation). xiii+114p.

Shan, S., & Sheng, J. (2012). Examination of circulation, flushing time and dispersion in Halifax Harbour of Nova Scotia. *Water Qual. Res. J. Canada*, *47*(3-4), 353-374.

Sheng, J., & Thompson, K. R. (1996). A robust method for diagnosing regional shelf circulation from scattered density profiles. *J. Geophys. Res. Oceans*, *101*(C11), 25647-25659.

Sheng, J., Greatbatch, R. J., & Wright, D. G. (2001). Improving the utility of ocean circulation models through adjustment of the momentum balance. *J. Geophys. Res. Oceans*, *106*(C8), 16711-16728.

Sheng, J., & Wang, L. (2004). A high-resolution coastal circulation model for Lunenburg Bay, Nova Scotia. In *Estuarine and Coastal Modeling, 2003,* 372-387.

Sheng, J., & Wang, L. (2004). Numerical study of tidal circulation and nonlinear dynamics in Lunenburg Bay, Nova Scotia. *J. Geophys. Res. Oceans*, *109*(C10).

Sheng, J., Zhai, X., & Greatbatch, R. J. (2006). Numerical study of the storm-induced circulation on the Scotian Shelf during Hurricane Juan using a nested-grid ocean model. *Prog. Oceanogr.*, *70*(2-4), 233-254.

Sheng, J., Zhao, J., & Zhai, L. (2009). Examination of circulation, dispersion, and connectivity in Lunenburg Bay of Nova Scotia using a nested-grid circulation model. *J. Mar. Syst.*, *77*(3), 350-365.

Sherwood, O. A., Lehmann, M. F., Schubert, C. J., Scott, D. B., & McCarthy, M. D. (2011). Nutrient regime shift in the western North Atlantic indicated by compound-specific δ15N of deep-sea gorgonian corals. *Proc. Nat. Acad. Sci.*, *108*(3), 1011-1015.

Smagorinsky, J., 1963. General circulation experiments with the primitive equations: I. The basic experiment. *Mon. Weather Rev.*, *91*(3), 99-164.

Smith, P. C. (1983). The mean and seasonal circulation off southwest Nova Scotia. *J. Phys. Oceanogr.*, *13*(6), 1034-1054.

Smith, P. C., Flagg, C. N., Limeburner, R., Fuentes-Yaco, C., Hannah, C., Beardsley, R. C., & Irish, J. D. (2003). Scotian Shelf crossovers during winter/spring 1999. *J. Geophys. Res. Oceans*, *108*(C11).

Smith, P. C., Petrie, B., & Mann, C. R. (1978). Circulation, variability, and dynamics of the Scotian Shelf and slope. *Can. J. Fish. Aquat. Sci., 35*(8), 1067-1083.

Smith, P. C., & Schwing, F. B. (1991). Mean circulation and variability on the eastern Canadian continental shelf. *Cont. Shelf Res.*, *11*(8-10), 977-1012.

Stammer, D., & Wunsch, C. (1999). Temporal changes in eddy energy of the oceans. *Deep-Sea Res. II: Top. Stud. Oceanogr.*, *46*(1-2), 77-108.

Steiner, Nadja & Deal, Clara & Lannuzel, Delphine & Lavoie, Diane & Massonet, Francois & Miller, Lisa & Moreau, Sebastien & Popova, Ekaterina & Stefels, Jacqueline & Tedesco, Letizia. (2016). What sea-ice biogeochemical modellers need from observersSea-ice biogeochemical modelling guide for observers. *Elem. Sci. Anth.*, *4:* 000084.

Thompson, K. R., & Sheng, J. (1997). Subtidal circulation on the Scotian Shelf: Assessing the hindcast skill of a linear, barotropic model. *J. Geophys. Res. Oceans*, *102*(C11), 24987-25003.

Thompson, K. R., Wright, D. G., Lu, Y., & Demirov, E. (2006). Erratum to “A simple method for reducing seasonal bias and drift in eddy resolving ocean models” [Ocean Modelling 13 (2006) 109–125]. *Ocean Modell.*, *14*(1-2), 122-138.

Thompson, K.R., Ohashi, K., Sheng, J., Bobanovic, J., & Ou, J., (2007). Suppressing bias and drift of coastal circulation models through the assimilation of seasonal climatologies of temperature and salinity. *Cont. Shelf Res.*, 27, 1303– 1316.

Urrego-Blanco, J., & Sheng, J. (2014). Study on subtidal circulation and variability in the Gulf of St. Lawrence, Scotian Shelf, and Gulf of Maine using a nested-grid shelf circulation model. *Ocean Dyn.*, *64*(3), 385-412.

Urrego-Blanco, J. R. (2014). Subtidal circulation, hydrography, sea ice and associated variability over the eastern Canadian shelf using a coupled ocean-ice model. (Doctoral dissertation). xviii+203p.

Wang, P., & Sheng, J. (2016). A comparative study of wave-current interactions over the eastern Canadian shelf under severe weather conditions using a coupled wave-circulation model. *J. Geophys. Res. Oceans*, *121*(7), 5252-5281.

Wang, Y., Sheng, J., & Lu, Y. (2020). Examining tidal impacts on seasonal circulation and hydrography variability over the eastern Canadian shelf using a coupled circulation-ice regional model. *Progress in Prog. Oceanogr., 189*, 102448.

Warner, J. C., Sherwood, C. R., Signell, R. P., Harris, C. K., & Arango, H. G. (2008). Development of a three-dimensional, regional, coupled wave, current, and sediment-transport model. *Comput. &Geosci.*, *34*(10), 1284-1306.

Wanninkhof, R. (1992). Relationship between wind speed and gas exchange over the ocean. *J. Geophys. Res. Oceans*, *97*(C5), 7373-7382.

Webb, P. (2019). *Introduction to Oceanography*. Roger Williams University. https://rwu.pressbooks.pub/webboceanography/. 383p.

Yang, B., & Sheng, J. (2008). Process study of coastal circulation over the inner Scotian Shelf using a nested-grid ocean circulation model, with a special emphasis on the storm-induced circulation during tropical storm Alberto in 2006. *Ocean Dyn.*, *58*(5-6), 375-396.

Yu, L., Fennel, K., & Laurent, A. (2015). A modeling study of physical controls on hypoxia generation in the northern Gulf of Mexico. *J. Geophys. Res. Oceans*, *120*(7), 5019-5039.

Zhai, L., Sheng, J., & Greatbatch, R. J. (2008). Application of a nested-grid ocean circulation model to Lunenburg Bay of Nova Scotia: Verification against observations. *J. Geophys. Res. Oceans*, *113*(C2).

Zhang, W., & McGillicuddy Jr, D. J. (2020). Warm Spiral Streamers over Gulf Stream Warm-Core Rings. *J. Phys. Oceanogr.*, *50*(11), 3331-3351.

Zhang, W. G., Wilkin, J. L., & Schofield, O. M. (2010). Simulation of water age and residence time in New York Bight. *J. Phys. Oceanogr.*, *40*(5), 965-982.